

Early Planet Formation in Embedded Disks (eDisk). XX: Constraining the Chemical Tracers of Young Protostellar Sources

Rajeeb Sharma¹ , Jes K. Jørgensen¹ , Merel L. R. van 't Hoff^{2,3} , Jeong-Eun Lee⁴ , Yuri Aikawa⁵ , Sacha Gavino^{1,6} , Yao-Lun Yang⁷ , Nagayoshi Ohashi⁸ , John J. Tobin⁹ , Patrick M. Koch⁸ , Zhi-Yun Li¹⁰ , Leslie W. Looney^{11,9} , Mayank Narang⁸ , Suchitra Narayanan¹² , and Travis J. Thieme⁸ 

¹ Niels Bohr Institute, University of Copenhagen, Jagtvej 155A, 2200 Copenhagen N., Denmark
e-mail: rajeeb.sharma@nbi.ku.dk

² Department of Astronomy, University of Michigan, 1085 S. University Ave., Ann Arbor, MI 48109-1107, USA

³ Department of Physics and Astronomy, Purdue University, 525 Northwestern Avenue, West Lafayette, IN 47907, USA

⁴ Department of Physics and Astronomy, SNU Astronomy Research Center, Seoul National University, 1 Gwanak-ro, Gwanak-gu, Seoul 08826, Korea

⁵ Department of Astronomy, Graduate School of Science, The University of Tokyo, 113-0033 Tokyo, Japan

⁶ Dipartimento di Fisica e Astronomia, Università di Bologna, Via Gobetti 93/2, 40122 Bologna, Italy

⁷ Star and Planet Formation Laboratory, RIKEN Cluster for Pioneering Research, Wako-shi, Saitama, 351-0106, Japan

⁸ Institute of Astronomy and Astrophysics, Academia Sinica. 11F of Astronomy-Mathematics Building, AS/NTU No.1, Sec. 4, Roosevelt Rd, Taipei 106216, Taiwan, R.O.C.

⁹ National Radio Astronomy Observatory, 520 Edgemont Rd., Charlottesville, VA 22903 USA

¹⁰ University of Virginia, 530 McCormick Rd., Charlottesville, Virginia 22904, USA

¹¹ Department of Astronomy, University of Illinois, 1002 West Green St, Urbana, IL 61801, USA

¹² Institute for Astronomy, University of Hawai'i at Mānoa, 2680 Woodlawn Dr., Honolulu, HI 96822, USA

September 24, 2025

ABSTRACT

Context. Recent studies indicate that the formation of planets in protoplanetary disks begins early in the embedded Class 0/I phases of protostellar evolution. The physical and chemical makeup of the embedded phase can provide valuable insights into the process of star and planet formation.

Aims. This study aims to provide a thorough overview of the various morphologies for molecular emissions observed on disk scales ($\lesssim 100$ au) toward nearby embedded sources.

Methods. We present high angular resolution ($0''.1$, ~ 15 au) molecular line emissions for ^{12}CO , ^{13}CO , C^{18}O , SO , SiO , DCN , CH_3OH , H_2CO , and $c\text{-C}_3\text{H}_2$ towards 19 nearby protostellar sources in the context of the Atacama Large Millimeter/submillimeter Array (ALMA) Large Program “Early Planet Formation in Embedded Disks (eDisk)”.

Results. Emissions in ^{12}CO are seen towards all sources and primarily trace outflowing materials. A few sources also show high-velocity jets in SiO emission and high-velocity channel maps of ^{12}CO . The ^{13}CO and C^{18}O emissions are well-known tracers of high-density regions and trace the inner envelope and disk regions with clear signs of rotation seen at continuum scales. The large-scale emissions of ^{13}CO also delineate the outflow cavity walls where the outflowing and infalling materials interact with each other, and exposure to UV radiation leads to the formation of hydrocarbons such as $c\text{-C}_3\text{H}_2$. Both DCN and CH_3OH , when detected, show compact emissions from the inner envelope and disk regions that peak at the position of the protostar. The CH_3OH emissions are contained within the region of DCN emissions, which suggests that CH_3OH traces the hot core regions. Likewise, a few sources, also display emissions in CH_3OH towards the outflow. Both SO and H_2CO show complex morphology among the sources, suggesting that they are formed through multiple processes in protostellar systems.

Key words. Stars: protostars – stars: formation – astrochemistry – protoplanetary disks

1. Introduction

The formation of low-mass stars like our Sun begins with the gravitational collapse of dense prestellar cores in cold molecular clouds. As the temperature and the pressure increase, the collapsing core eventually forms a protostar, signaling a shift from the prestellar to the protostellar phase. In the earliest phases of protostellar evolution, the Class 0 and Class I stages, the protostar is embedded in an infalling envelope that accounts for a substantial fraction of the mass of the system (Lada & Wilking 1984; André et al. 1993, 2000). This embedded nature of these young sources has long proved to be an obstacle for directly observing

protostellar disks. Consequently, most studies in the past have focused predominantly on the studies of disks in more evolved Class II sources, where most of the envelope has been accreted or dissipated (e.g. ALMA Partnership et al. 2015; Andrews et al. 2018).

Over its first decade of operations, the Atacama Large Millimeter/submillimeter Array (ALMA) has revolutionized studies of the inner regions of envelopes and structures of protoplanetary disks surrounding young stars in their earliest stages. Figure 1 presents an overview of our current understanding of the different components of an embedded protostar, such as its disk, envelope, outflow, etc. These components play an impor-

tant role during the formation of the protostar and the planets. For instance, protostellar disks regulate the mass accreted by the protostar from the envelope and provide the necessary conditions for the dust grain growth that seeds planet formation (Testi et al. 2014; Maury et al. 2019). Likewise, protostellar outflows and winds eject mass back into the molecular cloud, decreasing the protostar's efficiency of mass accretion and replenishing the turbulent motions via feedback mechanisms (Arce et al. 2007; Nakamura & Li 2014).

Understanding and characterizing the components of young protostellar systems in detail is therefore crucial in forming a comprehensive picture of star and planet formation. One way to achieve this is to study the molecular line emissions that trace the various components within a protostellar system. These molecules serve as a powerful diagnostic tool for these components and provide valuable insight into the various physical and chemical processes that occur during the formation of stars and planets.

The chemical makeup of a protostellar system is both complex and dynamic. Many molecules ranging from simple diatomic molecules to complex organic molecules (COMs, C-bearing molecules with six or more atoms) can already form during the prestellar phase (e.g., see reviews by Jørgensen et al. 2020; Ceccarelli et al. 2023). Initially, much of the chemistry of a system is at least partially inherited from the prestellar core and infalling envelope, where most molecules are primarily frozen onto the dust grains (Pontoppidan et al. 2014; Boogert et al. 2015). As the protostar evolves, the wide range of temperatures, densities, and physical processes occurring within its structures facilitate multiple new reaction pathways. Consequently, the inherited chemical composition undergoes significant changes, giving rise to a variety of new species (e.g., see reviews by Herbst & van Dishoeck 2009; Jørgensen et al. 2020; Öberg & Bergin 2021).

Astrochemical studies have long aimed to enhance our understanding of protostellar systems through molecular observations. This goal involves two primary objectives: First, to identify unique chemical tracers of specific components of protostellar systems on different spatial scales and in various evolutionary stages of young stars. Second, to thoroughly investigate the chemistry of these various components. An attempt at doing this systematically using ALMA was presented by Tychoniec et al. (2021), who examined the spectral line emissions of various molecules towards 16 Class 0/I protostars in nearby star-forming regions. By combining high-resolution spectral line data from several ALMA observations at different wavelengths (1.3 mm, 2 mm, and 3 mm observations), they analyzed emissions from several molecules and developed a comprehensive reference of molecules that traces the various morphologies in Class 0/I sources.

In this work, we present high-resolution ALMA spectral line observations of 19 nearby Class 0 and I protostars from the Early Planet Formation in Embedded Disks (eDisk) survey (Ohashi et al. 2023). This work extends on the findings from Tychoniec et al. (2021), offering two key advantages over the previous study. First, unlike the sources in Tychoniec et al. (2021), which were drawn from various studies, the eDisk program utilizes a uniform and well-characterized sample of sources, all observed in the same manner. This provides a more consistent and reliable baseline for comparison between the different sources. Second, the eDisk observations achieve higher spatial resolutions compared to those in the previous study ($\sim 0''.1$ compared to $\sim 0''.5 - 3''$). This enables us to investigate the physical and chemical processes in the innermost regions of protostellar disks.

Initial results from continuum observations and kinematic analyses of individual eDisk sources have already been presented in a series of first-look papers. These papers show that in contrast to Class II sources, where rings and gaps are ubiquitous, clear substructures are only seen in 2 out of the 19 sources, L1489IRS (Yamato et al. 2023) and OphIRS63 (Flores et al. 2023). Additionally, position velocity (PV) analysis of spectral line emissions has shown that Keplerian-rotating disks are common even in the youngest Class 0 protostars (Aso et al. 2023; van't Hoff et al. 2023; Kido et al. 2023; Sai et al. 2023; Sharma et al. 2023; Thieme et al. 2023). However, while these first-look papers have discussed cases of specific sources, a comprehensive synthesis of the data that identifies and contrasts the different chemical tracers across the entire sample is still lacking. This paper aims to address this gap by systematically analyzing the molecular tracers across all eDisk sources, providing a holistic view of the molecular tracers in early protostellar systems.

The paper is structured as follows. Sect. 2 briefly describes the observations and data reduction processes. The empirical results from the observations of the molecular line emissions are presented in Sect. 3. The implications of the results are discussed in Sect. 4 and the conclusions are presented in Sect. 5.

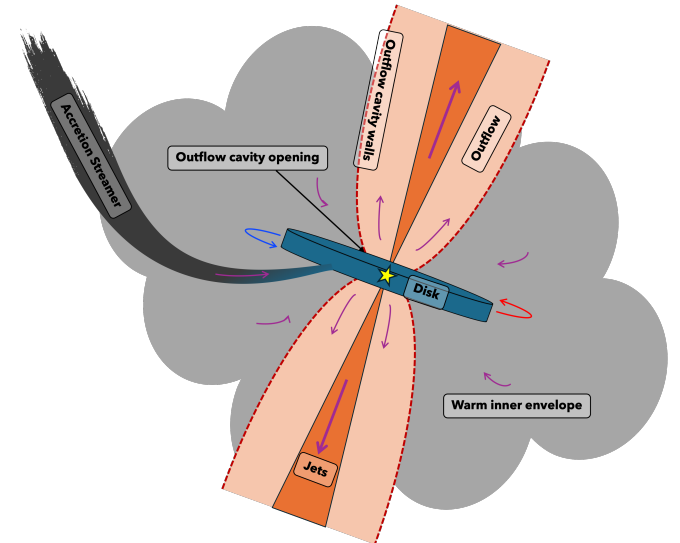


Fig. 1. Cartoon image illustrating the different components present in an embedded protostellar system.

2. Observations

Observations for the sources were conducted in multiple sessions that spanned April 2021 to July 2022 as part of the eDisk ALMA Large program (2019.1.00261.L, PI: N. Ohashi) in Band 6 at a wavelength of 1.3 mm, with supplemental data obtained from the ALMA DDT observations (2019.A.00034.S, PI: J. Tobin), also observed in Band 6 at a wavelength of 1.3 mm. The projected baselines of the observations ranged from 15 m to 12594.5 m, allowing for spatial resolutions of $\sim 0''.04$ for the continuum and $\sim 0''.1$ for the spectral lines, with slight variations among the sources due to differences in observing conditions and exact array configurations. The spectral setup was set up to probe the dust continuum and a suite of molecular species, including ^{12}CO , ^{13}CO , C^{18}O , SO , SiO , DCN , $c\text{--C}_3\text{H}_2$, H_2CO , and CH_3OH . Table 1 provides an overview of these targeted molecules, together with the velocity resolutions at which they were observed.

Both short and long baseline data were obtained for all sources in our sample, with the exception of OphIRS63, for which only short baseline data could be obtained due to scheduling constraints. The short baseline observations increase the maximum recoverable scale, (θ_{MRS}), of our observations to $\approx 3''$, allowing us to investigate the relatively extended emissions around the sources. A detailed description of the observational parameters, including the frequency ranges of the basebands, specific observation dates, number of antennas used, precipitable water vapor levels, and the complete spectral and correlator setups, can be found in Ohashi et al. (2023).

The data were initially calibrated using the standard ALMA pipeline calibrations, which involved bandpass, flux, and phase calibrations. Subsequent reduction and imaging were performed using the Common Astronomy Software Application (CASA; McMullin et al. 2007) version 6.2.1, following a script developed for the eDisk Large program¹. To enhance the data quality and signal-to-noise ratio, both phase-only and phase-and-amplitude self-calibration were applied to the continuum data. The number of self-calibrations applied varied by source. The spectral line cubes were then generated by subtracting the continuum emission from the visibility data using the CASA task *uvcontsub*. The derived solutions from the continuum self-calibrations were also applied to the line data. For each source, the final continuum images were created with a range of robust parameters from -2.0 to 2.0, and the line images were created with robust parameters of 0.5 and 2.0. We adopted the robust value of 2.0 for both the continuum contours and the spectral line images used in this work to increase the signal-to-noise ratio, particularly of the weaker spectral line emissions. For OphIRS63, which only has short baseline observations, we adopt the robust value of 0.5. This choice allowed us to keep the beam sizes of its line observations within a factor of $\lesssim 2$ -3 of the other sources, without significantly compromising the signal-to-noise ratio of the images.

In addition, comparable data for the protostars TMC1A (2015.1.01415.S; Bjerkeli et al. 2016; Harsono et al. 2018) and B335 (2013.1.00879.S, 2017.1.00288.S; Yen et al. 2015; Bjerkeli et al. 2019) were taken from the ALMA archive. Alongside the continuum emission, the archival data for TMC1A and B335 included molecular emissions from ^{12}CO , ^{13}CO , and C^{18}O . These raw datasets for these sources were reduced and imaged using the same script developed for the eDisk Large program to ensure consistency.

3. Results

Table 2 provides a summary of the continuum observations for the eDisk sample. All sources are located within 200 pc and have inclinations greater than 30 degrees, offering favorable viewing angles to study the disks. The bolometric luminosities (L_{bol}) of these sources range from $0.16 L_{\odot}$ to $10 L_{\odot}$, with a median value of $\sim 1 L_{\odot}$, reflecting a diverse set of protostellar objects. In order to characterize the different morphologies and the kinematics observed towards the eDisk sources, we create peak intensity (moment 8) and peak velocity (moment 9) maps for each of the targeted molecules. These maps are made only using pixels where emissions are detected at a level of $\geq 3\sigma$. Here, a “clear” detection in the molecular emission is defined to be a spatial structure in the moment maps that extends beyond the area of a synthesized beam. This ensures that any marginal emissions or isolated peaks that can arise from noise fluctuations and exceed the 3σ threshold are not identified as false positives. Figure 2 presents

an overview of the overall detection statistics, detailing the number of sources that display emissions for each molecule on the left and the number of molecules detected towards each source on the right. Certain molecules such as CO isotopologues, SO, and H_2CO are found throughout the sample, while molecules such as SiO, DCN, and CH_3OH are predominantly detected towards the Class 0 sources. Table 3 summarizes the molecular lines detected towards each source in this study.

In this section, we explore the origins of each of the molecules observed towards the eDisk sources. For the purpose of this study, we rely exclusively on the results seen in the moment 8 and moment 9 plots to identify and define the different components. For each of the molecular species observed, we display only a representative subset of sources that provide key insights into the emission morphology described in the main text. These representative sources are selected on the basis of the clarity and distinctiveness of the various emission morphologies observed in the moment maps. The complete maps of all sources for each molecule are shown in Appendices A and B, with references to these figures made whenever the corresponding sources are discussed throughout the sections. Furthermore, for ease of access and exploration, an interactive version of all the molecular maps for each source is available online.²

3.1. ^{12}CO

^{12}CO (2–1) emissions are detected towards all eDisk sources. Apart from IRS5N, Ced110IRS4, IRS7B, and OphIRS43, these emissions are primarily associated with molecular outflows and also delineate the walls of the outflow cavities. Figure 3 presents moment 8 maps that display the large-scale emission of ^{12}CO (2–1) towards ten eDisk sources. These maps reveal the different varieties of outflows observed in our sample. Of the 15 sources that clearly display molecular outflow in ^{12}CO , 13 exhibit wide-angle outflows that generally display curvature or have shoulder-like structures and deviate from being strictly conical or parabolic (see Figure A.1). In comparison, the outflow towards IRAS15398 is much more collimated and displays a U-shaped morphology, with the outflow cavity maintaining a relatively constant cross-sectional area. The outflow towards IRAS04302 is faint and lacks a clearly identifiable morphology (see Figure A.1). However, the extended blue-shifted emission seen towards the east shifts away from the protostar at higher velocities in the channel map (Feeney-Johansson et al. 2025; see also Lin et al. 2023).

The origin of the outflows appears to be deep within the inner disk region, very close to the corresponding positions of the protostars. The emissions are generally perpendicular to the major axis of the elongated continuum emission and typically exhibit distinct velocity gradients with red- and blue-shifted emissions tracing individual outflow lobes (see Figure A.1). The outflow originating from the main source of the close binary system IRAS32 appears to interact and blend with the material surrounding the secondary source. In addition to the outflow, the warm inner envelope and disk regions surrounding the continuum can also be traced by the ^{12}CO emission, especially in the velocity channels close to the systemic velocity (v_{sys}) of the source. These emissions likely originate from CO molecules sublimating off dust grains in the inner envelope and disk regions. This can occur due to the presence of viscous accretion heating that raises the dust temperatures above 20 K,

¹ <https://doi.org/10.5281/zenodo.7986682>

² https://group.asiaa.sinica.edu.tw/almaLP_edisk/data.php

Table 1. Summary of spectral line transitions covered

Molecule	Transition	Rest Frequency (GHz)	Velocity Resolution (km s ⁻¹)	A_{ij}^a (s ⁻¹)	E_{up}^b (K)	RMS range ^c (mJy beam ⁻¹)
¹² CO	2 – 1	230.538000	0.635	6.910×10^{-7}	16.6	0.83 – 2.14
¹³ CO	2 – 1	220.398684	0.167	5.066×10^{-7}	15.9	1.58 – 4.61
C ¹⁸ O	2 – 1	219.560354	0.167	6.011×10^{-7}	15.8	1.36 – 3.49
SiO	5 – 4	217.104980	1.340	5.196×10^{-4}	31.3	0.52 – 1.80
SO	6 ₅ – 5 ₄	219.949442	0.167	1.335×10^{-4}	35.0	1.75 – 4.33
CH ₃ OH	4 ₂ – 3 ₁ , E	218.440063	1.340	4.686×10^{-5}	45.6	0.46 – 1.24
DCN	3 – 2	217.238538	1.340	4.575×10^{-4}	20.9	0.51 – 1.68
H ₂ CO	3 _{0,3} – 2 _{0,2}	218.222192	0.167	2.818×10^{-4}	21.0	0.45 – 1.14
H ₂ CO	3 _{2,1} – 2 _{2,0}	218.760066	1.340	1.577×10^{-4}	68.1	1.30 – 3.26
H ₂ CO	3 _{2,2} – 2 _{2,1}	218.475632	1.340	1.571×10^{-4}	68.1	0.45 – 1.24
c-C ₃ H ₂ [†]	6 _{0,6} – 5 _{1,5}	217.822148	1.340	5.396×10^{-4}	38.6	0.47 – 1.36
c-C ₃ H ₂ [†]	6 _{1,6} – 5 _{0,5}	217.822148	1.340	5.396×10^{-4}	38.6	0.47 – 1.36
c-C ₃ H ₂	5 _{1,4} – 4 _{2,3}	217.940046	1.340	4.026×10^{-4}	35.4	0.53 – 1.16
c-C ₃ H ₂	5 _{2,4} – 4 _{1,3}	218.160456	1.340	4.041×10^{-4}	35.4	0.45 – 1.19

[†] These two lines are blended in eDisk observations.

^a Einstein A-coefficients.

^b Upper-state energy of the transition.

^c This range represents the range of the RMS values obtained towards different sources.

Table 2. Summary of the eDisk sources

Source Name	Hereafter	Class	Distance (pc)	T _{bol} (K)	L _{bol} (L_{\odot})	Inclination (°)	v_{sys} (km s ⁻¹)	References
BHR 71 IRS1	BHR71 IRS1	0	176	66	10	39	-4.45	(1)
BHR 71 IRS2	BHR71 IRS2	0	176	39	1.1	31	-4.45	(1)
Ced110 IRS4 [†]	Ced110IRS4	0	189	68	1.0	75	4.67	(2)
GSS30 IRS3	GSS30IRS3	0	138	50	1.7	72	2.84	(3)
IRAS 04166+2706	IRAS04166	0	156	61	0.4	47	6.80	(4)
IRAS 15398–3359	IRAS15398	0	155	50	1.4	51	5.40	(5)
IRAS 16253–2429	IRAS16253	0	139	42	0.16	68	4.00	(6)
IRAS 16544–1604	IRAS16544	0	151	50	0.89	73	4.96	(7)
L1527 IRS	L1527	0	140	41	1.3	75	5.90	(8)
R CrA IRAS 32 [†]	IRAS32	0	150	64	1.6	69	5.86	(9)
R CrA IRS5N	IRS5N	0	147	59	1.4	65	6.65	(10)
IRAS 04169+2702	IRAS04169	I	156	163	1.5	44	6.90	(11)
IRAS 04302+2247	IRAS04302	I	160	88	0.43	84	5.70	(12)
L1489 IRS	L1489	I	146	213	3.4	71	7.38	(13)
Oph IRS43 [†]	OphIRS43	I	137	193	4.1	78	3.90	(14)
Oph IRS63	OphIRS63	I	132	348	1.3	47	2.80	(15)
R CrA IRS7B [†]	IRS7B	I	152	88	5.1	68	5.90	(16, 17)
B335	B335	0	165	41	1.4	37	8.30	(9)
TMC-1A	TMC1A	I	137	183	2.3	52	6.80	(9)

[†] These sources have close binaries with projected separations of $\sim 1''.30$ (~ 250 au) for Ced110IRS4, $\sim 1''.38$ (~ 207 au) for IRAS32, $\sim 0''.55$ (~ 74 au) for OphIRS43, and $\sim 0''.70$ (~ 106 au) for IRS7B. The inclination angle for these binaries are based on their primary companion.

References. (1) Gavino et al. (2024); (2) Sai et al. (2023); (3) Santamaría-Miranda et al. (2024); (4) Phuong et al. (2025); (5) Thieme et al. (2023); (6) Aso et al. (2023); (7) Kido et al. (2023); (8) van't Hoff et al. (2023); (9) Ohashi et al. (2023); (10) Sharma et al. (2023); (11) Han et al. (2025); (12) Lin et al. (2023); (13) Yamato et al. (2023); (14) Narayanan et al. (2023); (15) Flores et al. (2023); (16) Takakuwa et al. (2024); (17) Ohashi et al. (2023).

the sublimation point of CO, even towards the midplane of the disk (Takakuwa et al. 2024).

The ¹²CO emissions towards the sources Ced110IRS4, OphIRS43, IRS7B, and IRS5N do not appear to trace any apparent outflow or jets associated with the protostar (see Figure A.1). Three of these sources are close binaries where the emissions

mainly seem to be associated with the main source. These emissions then appear to interact and blend with the material surrounding the secondary source, as with IRAS32. In Ced110IRS4 and OphIRS43, the emission appears along the direction of the major axis of the dust disks and appears to trace the rotation of the disk instead of the outflow, similar to C¹⁸O emission (see

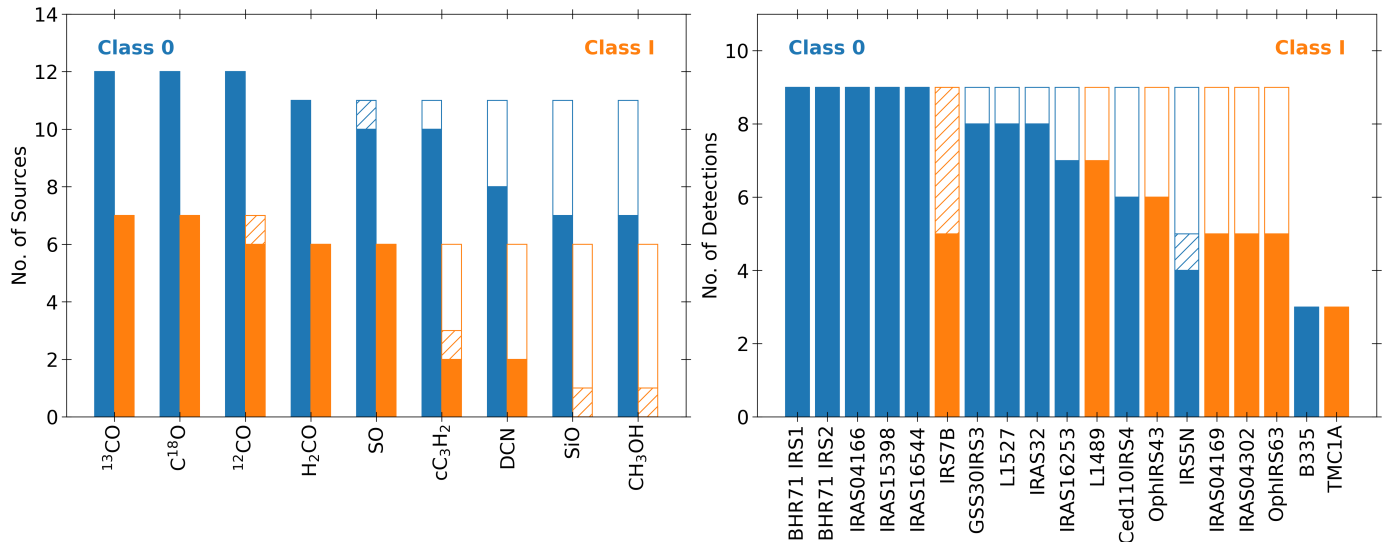


Fig. 2. Overview of the detection statistics showcasing plots illustrating the number of sources where emissions of each molecule are observed (left) and the number of molecules observed towards each source (right). The dashed regions represent cases where emissions are observed towards a source but are unlikely to be associated with that source.

Table 3. Summary of molecules observed towards eDisk sources

Source Name	^{12}CO	^{13}CO	C^{18}O	SiO	SO	DCN	CH_3OH	H_2CO	$c\text{-C}_3\text{H}_2$
BHR71 IRS1	✓	✓	✓	✓	✓	✓	✓	✓	✓
BHR71 IRS2	✓	✓	✓	✓	✓	✓	✓	✓	✓
Ced110IRS4	✓	✓	✓	✗	✓	✗	✗	✓	✓
GSS30IRS3	✓	✓	✓	✓	✓	✗	✓	✓	✓
IRAS04166	✓	✓	✓	✓	✓	✓	✓	✓	✓
IRAS15398	✓	✓	✓	✓	✓	✓	✓	✓	✓
IRAS16253	✓	✓	✓	✗	✓	✓	✗	✓	✓
IRAS16544	✓	✓	✓	✓	✓	✓	✓	✓	✓
L1527	✓	✓	✓	✓	✓	✓	✗	✓	✓
IRAS32	✓	✓	✓	✗	✗	✓	✓	✓	✓
IRS5N	✓	✓	✓	✗	✗	✗	✗	✓	✗
IRAS04169	✓	✓	✓	✗	✓	✗	✗	✓	✗
IRAS04302	✓	✓	✓	✗	✓	✗	✗	✓	✗
L1489	✓	✓	✓	✗	✓	✗	✗	✓	✓
OphIRS43	✓	✓	✓	✗	✓	✗	✗	✓	✓
OphIRS63	✓	✓	✓	✗	✓	✗	✗	✓	✗
IRS7B	✓	✓	✓	✓	✓	✓	✓	✓	✓
B335	✓	✓	✓	—	—	—	—	—	—
TMC1A	✓	✓	✓	—	—	—	—	—	—

✓ Emission is detected at $\geq 3\sigma$ level towards the source.

✗ No emission is detected at 3σ level.

✗ Emission is detected at $\geq 3\sigma$ level, but is unlikely to be directly associated with the protostellar system.

Figures A.1 and A.3 for the corresponding ^{12}CO and C^{18}O images, respectively). However, it also appears to trace the base of the outflow cavities along the minor axis of the continuum for both sources. In IRS7B, although extended emission is seen surrounding the source, it does not seem to be directly associated with the protostar. As for IRS5N, although extended emissions from the large-scale surroundings are clearly present, there are some emissions that are most likely associated with the protostar. The most notable of these is the spiral feature seen to

wards the west of the source that is likely tracing infalling material (Sharma et al. 2023). Both IRS7B and IRS5N are part of the complex Coronet region, which harbors multiple highly energetic molecular hydrogen emission-line objects (MHOs) and dozens of Herbig–Haro (HH) objects that likely interact and conceal any emission from these sources (see Wang et al. 2004, and references therein). Furthermore, any low-velocity emissions close to the v_{sys} of these sources are difficult to distinguish due to line opacity effects and spatial filtering.

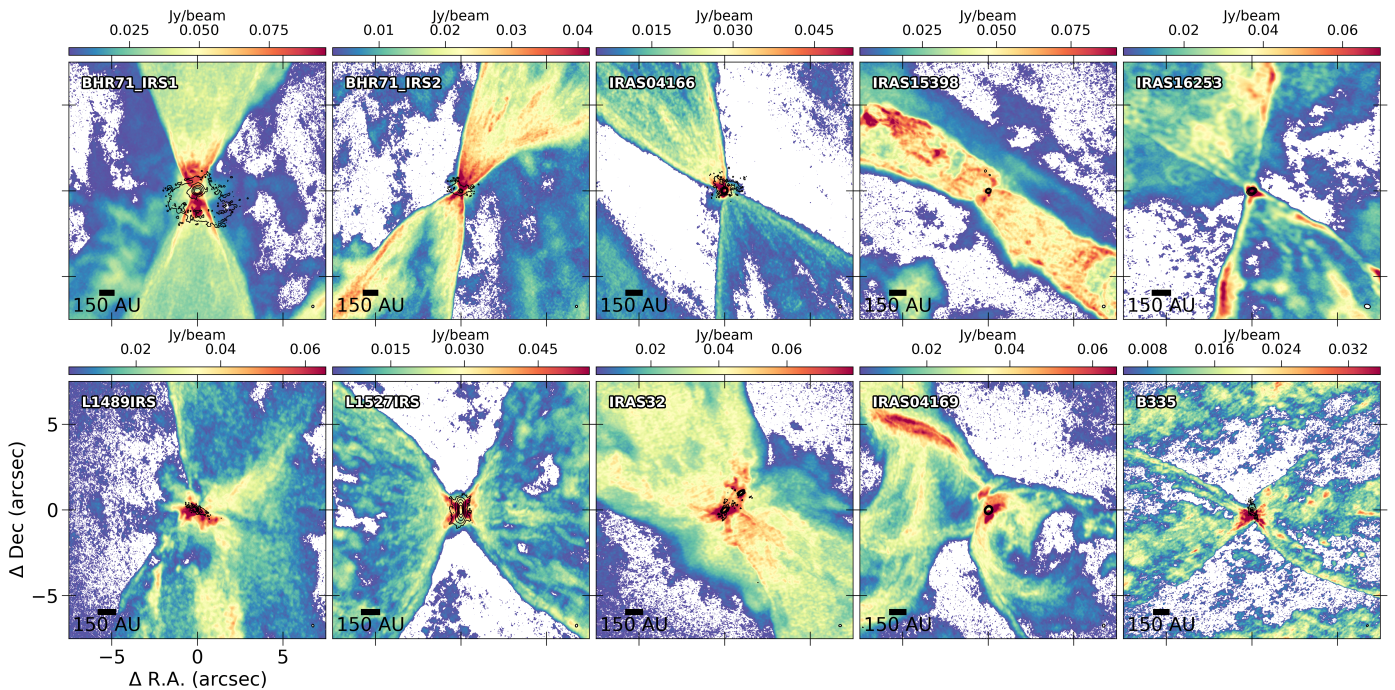


Fig. 3. Moment 8 maps of ^{12}CO ($J=2-1$) created using $\geq 3\sigma$ emissions towards 10 representative eDisk sources. The contour lines display the continuum emission at thresholds of 5σ , 15σ , 45σ , 135σ , and 320σ for each source. The scale bar is located at the bottom left, and the synthesized beam is indicated in white at the bottom right corner of each image.

3.2. ^{13}CO

Emissions in ^{13}CO (2–1) are also observed toward all eDisk sources. Figure 4 displays the ^{13}CO moment 8 maps towards five eDisk sources. The emissions primarily trace the inner $\sim 3\text{--}4''$ area and peak in the disk and the warm inner envelope region near the protostar. Moment 9 maps show clear signs of rotation with the separation of blue- and red-shifted emissions along the major axis of the continuum (see Figure B.2). The extended large-scale ^{13}CO emissions trace the outflows in a few sources (e.g., IRAS16544 and BHR71 IRS1; see Figure 4), and the sections of the outflow cavity walls in others (e.g., IRAS04166 and IRAS16253; see Figure 4). ^{13}CO is a well-known tracer of dense regions, as it is sensitive to higher column densities than ^{12}CO . The extended emissions are likely resulting from the outflows and the cavity walls. The cavity walls have higher densities than those of the surrounding envelope, and their temperatures are expected to be above 20 K, the sublimation temperature of CO (Collings et al. 2004). In addition, the materials in the cavity walls are exposed to passive heating from the UV radiation of the protostar, which can further elevate temperatures in this region, sublimating more CO from ices and facilitating the production of hydrocarbons (see Sect. 4.1.2 and also Lee et al. 2014, 2015).

The ^{13}CO emission towards IRS5N and IRS7B once again appears to be affected by the surrounding environment, although to a lesser extent compared to the ^{12}CO emission. The zoomed-in moment 9 map of IRS7B shows a distinct region coinciding with the continuum that exhibits a much different velocity profile compared to the surrounding emission (see Figure B.2). This emission likely originates from the disk and inner envelope of IRS7B. Likewise, the ^{13}CO emission observed along the north-south direction of IRS5N is closer to the systemic velocity and slightly red-shifted, which is in contrast with the predominantly blue-shifted large-scale emission surrounding the source.

3.3. C^{18}O

In line with the observations of other CO isotopologues, C^{18}O (2–1) emissions are detected in all sources within the eDisk sample. Figure 5 shows the zoomed-in moment 8 maps (top) and moment 9 maps (bottom) of the C^{18}O emissions towards five eDisk sources. The moment 8 maps show that the emissions are mostly concentrated in the inner envelope and the disk region, similar to that of the ^{13}CO emissions. For most sources, the C^{18}O emission appears to have an absorption profile at the protostar position. This feature likely results from the optically thick and cold foreground clouds absorbing the warmer continuum emissions at low velocities, causing the continuum oversubtraction. This absorption also occurs towards the emissions of ^{12}CO and ^{13}CO but due to their relatively high brightness, is less apparent and important in those molecules. Furthermore, bright and optically thick continuum emissions at small radii can block the relatively weak C^{18}O emissions, resulting in continuum oversubtraction during data reduction. A distinct separation between the blue- and the red-shifted emission can be seen in the moment 9 maps along the major axis of the continuum. PV analyses of the C^{18}O emission conducted as part of the first look results of eDisk sources have observed Keplerian disks in 14 of the 19 eDisk sources (Flores et al. 2023; van't Hoff et al. 2023; Kido et al. 2023; Lin et al. 2023; Ohashi et al. 2023; Sai et al. 2023; Sharma et al. 2023; Thieme et al. 2023; Yamato et al. 2023; Encalada et al. 2024; Santamaría-Miranda et al. 2024; Han et al. 2025; Phuong et al. 2025).

Large-scale C^{18}O emissions extending over $3\text{--}4''$ are also observed towards a couple of sources (see Figure A.3). In IRAS15398, IRAS16253, and L1527, the large-scale emission faintly traces an outline of the outflow cavity walls. In IRAS16544 and IRAS04169, the extended C^{18}O emission likely traces an accretion streamer that transports material from the outer envelope to the inner envelope and disk nonaxisymmetri-

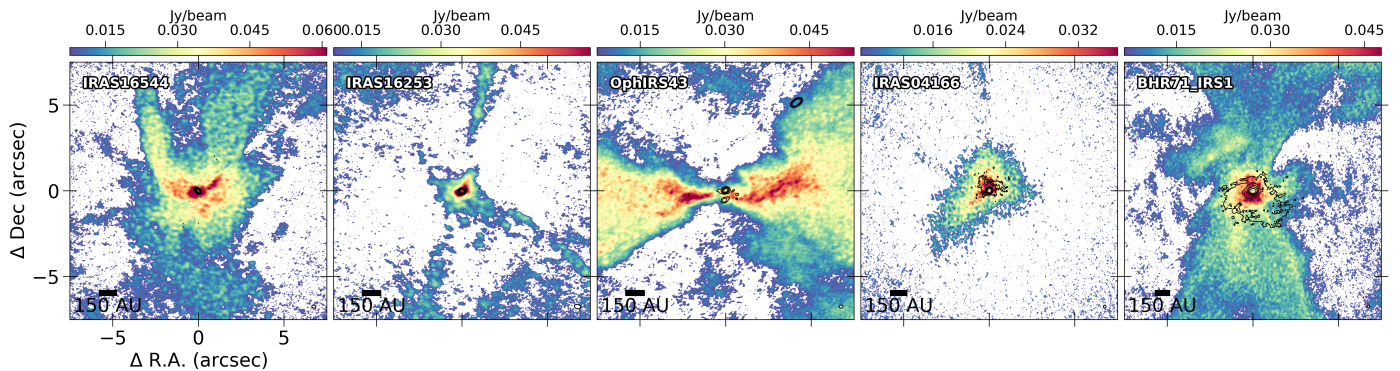


Fig. 4. Moment 8 maps of ^{13}CO ($J=2-1$) created using $\geq 3\sigma$ emissions towards 5 representative eDisk sources. The contours display the continuum emission at the same levels as Figure 3. The scale bar is located at the bottom left, and the synthesized beam is indicated in white at the bottom right corner of each image.

callly (see Section 4.1.4), whereas the arc-like structure seen towards the north of Ced110IRS4 is most likely tracing a shocked shell caused by a large-scale outflow in the past (Sai et al. 2023). As with the ^{12}CO and ^{13}CO emission maps, the large-scale C^{18}O emission seen towards IRS5N and IRS7B most likely originates from the complex environment of the Coronet region (see Figure A.3). However, they also exhibit compact emissions that overlap the continuum with a much different velocity profile than the surrounding emissions and likely trace the disk rotation, as shown in the bottom panels of Figure 5.

3.4. SiO

SiO (5–4) emission is only clearly detected towards eight eDisk sources, namely BHR71 IRS1/2, IRAS16544, IRAS15398, IRAS04166, GSS30IRS3, L1527, and IRS7B. Figure 6 shows the moment 8 maps of the SiO emission towards four systems. SiO is a well-known tracer of protostellar jets, and, unlike other molecules, the emission from SiO has generally been observed to be much more compact and collimated, containing knots and clumps (Jhan et al. 2022; Takahashi et al. 2024). The moment 8 maps for BHR71 IRS2 and IRAS 04166 show multiple knots throughout the elongated SiO emission, closely aligned with their outflows. The emissions toward BHR71 IRS1, IRAS16544, and L1527, while much less prominent and only observed near the protostar, also appear in the same direction as the outflow. Isolated clumps of SiO emission are observed $\sim 4''$ away from the protostar position towards GSS30IRS3, IRAS15398, and IRS7B in the west, southwest, and southeast, respectively (see Figure A.4). The clumps observed in GSS30IRS3 and IRS7B are observed along the direction of the major axis of the continuum, whereas the clump seen in IRAS15398 is oriented along the outflow direction. These clumps may be created by other shocks taking place in these regions. Nevertheless, it should be acknowledged that both sources are situated in complex regions, and some of the SiO emissions detected might be unrelated to the sources.

3.5. SO

Emissions from SO (6₅–5₄) are detected in all eDisk sources. However, in the case of IRS5N, all of the emission only appears towards the edges of the map and is most likely associated with the surrounding environment and not with the protostar itself. Figure 7 shows the zoomed-in moment 8 maps of SO (6₅–5₄) emission observed towards five systems. The emission typically

peaks within a few tens of au from the protostar, though the exact morphology varies among the sources. These emissions appear to trace the inner envelope and disk regions. In IRAS04169 and OphIRS63, the emissions reveal spiral structures that connect to the inner envelope and disk regions. These structures likely represent accretion streamers that funnel material nonaxisymmetrically to the inner envelope and the disk regions (Pineda et al. 2020; Flores et al. 2023; Lee et al. 2023, 2024; Phuong et al. 2025). The moment 9 maps of the SO emission towards most sources show that near the continuum, the emission shows clear signs of rotation (see Figure A.5).

Large-scale emissions are also observed in 8 of the 19 sources. These extended emissions appear to trace different components among the different sources. In BHR71 IRS2 and L1527, the extended SO emissions faintly trace a section of the outflow cavity wall, whereas in IRAS32, extended emissions are seen perpendicular to the outflow direction. A clump of blue-shifted SO emission is also seen southwest of IRAS15398 at the same location as the SiO clump. In IRAS16544 and Ced110IRS4, extended emissions seen toward the north of the protostar weakly trace the streamer and the shocked shell due to outflow, respectively, as observed in C^{18}O emission. The extended emissions observed towards GSS30IRS3 and IRS7B appear to be affected by the environment. However, for these two sources, the emissions near the protostar exhibit distinct velocity profiles in the moment 9 maps, suggesting an association with the protostar (see Figure B.5).

3.6. DCN

Emissions from DCN (3–2) are clearly detected in nine sources, and in all cases, the bulk of the emission appears to originate in the inner warm envelope and disk region of the protostar. Figure 8 shows the zoomed-in moment 8 maps of DCN emission observed towards four eDisk sources. Emissions in BHR71 IRS1/2, IRAS16544, and L1489 are concentrated towards the disk region and show signs of rotation in the moment 9 maps (see Figure B.6). Notably, the emissions in BHR71 IRS1 and L1489 show ring-shaped structures with an absorption profile in the middle, similar to the ones seen in C^{18}O . Extended emission that is clearly associated with the source is only observed towards IRAS15398, which shows an elongated structure extending from the northeast to the southwest, along the direction of the outflow, and has a similar velocity structure as shown by the ^{13}CO emission (see Figure A.6).

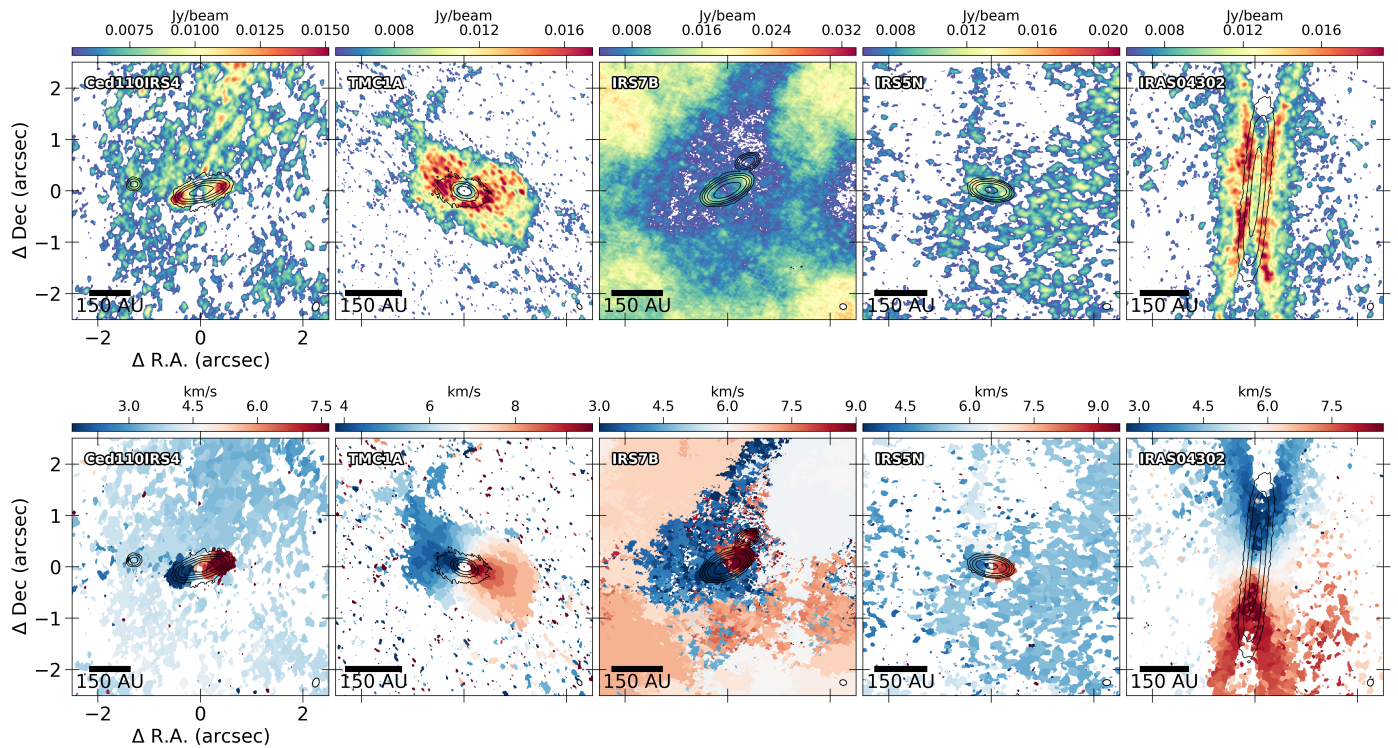


Fig. 5. Zoomed-in moment 8 maps (top) and moment 9 maps (bottom) of C^{18}O ($J=2-1$) created using $\geq 3\sigma$ emissions towards 5 representative eDisk sources. The contours display the continuum emission at the same levels as Figure 3. The scale bar is located at the bottom left, and the synthesized beam is indicated in white at the bottom right corner of each image.

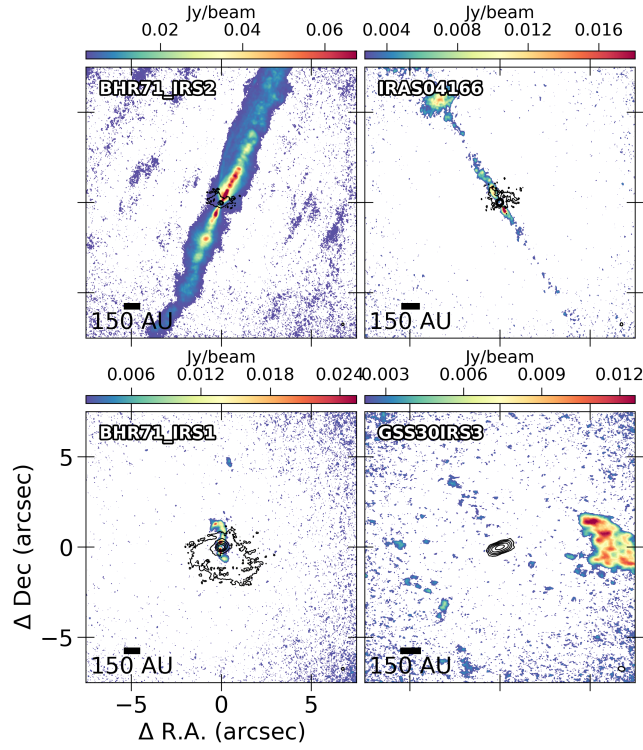


Fig. 6. Moment 8 maps of SiO ($J=5-4$) created using $\geq 3\sigma$ emissions towards 4 representative eDisk sources. The contours display the continuum emission at the same levels as Figure 3. The scale bar is located at the bottom left, and the synthesized beam is indicated in white at the bottom right corner of each image.

DCN emission is also detected towards L1527, IRAS04166, IRAS32, and IRAS16253 (see Figure A.6). However, these detections lack clear association with specific source structures. In IRAS32, knotty emission is detected between the two continuum sources of the binary, accompanied by two sets of elongated emissions. One emission is slightly blue-shifted in the north-south direction, while the other one is slightly red-shifted in the northeast-southwest direction. Patches of emission are seen towards the south and the northwest of the continuum in IRAS16253, while tentative and relatively weak emissions are also seen near the continuum positions of L1527 and IRAS04166. These sources are also affected by strong absorption at the position of their continuum. In addition to the nine sources mentioned above, DCN emission is also seen in IRS7B. Although the emissions towards IRS7B again appear to be affected by the surrounding environment, as seen in observations of other molecules, a distinct patch of highly blue-shifted emission is present towards the southeast, near the edge of the major axis of the continuum. This distinct velocity structure of this patch compared to surrounding emissions suggests a separate origin, likely associated with IRS7B itself, similar to the emissions in C^{18}O (see Figures 5, B.6).

3.7. CH_3OH

Emissions in CH_3OH (4_2-3_1) are clearly detected toward seven sources. Figure 9 shows the zoomed-in moment 8 maps illustrating CH_3OH emissions towards four eDisk sources. Towards BHR71 IRS 1/2, IRAS16544, and IRAS04166, these emissions are mostly compact and concentrated in the inner envelope and disk region, with their peaks coinciding with the positions of the corresponding protostars. In contrast, the emission towards IRAS15398 peaks near the position of the protostar, but addi-

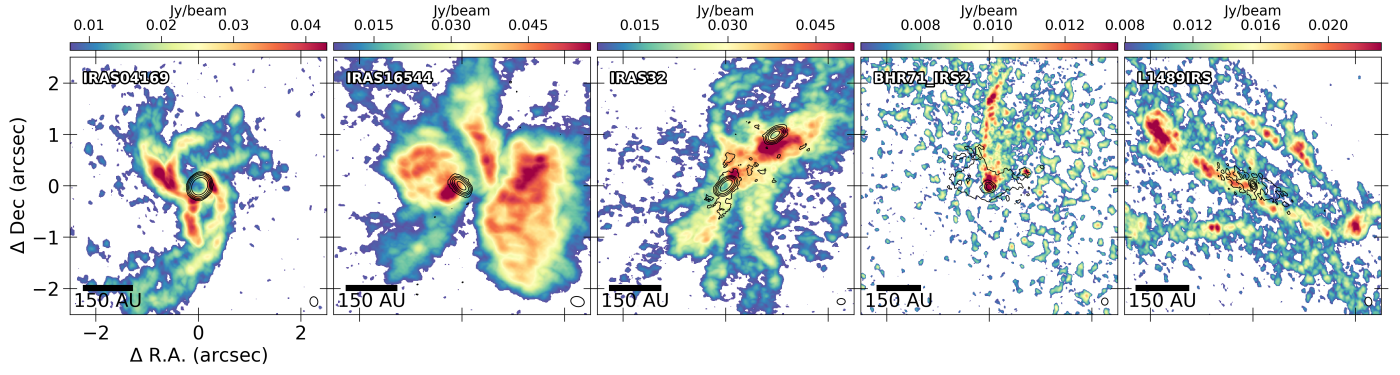


Fig. 7. Moment 8 maps of SO ($J=65-54$) created using $\geq 3\sigma$ emissions towards 5 representative eDisk sources. The contours display the continuum emission at the same levels as Figure 3. The scale bar is located at the bottom left, and the synthesized beam is indicated in white at the bottom right corner of each image.

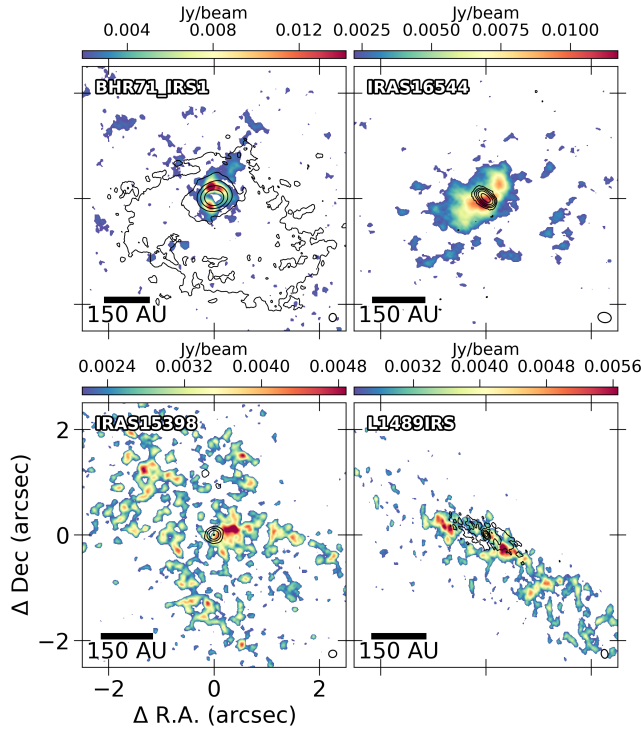


Fig. 8. Zoomed-in moment 8 maps of DCN ($J=3-2$) created using $\geq 3\sigma$ emissions towards 4 representative eDisk sources. The contours display the continuum emission at the same levels as Figure 3. The scale bar is located at the bottom left, and the synthesized beam is indicated in white at the bottom right corner of each image.

tional patchy emissions are also seen in the direction of the outflow.

In addition, patches of CH_3OH emission can be seen in the large-scale maps of three sources (see Figure A.7). Toward IRAS15398 and GSS30IRS3, a knot-like feature can be seen in the northeast direction, which aligns with the direction of their respective outflow. IRAS04166 also exhibits a similar but slightly more elongated emission in the direction of its outflow. These knots might suggest previous outbursts in these sources (Kim et al. 2024; Lee et al. 2024). A compact, likely unresolved blue-shifted patch of emission is observed near the primary source of IRAS32, potentially indicating molecular jets that have recently emerged from the source (see Figure B.7; but for a better view, consult the web application). The IRAS15398

map again reveals a clump of CH_3OH emission in the large-scale map at the same location as the SiO and SO emissions.

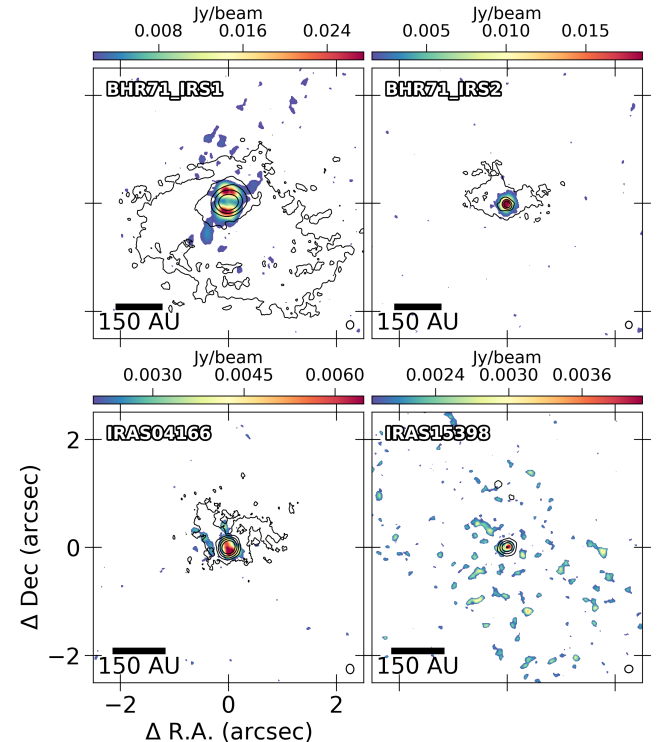


Fig. 9. Zoomed-in moment 8 maps of CH_3OH ($J=4-3$) created using $\geq 3\sigma$ emissions towards 4 representative eDisk sources. The contours display the continuum emissions at the same levels as Figure 3. The scale bar is located at the bottom left, and the synthesized beam is indicated in white at the bottom right corner of each image.

3.8. H_2CO

The spectral windows of the eDisk observations also cover three transitions of H_2CO : $3_{0,3}-2_{0,2}$, $3_{2,1}-2_{2,0}$, and $3_{2,2}-2_{2,1}$. Figure 10 displays the zoomed-in moment 8 maps of the H_2CO emissions for the $3_{0,3}-2_{0,2}$ transition with $E_{\text{up}} = 21$ K and the $3_{2,2}-2_{2,1}$ transition $E_{\text{up}} = 68$ K towards five eDisk sources. The plots show that, in most cases, the different transitions exhibit similar morphologies for a given source, with stronger and more extended emissions seen in the lower-energy transition. Emis-

sions in H_2CO are observed in all 19 eDisk sources for the lower-energy $3_{0,3}-2_{0,2}$ transition, with emissions mostly concentrating near the position of the protostar. These emissions likely trace the inner envelope and disk regions and, in some cases, also trace the base of the outflow cavity walls, forming a U-shaped morphology on either side of the minor axis of the continuum. In the large-scale map of a few sources, such as BHR71 IRS2, IRAS15398, and IRAS04166, clumpy emissions are also seen in the direction of the outflow, which is suggestive of outflow jets and can be released in shocks (Tychoniec et al. 2020).

Additionally, the moment maps of the H_2CO emission also trace the inner envelope and disks and accretion streamers towards some sources (see Figure A.8). In L1489, L1527, IRAS16253, and OphIRS43, the emission is elongated along the major axis of the continuum. In IRAS04169, the emission traces the spiral structure around the source, while in Ced110IRS4, the emission traces the extended structure seen towards the north of the source. These components have also been observed in C^{18}O and SO molecules and are likely trace accretion streamers in IRAS04169 and outflow shocked shells in Ced110IRS4. In IRAS32, the H_2CO emission is observed mostly in the mutual envelope material between the two binary sources. The emission towards OphIRS43 peaks towards the west of the source and is extended in the east-west direction. In GSS30IRS3, an elongated band of H_2CO emission in the north-south direction is seen towards the northeast of the source. IRS7B once again has two small patches of H_2CO emission with vastly different velocity structures with respect to the surrounding emission (see Figure B.8).

3.9. $c\text{-C}_3\text{H}_2$

The spectral windows of the eDisk observations also cover four transitions of $c\text{-C}_3\text{H}_2$ emissions: $6_{0,6}-5_{1,5}$, $6_{1,6}-5_{0,5}$, $5_{1,4}-4_{2,3}$, and $5_{2,4}-4_{1,3}$. Emissions in $c\text{-C}_3\text{H}_2$ are detected towards twelve eDisk sources. Figure 11 shows the moment 8 maps made with the blended $6_{0,6}-5_{1,5}$ and $6_{1,6}-5_{0,5}$ transitions towards four eDisk sources. The emissions of $c\text{-C}_3\text{H}_2$ appear to primarily trace the outflow cavity walls near the position of the protostar in many sources, such as BHR71 IRS1/2, IRAS15398, IRAS04166, IRAS16253, and IRAS16544. Emissions are also seen towards the envelope in L1527, L1489, IRAS32, IRAS16253, and IRAS16544. These emissions generally have constant velocities that are close to the systemic velocity (v_{sys}) of the source (see Figure B.11). Likewise, the emission towards Ced110IRS4 traces the outflow-shocked shell that is also seen in other molecules, and IRS7B once again shows large-scale emissions from the surroundings.

The emissions from the remaining two transitions also trace similar structures as the two blended lines towards the different sources. One notable exception to this is the source BHR71 IRS2, where each transition displays a different feature. Emissions are seen tracing the cavity walls in the blended lines, no emission is seen in the $5_{1,4}-4_{2,3}$ transition, and a patch of highly red-shifted emission is seen right at the center in the $5_{2,4}-4_{1,3}$ line (see Figures B.11, B.12, and B.13; but for a better view, consult the web application).

4. Discussion

4.1. Chemical morphology of the embedded sources

The high resolution and sensitivity of the eDisk observations provide a unique opportunity to study the spatial distribution of

the molecules in the inner envelope and disk regions of embedded sources. Table 4 summarizes the principal molecular lines detected toward the various morphological components identified in this study. In this section, we only discuss these primary molecules targeted by the spectral window of the eDisk observations. For the sources, BHR71 IRS1/2, as well as IRAS16544, line emissions of several other COMs are seen beyond the CH_3OH emissions presented in Sect. 3.7. The analysis of these more complex species observed lies beyond the scope of this paper and will be presented in a forthcoming study.

4.1.1. Outflowing material

Outflows and jets play a crucial role in transferring the excess angular momentum back to the molecular cloud and are essential feedback processes in protostellar systems (Offner & Arce 2014). Outflows generally consist of low-velocity components, with gases moving at velocities up to 20 km s^{-1} relative to the v_{sys} of the source. The threshold of 20 km s^{-1} has been selected based on the channel maps of the molecular emissions, and similar values have been adapted in previous studies (e.g. Arce et al. 2007; Frank et al. 2014). In eDisk observations, they are commonly traced by low-velocity channels of ^{12}CO and ^{13}CO emissions. All eDisk sources display a certain extent of ^{12}CO emission in the direction of the outflow (perpendicular to the major axis of the continuum). 15 of the 19 sources clearly trace large-scale bipolar outflows in ^{12}CO emission, whereas the distinction is not as clear in the remaining sources (see Figure A.1). The low-velocity ^{12}CO emission typically displays a parabolic shape with a wide-angle morphology. Our observations show that such outflows originate within the inner disk region, very close to the position of the protostar. Similar structures are also observed in the ^{13}CO emission towards some eDisk sources (see Figure A.2). The ^{13}CO emission, however, is associated with denser regions of a protostar, as it is much less abundant than ^{12}CO with the abundance ratio of $^{12}\text{CO}/^{13}\text{CO} \sim 77$ (Wilson & Rood 1994).

In contrast, protostellar jets consist of high-velocity components, with gases moving at speeds greater than 20 km s^{-1} relative to v_{sys} of the source and can reach upwards of 100 km s^{-1} (e.g., Bachiller 1996; Arce et al. 2007). These jets are often seen in high-velocity channels of ^{12}CO and SiO emissions. Figure 12 shows the moment 8 maps of high-velocity ^{12}CO emission seen towards four eDisk sources. Compared to low-velocity outflows with $|v_{\text{sys}} - v_{\text{chan}}| < 20 \text{ km s}^{-1}$, these jets are much more collimated, have narrower opening angles, and originate much closer to the protostar. Furthermore, they typically show clumpy emission towards very young protostars, which is believed to be indicative of past episodic accretion (Plunkett et al. 2015; Vorobyov et al. 2018; Sharma et al. 2020). Except in GSS30IRS3, all other sources that display high-velocity ^{12}CO emission also display corresponding jets in SiO . These SiO emissions also exhibit similar structures to their high-velocity ^{12}CO counterparts. In contrast, ^{12}CO emissions in L1527 do not show any high-velocity components, and the only indication of a jet is a patch of mostly unresolved high-velocity SiO emission close to the protostar (van't Hoff et al. 2023).

The absence of SiO emission in GSS30IRS3 as a complement to its high-velocity ^{12}CO emission could be attributed to the lack of sensitivity of the observation to detect the SiO present in the jets or to the jets themselves not being energetic enough to generate shocks to release SiO into gas, as SiO is a well-known shock tracer (Martin-Pintado et al. 1992; Bergin et al. 1998). Although SiO emissions in IRAS16544 align well with the outflow

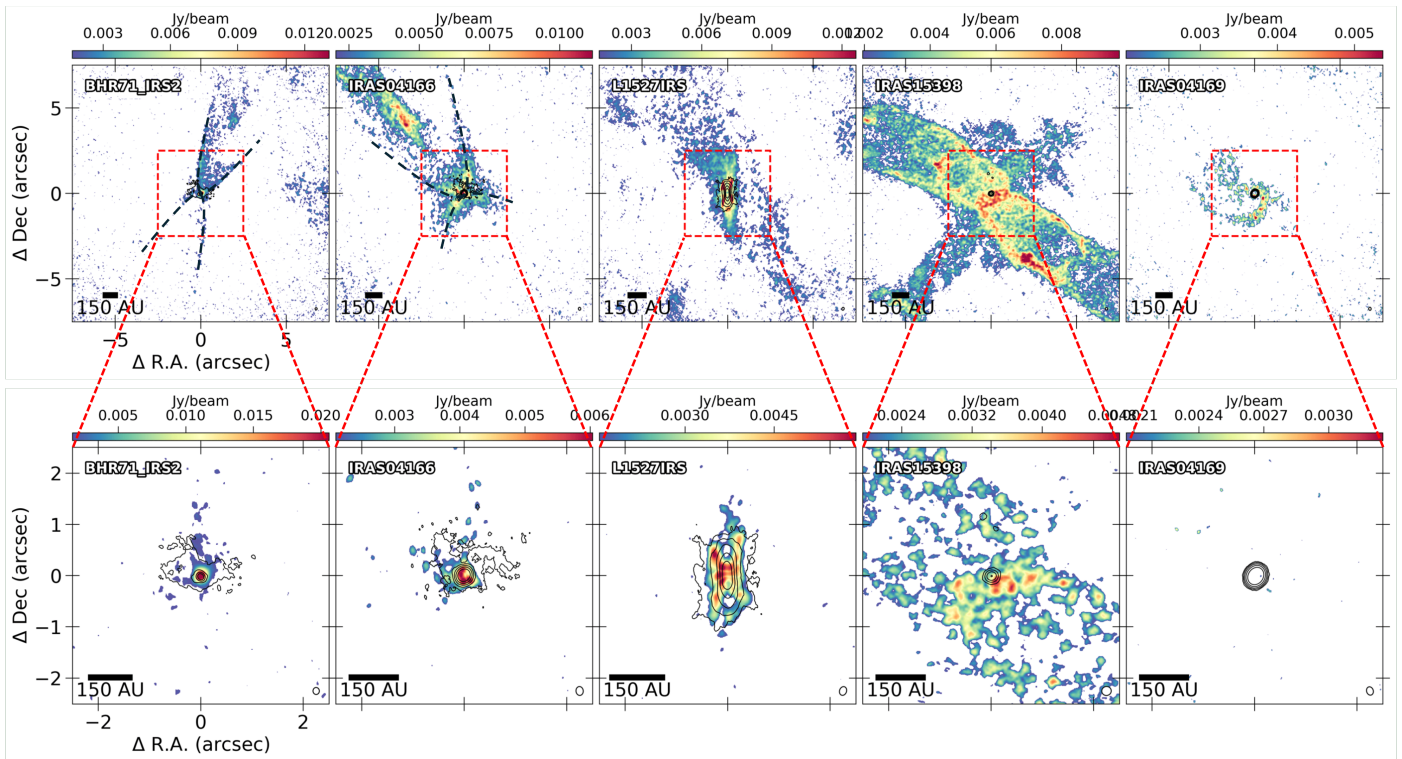


Fig. 10. Moment 8 maps of H₂CO emissions in 3_{0,3}–2_{0,2} (top) and 3_{2,2}–2_{2,1} (bottom) created using $\geq 3\sigma$ emissions towards 5 of the eDisk sources. Dashed lines show the outflow cavity walls seen towards the 3_{0,3}–2_{0,2} emissions. The contours display the continuum emission at the same levels as Figure 3. The scale bar is located at the bottom left, and the synthesized beam is indicated in white at the bottom right corner of each image.

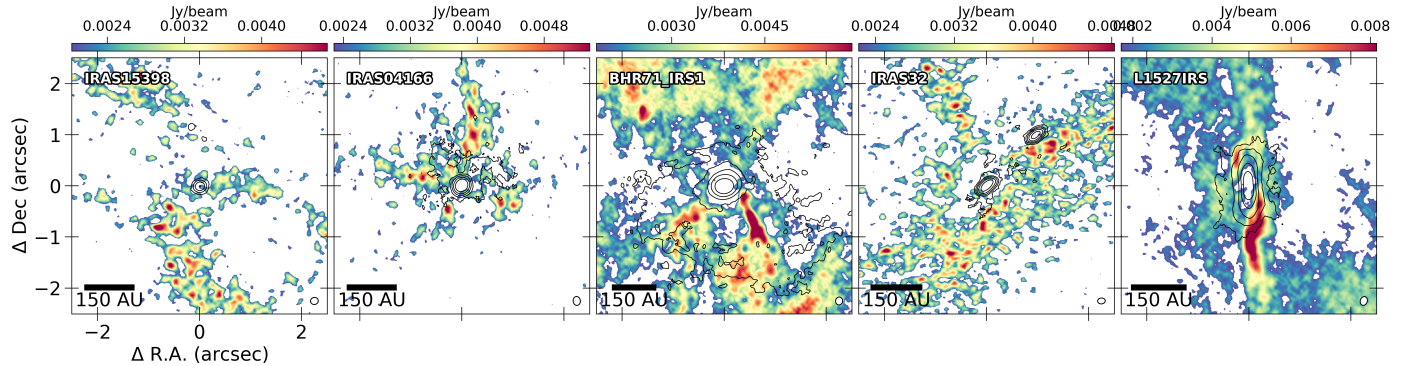


Fig. 11. Zoomed-in moment 8 maps of blended *c*-C₃H₂ $J=6_{0,6}-5_{1,5}$ and $J=6_{1,6}-5_{0,5}$ transitions created using $\geq 3\sigma$ emissions towards 5 representative eDisk sources. The contours display the continuum emissions at the same levels as Figure 3. The scale bar is located at the bottom left, and the synthesized beam is indicated in white at the bottom right corner of each image.

Table 4. Summary of molecules observed towards the various components

Components	¹² CO	¹³ CO	C ¹⁸ O	SiO	SO	DCN	CH ₃ OH	H ₂ CO	<i>c</i> -C ₃ H ₂
Outflows	✓	✓					✓	✓	
High velocity jets	✓				✓				
Outflow cavity walls	✓	✓						✓	✓
Inner envelope and disk			✓	✓	✓	✓	✓		✓
Accretion streamers			✓	✓	✓			✓	

direction, their velocities are close to v_{sys} of the source, suggesting that these emissions may result from other shock processes such as shock created by the interaction of the infalling streamer depositing material onto the disk (Garufi et al. 2022; Kido et al. 2023) rather than from shocks due to high-velocity jets. The general lack of SiO emission in the outflow towards

most eDisk sources is in contrast to the findings of Tychoniec et al. (2021) where jets in SiO were seen towards six of the seven Class 0 sources observed. The Class 0 targets of Tychoniec et al. (2021) are much more luminous, averaging $\sim 19 L_{\odot}$. This could reflect that these sources are potentially more actively accreting and driving more energetic outflows than those targeted as part

of eDisk. However, both samples are still relatively small for any more conclusive statements about this.

As mentioned in Sect.3, sporadic emissions of other molecules such as CH_3OH and H_2CO are also seen towards the outflow direction in some sources. These emissions are consistent with the release of molecules from dust grain surfaces via sputtering due to slow shocks as observed by Tychoniec et al. (2021). Such shocks can raise the temperatures in these regions to thermally desorb the frozen molecules off the dust grains. We discuss these molecules in greater detail in Sect.4.1.3 and Sect.4.2.2.

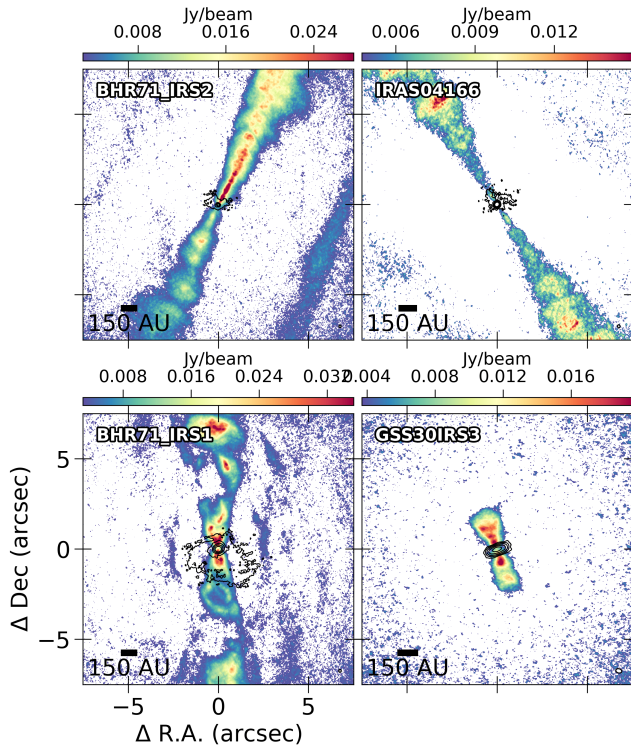


Fig. 12. Moment 8 maps of high-velocity jets seen in ^{12}CO emission towards 4 of the eDisk sources. The maps are created using the velocity channels where $|\nu_{\text{sys}} - \nu_{\text{chan}}| > 20 \text{ km s}^{-1}$. These are the same sources used for the SiO images in Figure 6, allowing for a comparison with the SiO emissions. The contours display the continuum emission at the same levels as Figure 3. The scale bar is located at the bottom left, and the synthesized beam is indicated in white at the bottom right corner of each image.

4.1.2. Outflows cavity walls

The boundary where the infalling envelope meets the cavity opened up by the outflows and jets is referred to as the outflow cavity wall. These walls typically exhibit increased chemical complexity due to the interaction between the infalling envelope and the outflows, and also due to their exposure to UV radiation from the protostar (Arce & Sargent 2006; Visser et al. 2012; Murillo et al. 2018; Tychoniec et al. 2021). Emissions of ^{12}CO , ^{13}CO , and $c\text{-C}_3\text{H}_2$ are commonly seen towards the outflow cavity walls in the eDisk sources. A few sources also show emissions in H_2CO and SO in the cavity walls. We discuss these two molecules separately in Sect. 4.2.

In addition to tracing the outflows, both ^{12}CO and ^{13}CO emissions delineate the parabolic shape of the outflow cavity walls. The emissions seen towards the cavity walls generally

have velocities close to the ν_{sys} of the source and likely originate from the sublimation of these molecules from the dust grains caused by the heating of the material by UV radiation and high-velocity jets interacting with the infalling envelope. For the protostars IRAS04166, IRAS15398, IRAS16253, and B335, most of the ^{13}CO emission in the direction of the outflow is concentrated primarily in the cavity walls. This indicates that the cavity walls are typically denser compared to both the outflow and the surrounding envelope.

Hydrocarbons such as $c\text{-C}_3\text{H}_2$ are well-known tracers of photodissociation regions (PDRs), which are dominated by UV radiation (e.g., van der Wiel et al. 2009; Guzmán et al. 2015). Exposure of the cavity walls to UV radiation from the source creates the PDR-like environment necessary for the release of atomic carbon, enabling the production of $c\text{-C}_3\text{H}_2$. The emission in $c\text{-C}_3\text{H}_2$ is concentrated in the cavity walls close to the protostar in many sources (see Figures B.11, B.12, B.13). This is anticipated, as the walls nearest to the protostar are exposed to more intense UV radiation from the protostar. Over time, this concentration of $c\text{-C}_3\text{H}_2$ in the outflow cavity shifts towards the inner envelope and disk as more of the envelope is accreted, allowing UV radiation to penetrate further (Drozdovskaya et al. 2015). This can likely explain some of the $c\text{-C}_3\text{H}_2$ emissions observed towards the envelope regions of some of the protostars.

Tychoniec et al. (2021) reported detections of $c\text{-C}_3\text{H}_2$ emissions in 4 of their 16 sources. In three of these cases, the $c\text{-C}_3\text{H}_2$ emission traces the walls of the UV-irradiated outflow cavities. For TMC1, however, the emission is observed along the extended envelope region, possibly reflecting the case where UV radiation penetrates further as the envelope dissipates (Drozdovskaya et al. 2015). Our observations of $c\text{-C}_3\text{H}_2$ emissions are consistent with these findings, further supporting that hydrocarbons such as $c\text{-C}_3\text{H}_2$ are enhanced in PDR-like regions created by UV radiation from the protostar.

4.1.3. Inner envelope and disk

The inner envelope consists of regions within several hundred au of the protostar and is characterized by higher temperatures ($T \gtrsim 30 \text{ K}$) and densities ($n \gtrsim 10^7 \text{ cm}^{-3}$) compared to the outer envelope (Jørgensen et al. 2002). This leads to a rich chemistry in this region, including the formation of COMs (see reviews by Jørgensen et al. 2020; Öberg et al. 2023). Infalling material from the inner envelope to the protostar funnels onto the circumstellar disk, which not only regulates the material accreted onto the protostar but also serves as a site for planet formation. Among the molecules targeted in the eDisk observations, emissions of ^{13}CO , C^{18}O , DCN, and CH_3OH are commonly seen towards the inner envelope and disk regions of the sources.

The CO isotopologues ^{13}CO and C^{18}O are well-known tracers of the gas distribution and kinematics in the inner envelope and disk region of protostars. This is because CO is ubiquitous in regions where temperatures rise above 20 K, and due to its low critical densities of $\sim 10^4 \text{ cm}^{-3}$, it can be readily excited even in the low-density conditions typical of outer envelope regions. As a result, CO emissions do not require active chemistry to be observed at spatial scales probed by the eDisk observations. Moment 9 maps from both these molecules at small and intermediate scales ($\lesssim 500 \text{ au}$) display a velocity gradient along the major axis of the continuum, consistent with the rotation of the disk or infalling envelope (see Figures B.2, B.3). van 't Hoff et al. (2018) found that emissions from ^{13}CO and C^{18}O in the inner envelope and disk regions of embedded sources are mostly optically thick.

This suggests that temperatures in these regions are at least high enough to cause the CO molecules to sublimate ($T \geq 20$ K).

Unlike ^{13}CO and C^{18}O , the DCN emissions observed towards the eDisk sources are much more compact and generally peak near the central protostar (see Figure B.6). DCN is produced by two main reaction pathways that are active in protostellar disks. At temperatures below 30 K, it forms via D-atom transfer with H_2D^+ , and at temperatures above 30 K, it forms through reactions with deuterated hydrocarbons such as C_2HD^+ (Millar et al. 1989; Turner 2001; Willacy 2007; Aikawa et al. 2018). The low-temperature pathway is primarily active in the outer disk midplane, just inside the CO snowline, while the warmer formation pathway is prevalent at disk surface layers where the temperatures are elevated. The observation of DCN emissions in the inner disk region, very close to the protostar towards BHR71 IRS1/2, IRAS16544, IRAS04166, and IRAS15398, suggests that the warmer temperature pathway predominantly drives DCN production in these sources. Alternatively, these emissions could also arise from DCN molecules that sublimate off dust grains in envelope regions that are close to the protostar, where temperatures are high. The sublimation temperature of DCN should be similar to that of HCN (~80 K, Bergner et al. 2022). Consequently, DCN formed in the gas phase can freeze out onto the dust grains in regions of the envelope where temperatures are lower. The extended emissions seen towards some sources likely trace the DCN produced through the lower temperature route.

An interesting result obtained in our observations is that, except for L1489 and maybe towards the disk of IRS7B, DCN emissions are observed only towards the Class 0 sources. This non-detection towards Class I sources can simply be attributed to the lack of sensitivity in our observations to the less abundant DCN emissions towards the Class I sources. This result would be a natural consequence of the alternative pathway for the DCN emission mentioned above. It is likely that DCN shares similar chemistry in the envelopes of both Class 0 and Class I sources; however, since the masses of the envelopes of the Class I sources are smaller, detecting them becomes more challenging. Alternatively, as accretion proceeds, DCN gets broken down readily by reactions with H^+ and H_3^+ (Albertsson et al. 2013), leading to a reduction in the amount of DCN detectable at the provided sensitivity. In either case, DCN might be a more reliable tracer of the earlier, younger stages of protostellar evolution.

Similar to DCN, emissions from CH_3OH are also only observed towards Class 0 sources. These emissions are also very compact and generally peak near the position of the central protostar, likely tracing the hot core region, as also inferred from the lower resolution (~100 au) data by Tychoniec et al. (2021). The emitting regions of CH_3OH are contained within the angular extent of DCN, suggesting that they trace higher temperature regions than the DCN emissions (see Figure B.7). CH_3OH primarily forms on grain surfaces through successive hydrogenation of CO-rich ices (Hiraoka et al. 1994; Watanabe & Kouchi 2002; Fuchs et al. 2009; Simons et al. 2020) or surface chain reaction in H_2O -rich ices (Bergner et al. 2017; Qasim et al. 2018) and sublimate at high temperatures (~100 K; Brown & Bolina 2007; Kristensen et al. 2010; Penteado et al. 2017). The presence of CH_3OH in the inner envelope and disk regions of BHR71 IRS1/2, IRAS16544, and likely IRAS04166 indicates that these sources are “hot corinos”, where the temperatures exceed 100 K in the innermost (≤ 100 au) dense regions around protostars (Ceccarelli 2004; Ceccarelli et al. 2007). These hot corinos are regions rich in COMs, suggesting that the production of complex molecules is well underway in the early stages of star formation.

4.1.4. Accretion streamers

The recent increase in the detection of streamers toward YSOs suggests that these structures likely play a crucial role in the star and planet formation process (see Pineda et al. 2023, for an overview). Accretion streamers channel material from the broader surrounding environment, such as filaments and fibers, directly onto the protostar’s inner disk-forming region (e.g. Pineda et al. 2020; Valdivia-Mena et al. 2024). They serve as a critical means to replenish the mass of the system, often having infall rates that exceed the accretion rates of protostars (Hsieh et al. 2019; Kido et al. 2023; Lee et al. 2023; Flores et al. 2023). This influx of material can change the temperatures and densities of the system and can also generate shocks and instabilities at regions where material is deposited (Lee et al. 2024). This can lead to the formation of dust traps, the development of substructures, the initiation of outbursts, and changes in the chemical makeup of the system (Pineda et al. 2023).

Streamers are identified toward IRAS16544, IRAS04169, IRAS16253, OphIRS63, and L1489, observed in emissions of C^{18}O , SO, and H_2CO . Figure 13 presents the moment 8 maps of C^{18}O , SO, and H_2CO $3_{0,3}-2_{0,2}$ emissions, with the streamers marked by dashed lines. For IRAS16544, IRAS04169, and L1489, all three molecules evidently trace the same streamer structures, whereas the distinction is less clear in IRAS16253 and OphIRS63. The C^{18}O emissions reveal large-scale arc-like streamers in IRAS16544 and L1489, and spiral streamers in IRAS04169. These structures might extend beyond the MRS of our observations and likely trace regions of elevated column densities where temperatures exceed 20 K, causing the CO to be released from the ice. In contrast, the SO and H_2CO emissions trace the same structures but are confined within the inner 3''–5'' region of the protostar, with enhanced emissions at the landing point of where the streamer meets the inner disk-envelope region. This enhancement is likely due to the shock resulting from the streamer interacting with the disk-envelope region. In IRAS16253, a small streamer is detected towards the east of the source in SO but appears to be obscured by emissions from the envelope in C^{18}O and H_2CO .

For OphIRS63, the C^{18}O emission shows a long arc-like streamer to the north of the protostar and a shorter spiral streamer towards the east. The SO emission does not show the extended streamer towards the north but shows three short spiral streamers arriving from the east, south, and west. The spiral arriving from the east likely traces the same streamer seen towards the east in the C^{18}O emission. The H_2CO emissions from eDisk observations do not appear to trace any of the streamers observed in C^{18}O and SO. However, a more sensitive observation conducted by the ALMA Large Program Fifty AU STudy of the chemistry in the disk/envelope system of solar-like protostars (FAUST) detected a streamer to the north of the source, likely tracing the same streamer seen towards the north in our C^{18}O emissions (Piodio et al. 2024).

The molecules C^{18}O , H_2CO , and SO observed in this work are well-known tracers of infall and shocks in protostellar systems (e.g., van Dishoeck & Blake 1998; Oya et al. 2014; Sakai et al. 2014a; Yen et al. 2017). Thus, these molecules are useful for identifying such asymmetric infalling structures and have been employed in several studies to identify accretion streamers. C^{18}O emissions commonly trace dense structures in low-temperature regions of 20–40 K due to their relatively low optical depth and were used to identify streamers in several embedded sources, including Lupus 3-MMS (Thieme et al. 2022), Perseus-50 (Valdivia-Mena et al. 2022), VLA 1623-2417W (Mer-

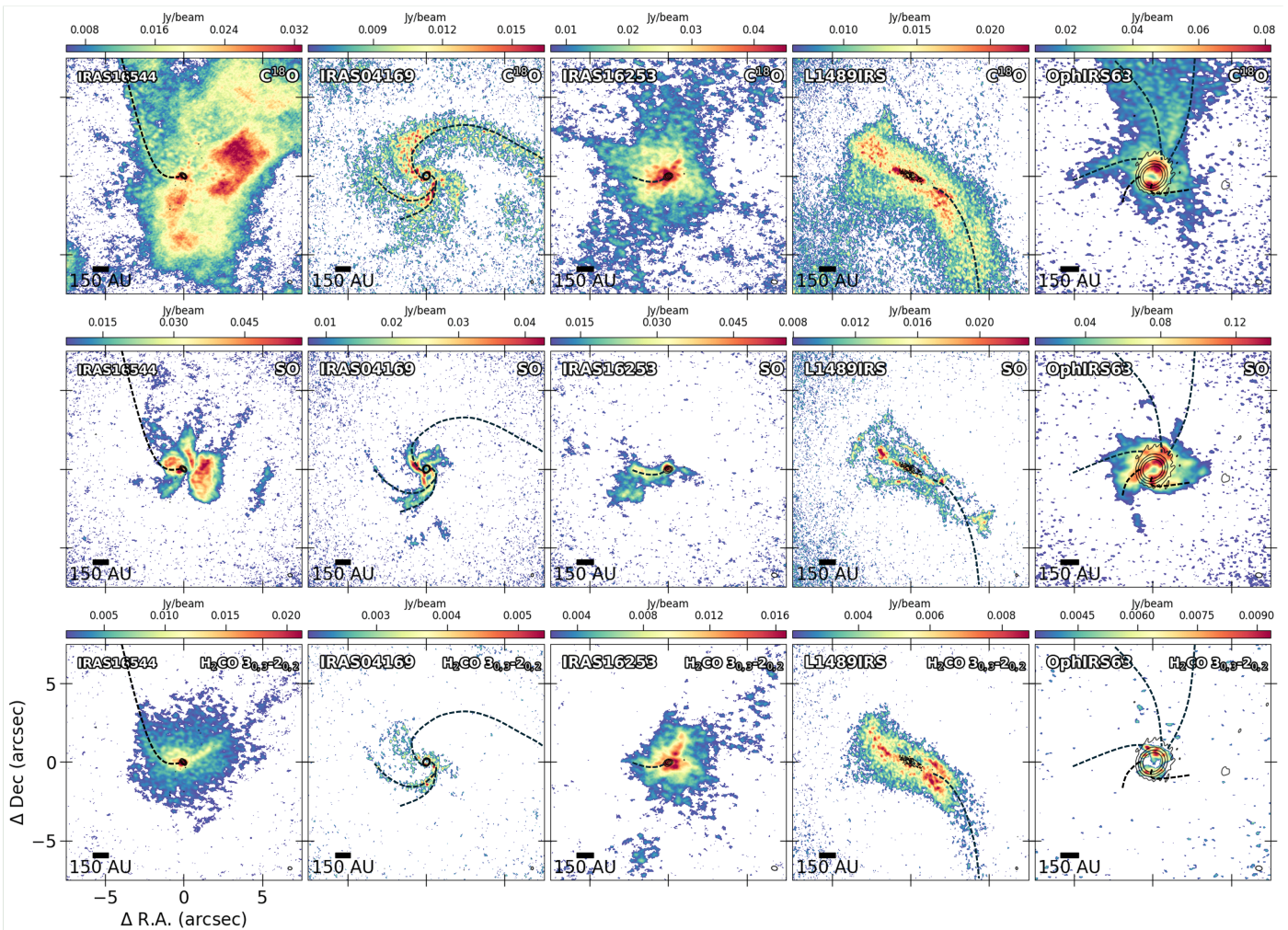


Fig. 13. Moment 8 maps depicting the streamers observed towards the eDisk sources. The streamers seen towards each source are traced by the dashed lines. The contours display the continuum emission at the same levels as Figure 3. The scale bar is located at the bottom left, and the synthesized beam is indicated in white at the bottom right corner of each image.

cimek et al. 2023), and Per-emb-8 (Lin et al. 2024). SO and H₂CO emissions, on the other hand, are often enhanced at elevated temperatures and shocked regions, making them useful tracers of impact zones where these infalling streamers deposit their material, typically in the inner envelope and disk regions of protostars (e.g., Garufi et al. 2022; Valdivia-Mena et al. 2022, 2023; Lee et al. 2023, 2024).

In addition to C¹⁸O, H₂CO, and SO, several other molecular tracers, including HC₃N, N₂H⁺, CCS, CS, HCO⁺, and SO₂, have been used to identify streamers in protostellar systems (e.g., Yen et al. 2019; Pineda et al. 2020; Garufi et al. 2022; Murillo et al. 2022). A recent systematic survey of the NGC 1333 star-forming region conducted by Valdivia-Mena et al. (2024) found evidence of streamers using emissions in HC₃N and N₂H⁺ in nearly 60% of the embedded sources. Within the eDisk survey, streamers are detected in $\sim 30\%$ of the sources (5 out of 19). However, it is important to note that the eDisk observations were not optimized for detecting large-scale streamers. The NGC1333 survey of Valdivia-Mena et al. (2024), covering an area of approximately $150'' \times 150''$ with spatial resolutions of $\sim 5''$, was specifically designed to capture large-scale accretion structures and filaments over extended envelopes. In comparison, the eDisk survey probed considerably smaller spatial scales, with spatial resolutions of $\sim 0''.1$ and maximum recoverable scales of only

$\sim 3''$. As a result, the eDisk survey is primarily sensitive to the warm, shock-influenced inner regions of streamers. Therefore, the molecular tracers used in each study are complementary and highlight the multiscale nature of accretion streamers and the importance of combining both large- and small-scale observations in order to obtain a comprehensive understanding of the accretion process in protostellar systems. Consequently, streamers may have been missed in other sources, especially if they originate from much larger scales. Notably, streamers are present in both OphIRS63 and L1489, the only two sources in our sample that also show clear signs of substructures, suggesting a possible link between the presence of streamers and the development of these substructures.

4.2. SO and H₂CO

The emissions of SO and H₂CO exhibit complex morphology and trace disparate spatial distributions within the eDisk sources. These apparent variations suggest multiple concurrent physical processes at play in protostars, the understanding of which can provide valuable insights into the star formation process.

4.2.1. Morphology of SO emission

The SO emissions exhibit peaks near the outer edge of the continuum position in several eDisk sources (see Figure B.5). SO is considered to be a reliable tracer of shocked regions in protostellar systems (e.g., Wakelam et al. 2005; Tafalla et al. 2010; Podio et al. 2015). In the cases of IRAS04169, IRAS16544, L1489, and OphIRS63, this enhancement is probably due to accretion shocks triggered by material from streamers landing onto the inner-disk envelope region (Flores et al. 2023; Kido et al. 2023; Yamato et al. 2023; Han et al. 2025). Likewise, the SO emissions show ring-like structures in L1527, OphIRS63, IRAS16253 (only visible in the robust = 0.5 image, see Aso et al. 2023), and possibly in BHR71 IRS1. The emission in L1527 was found to be likely originating from the disk surface layer and outflow cavity walls (van't Hoff et al. 2023), and this might be the case for the other sources as well. Additionally, such ring-like morphology is also believed to result from accretion shocks at the centrifugal barrier, where the infalling material from the envelope or streamers interacts with the rotating disk (Ohashi et al. 2014; Sakai et al. 2014b, 2017; Aso et al. 2023).

In the innermost regions ($\lesssim 0\farcs4$, $\lesssim 70$ au) of BHR71 IRS2, IRAS04166, IRAS15398, IRAS32, and OphIRS43, the SO emissions peak on or close to the peak of the continuum and, in most cases, are asymmetric. The emissions at these distances might be associated with the hot core region (Drozdovskaya et al. 2018), where SO can sublimate off the disk surface, as temperatures can reach higher than its sublimation temperature of ~ 50 K. Indeed, moment 9 maps show a velocity gradient along the major axis in most sources, which suggests that the emission close to the protostar likely originates from the innermost envelope and disk region. These emissions could represent the thermal sublimation of SO itself or its precursor. Similar findings have been noted in the outbursting protostar V883 Ori, where the central sublimated component of the SO emissions displays similar size and kinematic properties to those of the COMs (Lee et al. 2024). However, this scenario does not account for the asymmetry observed towards many sources. The asymmetrical peaks in these sources are oriented in the direction of the outflow, which suggests that they probably result from localized enhancement of SO caused by disk winds or bow shocks from outflows and jets (Tabone et al. 2017). This enhancement likely complements the SO emissions from the inner envelope and disk surface. Additionally, the large-scale SO emissions seen in a few sources likely also trace shocked regions caused by the outflows (see Figure A.5). A large arc-like structure is seen in the northeast of Ced110IRS4, and a small blob of emission is seen in the southwest of IRAS15398. Both structures are seen in the direction of the outflow and probably result from SO emissions from gas-phase reactions due to slow-moving outflows (~ 3 km s $^{-1}$) or sublimation of SO from ices due to fast-moving outflows ($\gtrsim 4$ km s $^{-1}$; van Gelder et al. 2021). In BHR71 IRS2 and L1527, large-scale emissions are seen toward the outflow cavities and likely also originate from the sublimation of SO from the ices due to increased temperatures in these regions.

Tychoniec et al. (2021) discovered that SO and SiO emissions exhibit similar morphologies in most sources in their study. However, we only observe the similarity between the two molecules in IRAS16544, where both molecules peak near the protostar towards the southeast, and in IRAS15398, where a clumpy emission is seen ~ 1000 au southwest in the direction of the outflow. Corresponding moment 9 maps of both molecules show that the emissions show velocity structures that are close to the v_{sys} of the corresponding source. This suggests that only

the shocks produced by the low-velocity outflows with velocities $\lesssim 20$ km s $^{-1}$ are able to induce SO emissions either chemically or due to excitation. Likewise, Tychoniec et al. (2021) observed a clear decrease in emissions in SO from Class 0 sources to Class I sources. However, we do not see a discernible difference between the sources. It is crucial to note that Tychoniec et al. (2021) detected SO emissions in only five of the sixteen sources observed, with only one being a Class I source. Because of this small sample size, caution must be exercised in generalizing this as a trend. Nevertheless, this apparent decrease likely results from the observations lacking the sensitivity needed to detect the lower column densities of the SO emissions in Class I sources due to their thinner envelopes.

4.2.2. Morphology of H₂CO emission

H₂CO was the first organic molecule identified in the ISM that includes elements other than carbon and hydrogen (Snyder et al. 1969). It has multiple reaction pathways and can form both in warm regions through gas-phase reactions (e.g., Flockenberg & Preses 2002; Atkinson et al. 2006; van der Marel et al. 2014; Loomis et al. 2015) and cold regions on grain surfaces through the hydrogenation of CO ices (e.g., Watanabe & Kouchi 2002; Cuppen et al. 2009; Fuchs et al. 2009). Its importance goes beyond being a simple organic molecule, as it is considered a key intermediate molecule in the synthesis pathways of numerous COMs and is often detected in protostellar systems (e.g., Maret et al. 2004; Jørgensen et al. 2005; Öberg et al. 2017). The multiple H₂CO transitions covered by the eDisk observations provide a valuable opportunity to probe the physical conditions of the protostellar environments where these emissions are observed.

The zoomed-in $3_{0,3}-2_{0,2}$ maps reveal that emissions in the inner envelope and disk regions are observed toward all eDisk sources (see Figure B.8). Emissions from higher energy transitions are also concentrated in these regions toward BHR71 IRS1/2, IRAS16544, IRAS04166, IRAS15398, IRAS16253, IRAS32, and L1527 (see Figures B.9, B.10). These emissions likely trace the disk surface and inner envelope regions where temperatures exceed the excitation temperatures required to populate the high-energy states. The detection of emissions in high-energy lines and the fact that CO cannot remain frozen in dust grains in these areas suggest that gas-phase reactions are dominant in these regions (Loomis et al. 2015; Öberg et al. 2017). Similarly, clusters of H₂CO emissions are detected across all transitions toward GSS30IRS3, IRAS04169, and IRAS15398 at larger distances in the outflow direction. These emissions are also probably dominated by gas-phase reactions, with shock-induced heating from outflows raising the temperatures in these regions.

Although the H₂CO emissions from both the low- and high-energy transitions trace similar morphologies in the overall moment 8 maps, some differences are observed between these transitions, especially within the individual channel maps. For instance, for the source L1527, emissions in the $3_{2,2}-2_{2,1}$ transition were found to originate mostly from the disk surface layer, while significant contributions from the envelope are seen in $3_{0,3}-2_{0,2}$ transition (see van't Hoff et al. 2023 for further details). Such discrepancies indicate that emissions from different physical layers can contribute to different transitions.

Aside from BHR71 IRS1, IRAS15398, and OphIRS43, extended H₂CO emissions are detected only in the $3_{0,3}-2_{0,2}$ transition. This absence of extended emissions in the higher energy transitions indicates that these emissions primarily trace the relatively colder, outer regions of the protostellar envelope, where

the temperatures are not quite warm enough to excite H₂CO molecules to higher energy states. Another possibility is that the quantity of molecules excited to the higher energy states in these outer regions is insufficient to produce emissions that exceed the brightness temperature thresholds sensitive to the eDisk observations. In either case, the emissions in these regions are likely dominated by the grain surface hydrogenation pathway, with H₂CO remaining frozen out until temperatures rise above the H₂CO sublimation temperatures of $\sim 40 - 70$ K (Aikawa et al. 1997; Noble et al. 2012; Fedoseev et al. 2015). A more comprehensive analysis using chemical models incorporating both formation pathways is necessary to fully untangle the chemistry of H₂CO emissions in protostellar sources.

The ratios of different K_a ladders of H₂CO transitions such as $J_{K_a K_c} = 3_{0,3}-2_{0,2}$, and $J_{K_a K_c} = 3_{2,2}-2_{2,1}$ are often considered to be good tracers of the kinetic temperatures of dense regions (e.g., Mangum & Wootten 1993; Tang et al. 2017; Artur de la Villarmois et al. 2019; van't Hoff et al. 2023). As mentioned in sections 3.8 and 4.2.2, the eDisk observations feature several sources where emissions are detected in both H₂CO ($3_{0,3}-2_{0,2}$) and ($3_{2,2}-2_{2,1}$) transitions. However, on the scales of the eDisk sources, the temperatures increase above 70 K and extinctions are $\gtrsim 100$ mag, corresponding to H₂ column densities of $\gtrsim 10^{23}$ cm⁻². A simple non-local thermal equilibrium (non-LTE) calculation using RADEX (van der Tak et al. 2007) demonstrates that the $3_{0,3}-2_{0,2}$ transition becomes optically thick under these conditions even for a conservative H₂CO abundance of 10⁻⁹, which is why this method is not applicable on these scales. Additional molecular tracers that are optically thin and sensitive to higher temperatures, such as CH₃CN or H₃CN (e.g., Bergner et al. 2018; Hsieh et al. 2023; van't Hoff et al. 2024), as well as more sophisticated radiative transfer modeling, are necessary to accurately determine the temperature structures on these scales of protostellar systems.

Emissions from H₂CO were also identified in various morphologies of a protostellar system, including envelope, disk, outflow, and jets, towards the sources studied by Tychoniec et al. (2021), consistent with the interpretation that H₂CO has a multi-component origin in the eDisk observations. However, a notable distinction between the two studies is that in our observations, we detect H₂CO emissions toward the walls of the outflow cavity in some sources, including BHR71 IRS1 and IRAS04166 (see Figure 10), which was not reported by Tychoniec et al. (2021). This discrepancy most likely arises from the difference in the spatial resolution of the two observations. The eDisk observations, with resolutions of ~ 15 au, are significantly more sensitive to emissions from small-scale structures compared to $\gtrsim 100$ au resolution in Tychoniec et al. (2021). Thus, any emissions arising from the narrow outflow cavity walls in H₂CO may have been unresolved or spatially filtered out in the previous study.

5. Conclusions

We present a comprehensive analysis of high-angular resolution ($\sim 0.1'$ or ~ 15 au) spectral line emissions detected toward 19 nearby Class 0/I protostars in an attempt to characterize the various morphologies traced by different molecules and their physical and chemical implications. Figure 14 provides a summary of our results by showing the molecules detected in each spatial region illustrated schematically in Figure 1. Our main findings are as follows:

1. Protostellar outflows are observed in 15 of the 19 sources and are primarily traced by large-scale emissions in ^{12}CO and

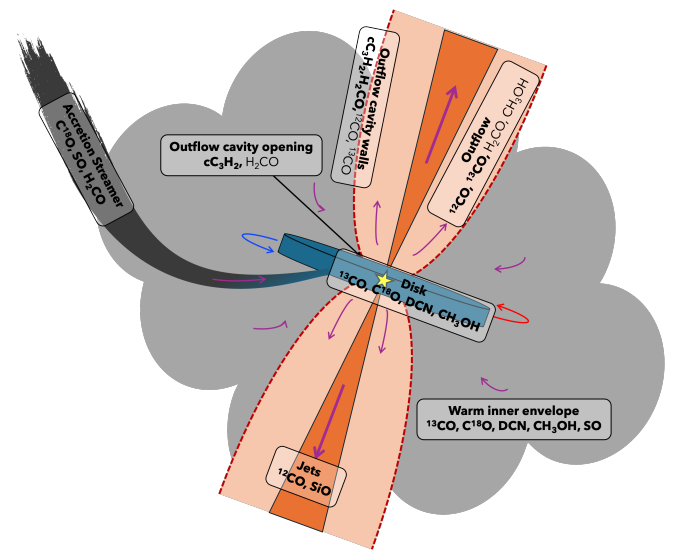


Fig. 14. Cartoon image depicting the various molecules identified in different components of this study. Molecules highlighted in bold are tracers typically found in these components, whereas those in regular font indicate tracers that are occasionally identified in some sources.

- ^{13}CO . Additionally, we also detect high-velocity molecular jets with $|\nu_{\text{sys}} - \nu_{\text{chan}}| > 20$ km s⁻¹, in emissions of ^{12}CO and SiO towards four sources.
2. The walls of the outflow cavities have high densities and are delineated by large-scale ^{13}CO emissions. Exposure to UV radiation and outflow shocks leads to increased temperatures in the cavity walls, leading to enhanced emissions from $c\text{-C}_3\text{H}_2$ and H₂CO in these regions.
 3. Rotation in the inner envelope and disk regions is traced by emissions in ^{13}CO and C¹⁸O, with Keplerian rotation identified in 14 of the 19 sources. Emissions in all nine sources where DCN is detected, and in five of the seven sources where CH₃OH is detected, are confined to the innermost regions. These molecules are most likely tracing the hot core regions of these sources.
 4. Accretion streamers are identified in five sources. These appear as spirals or elongated arc-like structures in emissions of C¹⁸O, SO, and H₂CO.
 5. Emissions in SO and H₂CO display complex morphologies and trace disparate structures across the different sources. Both molecules have multiple reaction pathways that likely contribute to the overall emissions observed towards the eDisk sources.

Acknowledgements. The authors would like to thank the anonymous referee for the helpful comments and suggestions that improved the quality of the manuscript. This paper makes use of the following ALMA data: ADS/JAO.ALMA#2019.1.00261.L, ADS/JAO.ALMA#2019.A.00034.S. ALMA is a partnership of ESO (representing its member states), NSF (USA), and NINS (Japan), together with NRC (Canada), MOST and ASIAA (Taiwan), and KASI (Republic of Korea), in cooperation with the Republic of Chile. The Joint ALMA Observatory is operated by ESO, AUI/NRAO, and NAOJ. The National Radio Astronomy Observatory is a facility of the National Science Foundation operated under cooperative agreement by Associated Universities, Inc. R.S, J.K.J, and S.G. acknowledge support from the Independent Research Fund Denmark (grant No. 0135-00123B). J.J.T. acknowledges support from NASA XRP 80NSSC22K1159. L.W.L. acknowledges support from NSF AST-2108794. Y.-L.Y. acknowledges support from Grant-in-Aid from the Ministry of Education, Culture, Sports, Science, and Technology of Japan (20H05845, 20H05844, 22K20389), and a pioneering project in RIKEN (Evolution of Matter in the Universe). Y.A. acknowledges support from Grain-in-Aid from the Ministry of Education, Culture, Sports, Science, and Technology of Japan (24K00674,

21H04495, 20H05847). J.-E.L. was supported by the National Research Foundation of Korea (NRF) grant funded by the Korea government (MSIT) (grant numbers 2021R1A2C1011718 and RS-2024-00416859). S.N. acknowledges support from NSF GRFP grant No. 2236415 and the P.E.O. Scholar Award. Z.-Y.L. is supported in part by NASA 80NSSC20K0533 and NSF AST-2307199. N.O. and M.N. acknowledge support from National Science and Technology Council (NSTC 113-2112-M-001-037) and the Academia Sinica Investigator Project Grant (AS-IV-114-M02).

References

- Aikawa, Y., Furuya, K., Hincelin, U., & Herbst, E. 2018, *ApJ*, 855, 119
- Aikawa, Y., Umebayashi, T., Nakano, T., & Miyama, S. M. 1997, *ApJ*, 486, L51
- Albertsson, T., Semenov, D. A., Vasyunin, A. I., Henning, T., & Herbst, E. 2013, *ApJS*, 207, 27
- ALMA Partnership, Brogan, C. L., Pérez, L. M., et al. 2015, *ApJ*, 808, L3
- Andrè, P., Ward-Thompson, D., & Barsony, M. 1993, *ApJ*, 406, 122
- Andrè, P., Ward-Thompson, D., & Barsony, M. 2000, in *Protostars and Planets IV*, ed. V. Mannings, A. P. Boss, & S. S. Russell, 59
- Andrews, S. M., Huang, J., Pérez, L. M., et al. 2018, *The Astrophysical Journal Letters*, 869, L41
- Arce, H. G. & Sargent, A. I. 2006, *ApJ*, 646, 1070
- Arce, H. G., Shepherd, D., Gueth, F., et al. 2007, in *Protostars and Planets V*, ed. B. Reipurth, D. Jewitt, & K. Keil, 245
- Artur de la Villarmois, E., Kristensen, L. E., & Jørgensen, J. K. 2019, *A&A*, 627, A37
- Aso, Y., Kwon, W., Ohashi, N., et al. 2023, *ApJ*, 954, 101
- Atkinson, R., Baulch, D. L., Cox, R. A., et al. 2006, *Atmospheric Chemistry & Physics*, 6, 3625
- Bachiller, R. 1996, *ARA&A*, 34, 111
- Bergin, E. A., Melnick, G. J., & Neufeld, D. A. 1998, *ApJ*, 499, 777
- Bergner, J. B., Guzmán, V. G., Öberg, K. I., Loomis, R. A., & Pegues, J. 2018, *ApJ*, 857, 69
- Bergner, J. B., Öberg, K. I., & Rajappan, M. 2017, *ApJ*, 845, 29
- Bergner, J. B., Rajappan, M., & Öberg, K. I. 2022, *ApJ*, 933, 206
- Bjerkeli, P., Ramsey, J. P., Harsono, D., et al. 2019, *A&A*, 631, A64
- Bjerkeli, P., van der Wiel, M. H. D., Harsono, D., Ramsey, J. P., & Jørgensen, J. K. 2016, *Nature*, 540, 406
- Boogert, A. C. A., Gerakines, P. A., & Whittet, D. C. B. 2015, *ARA&A*, 53, 541
- Brown, W. A. & Bolina, A. S. 2007, *MNRAS*, 374, 1006
- Ceccarelli, C. 2004, in *Astronomical Society of the Pacific Conference Series*, Vol. 323, *Star Formation in the Interstellar Medium: In Honor of David Hollenbach*, ed. D. Johnstone, F. C. Adams, D. N. C. Lin, D. A. Neufeld, & E. C. Ostriker, 195
- Ceccarelli, C., Caselli, P., Herbst, E., Tielens, A. G. G. M., & Caux, E. 2007, in *Protostars and Planets V*, ed. B. Reipurth, D. Jewitt, & K. Keil, 47
- Ceccarelli, C., Codella, C., Balucani, N., et al. 2023, in *Astronomical Society of the Pacific Conference Series*, Vol. 534, *Protostars and Planets VII*, ed. S. Inutsuka, Y. Aikawa, T. Muto, K. Tomida, & M. Tamura, 379
- Collings, M. P., Anderson, M. A., Chen, R., et al. 2004, *MNRAS*, 354, 1133
- Cuppen, H. M., van Dishoeck, E. F., Herbst, E., & Tielens, A. G. G. M. 2009, *A&A*, 508, 275
- Drozdovskaya, M. N., van Dishoeck, E. F., Jørgensen, J. K., et al. 2018, *MNRAS*, 476, 4949
- Drozdovskaya, M. N., Walsh, C., Visser, R., Harsono, D., & van Dishoeck, E. F. 2015, *MNRAS*, 451, 3836
- Encalada, F. J., Looney, L. W., Takakuwa, S., et al. 2024, *ApJ*, 966, 32
- Fedoseev, G., Cuppen, H. M., Ioppolo, S., Lamberts, T., & Linnartz, H. 2015, *MNRAS*, 448, 1288
- Feeley-Johansson, A., Aikawa, Y., Takakuwa, S., et al. 2025, Submitted to *ApJ*
- Flores, C., Ohashi, N., Tobin, J. J., et al. 2023, *ApJ*, 958, 98
- Fockenberg, C. & Preses, J. M. 2002, *Journal of Physical Chemistry A*, 106, 2924
- Frank, A., Ray, T. P., Cabrit, S., et al. 2014, in *Protostars and Planets VI*, ed. H. Beuther, R. S. Klessen, C. P. Dullemond, & T. Henning, 451–474
- Fuchs, G. W., Cuppen, H. M., Ioppolo, S., et al. 2009, *A&A*, 505, 629
- Garufi, A., Podio, L., Codella, C., et al. 2022, *A&A*, 658, A104
- Gavino, S., Jørgensen, J. K., Sharma, R., et al. 2024, *ApJ*, 974, 21
- Guzmán, V. V., Pety, J., Goicoechea, J. R., et al. 2015, *ApJ*, 800, L33
- Han, I., Kwon, W., Aso, Y., et al. 2025, *ApJ* in press, arXiv:2506.16569
- Harsono, D., Bjerkeli, P., van der Wiel, M. H. D., et al. 2018, *Nature Astronomy*, 2, 646
- Herbst, E. & van Dishoeck, E. F. 2009, *ARA&A*, 47, 427
- Hiraoka, K., Ohashi, N., Kihara, Y., et al. 1994, *Chemical Physics Letters*, 229, 408
- Hsieh, T.-H., Murillo, N. M., Belloche, A., et al. 2019, *ApJ*, 884, 149
- Hsieh, T. H., Segura-Cox, D. M., Pineda, J. E., et al. 2023, *A&A*, 669, A137
- Jhan, K.-S., Lee, C.-F., Johnstone, D., et al. 2022, *ApJ*, 931, L5
- Jørgensen, J. K., Belloche, A., & Garrod, R. T. 2020, *ARA&A*, 58, 727
- Jørgensen, J. K., Schöier, F. L., & van Dishoeck, E. F. 2002, *A&A*, 389, 908
- Jørgensen, J. K., Schöier, F. L., & van Dishoeck, E. F. 2005, *A&A*, 437, 501
- Kido, M., Takakuwa, S., Saigo, K., et al. 2023, *ApJ*, 953, 190
- Kim, C.-H., Lee, J.-E., Peña, C. C., et al. 2024, *ApJ*, 961, 108
- Kristensen, L. E., van Dishoeck, E. F., van Kempen, T. A., et al. 2010, *A&A*, 516, A57
- Lada, C. J. & Wilking, B. A. 1984, *ApJ*, 287, 610
- Lee, J.-E., Kim, C.-H., Lee, S., et al. 2024, *ApJ*, 966, 119
- Lee, J.-E., Matsumoto, T., Kim, H.-J., et al. 2023, *ApJ*, 953, 82
- Lee, S., Lee, J.-E., & Bergin, E. A. 2015, *ApJS*, 217, 30
- Lee, S., Lee, J.-E., Bergin, E. A., & Park, Y.-S. 2014, *ApJS*, 213, 33
- Lin, S.-J., Yen, H.-W., & Lai, S.-P. 2024, *AJ*, 168, 107
- Lin, Z.-Y. D., Li, Z.-Y., Tobin, J. J., et al. 2023, *ApJ*, 951, 9
- Loomis, R. A., Cleeves, L. I., Öberg, K. I., Guzman, V. V., & Andrews, S. M. 2015, *ApJ*, 809, L25
- Mangum, J. G. & Wootten, A. 1993, *ApJS*, 89, 123
- Maret, S., Ceccarelli, C., Caux, E., et al. 2004, *A&A*, 416, 577
- Martin-Pintado, J., Bachiller, R., & Fuente, A. 1992, *A&A*, 254, 315
- Maury, A. J., André, P., Testi, L., et al. 2019, *A&A*, 621, A76
- McMullin, J. P., Waters, B., Schiebel, D., Young, W., & Golap, K. 2007, in *Astronomical Society of the Pacific Conference Series*, Vol. 376, *Astronomical Data Analysis Software and Systems XVI*, ed. R. A. Shaw, F. Hill, & D. J. Bell, 127
- Mercimek, S., Podio, L., Codella, C., et al. 2023, *MNRAS*, 522, 2384
- Millar, T. J., Bennett, A., & Herbst, E. 1989, *ApJ*, 340, 906
- Murillo, N. M., van Dishoeck, E. F., Hacar, A., Harsono, D., & Jørgensen, J. K. 2022, *A&A*, 658, A53
- Murillo, N. M., van Dishoeck, E. F., van der Wiel, M. H. D., et al. 2018, *A&A*, 617, A120
- Nakamura, F. & Li, Z.-Y. 2014, *ApJ*, 783, 115
- Narayanan, S., Williams, J. P., Tobin, J. J., et al. 2023, *ApJ*, 958, 20
- Noble, J. A., Theule, P., Mispelaer, F., et al. 2012, *A&A*, 543, A5
- Öberg, K. I. & Bergin, E. A. 2021, *Phys. Rep.*, 893, 1
- Öberg, K. I., Facchini, S., & Andersson, D. E. 2023, *ARA&A*, 61, 287
- Öberg, K. I., Guzmán, V. V., Merchantz, C. J., et al. 2017, *ApJ*, 839, 43
- Offner, S. S. R. & Arce, H. G. 2014, *ApJ*, 784, 61
- Ohashi, N., Saigo, K., Aso, Y., et al. 2014, *ApJ*, 796, 131
- Ohashi, N., Tobin, J. J., Jørgensen, J. K., et al. 2023, *ApJ*, 951, 8
- Oya, Y., Sakai, N., Sakai, T., et al. 2014, *ApJ*, 795, 152
- Penteado, E. M., Walsh, C., & Cuppen, H. M. 2017, *ApJ*, 844, 71
- Phuong, N. T., Lee, C. W., Tobin, J. J., et al. 2025, *ApJ* in press, arXiv:2508.07212
- Pineda, J. E., Arzoumanian, D., Andre, P., et al. 2023, in *Astronomical Society of the Pacific Conference Series*, Vol. 534, *Protostars and Planets VII*, ed. S. Inutsuka, Y. Aikawa, T. Muto, K. Tomida, & M. Tamura, 233
- Pineda, J. E., Segura-Cox, D., Caselli, P., et al. 2020, *Nature Astronomy*, 4, 1158
- Plunkett, A. L., Arce, H. G., Mardones, D., et al. 2015, *Nature*, 527, 70
- Podio, L., Ceccarelli, C., Codella, C., et al. 2024, *A&A*, 688, L22
- Podio, L., Codella, C., Gueth, F., et al. 2015, *A&A*, 581, A85
- Pontoppidan, K. M., Salyk, C., Bergin, E. A., et al. 2014, in *Protostars and Planets VI*, ed. H. Beuther, R. S. Klessen, C. P. Dullemond, & T. Henning, 363–385
- Qasim, D., Chuang, K. J., Fedoseev, G., et al. 2018, *A&A*, 612, A83
- Sai, J., Yen, H.-W., Ohashi, N., et al. 2023, *ApJ*, 954, 67
- Sakai, N., Oya, Y., Higuchi, A. E., et al. 2017, *MNRAS*, 467, L76
- Sakai, N., Oya, Y., Sakai, T., et al. 2014a, *ApJ*, 791, L38
- Sakai, N., Sakai, T., Hirota, T., et al. 2014b, *Nature*, 507, 78
- Santamaría-Miranda, A., de Gregorio-Monsalvo, I., Ohashi, N., et al. 2024, *A&A*, 690, A46
- Sharma, R., Jørgensen, J. K., Gavino, S., et al. 2023, *ApJ*, 954, 69
- Sharma, R., Tobin, J. J., Sheehan, P. D., et al. 2020, *ApJ*, 904, 78
- Simons, M. A. J., Lamberts, T., & Cuppen, H. M. 2020, *A&A*, 634, A52
- Snyder, L. E., Buhl, D., Zuckerman, B., & Palmer, P. 1969, *Phys. Rev. Lett.*, 22, 679
- Tabone, B., Cabrit, S., Bianchi, E., et al. 2017, *A&A*, 607, L6
- Tafalla, M., Santiago-García, J., Hacar, A., & Bachiller, R. 2010, *A&A*, 522, A91
- Takahashi, S., Machida, M. N., Omura, M., et al. 2024, *ApJ*, 964, 48
- Takakuwa, S., Saigo, K., Kido, M., et al. 2024, *ApJ*, 964, 24
- Tang, X. D., Henkel, C., Chen, C. H. R., et al. 2017, *A&A*, 600, A16
- Testi, L., Birnstiel, T., Ricci, L., et al. 2014, in *Protostars and Planets VI*, ed. H. Beuther, R. S. Klessen, C. P. Dullemond, & T. Henning, 339–361
- Thieme, T. J., Lai, S.-P., Lin, S.-J., et al. 2022, *ApJ*, 925, 32
- Thieme, T. J., Lai, S.-P., Ohashi, N., et al. 2023, *ApJ*, 958, 60
- Turner, B. E. 2001, *ApJS*, 136, 579
- Tychoniec, Ł., Manara, C. F., Rosotti, G. P., et al. 2020, *A&A*, 640, A19
- Tychoniec, Ł., van Dishoeck, E. F., van't Hoff, M. L. R., et al. 2021, *A&A*, 655, A65

- Valdivia-Mena, M. T., Pineda, J. E., Caselli, P., et al. 2024, A&A, 687, A71
- Valdivia-Mena, M. T., Pineda, J. E., Segura-Cox, D. M., et al. 2022, A&A, 667, A12
- Valdivia-Mena, M. T., Pineda, J. E., Segura-Cox, D. M., et al. 2023, A&A, 677, A92
- van der Marel, N., van Dishoeck, E. F., Bruderer, S., & van Kempen, T. A. 2014, A&A, 563, A113
- van der Tak, F. F. S., Black, J. H., Schöier, F. L., Jansen, D. J., & van Dishoeck, E. F. 2007, A&A, 468, 627
- van der Wiel, M. H. D., van der Tak, F. F. S., Ossenkopf, V., et al. 2009, A&A, 498, 161
- van Dishoeck, E. F. & Blake, G. A. 1998, ARA&A, 36, 317
- van Gelder, M. L., Tabone, B., van Dishoeck, E. F., & Godard, B. 2021, A&A, 653, A159
- van 't Hoff, M. L. R., Tobin, J. J., Harsono, D., & van Dishoeck, E. F. 2018, A&A, 615, A83
- van't Hoff, M. L. R., Bergin, E. A., Riley, P., et al. 2024, ApJ, 970, 138
- van't Hoff, M. L. R., Tobin, J. J., Li, Z.-Y., et al. 2023, ApJ, 951, 10
- Visser, R., Kristensen, L. E., Bruderer, S., et al. 2012, A&A, 537, A55
- Vorobyov, E. I., Elbakyan, V. G., Plunkett, A. L., et al. 2018, A&A, 613, A18
- Wakelam, V., Ceccarelli, C., Castets, A., et al. 2005, A&A, 437, 149
- Wang, H., Mundt, R., Henning, T., & Apai, D. 2004, ApJ, 617, 1191
- Watanabe, N. & Kouchi, A. 2002, ApJ, 571, L173
- Willacy, K. 2007, ApJ, 660, 441
- Wilson, T. L. & Rood, R. 1994, ARA&A, 32, 191
- Yamato, Y., Aikawa, Y., Ohashi, N., et al. 2023, ApJ, 951, 11
- Yen, H.-W., Gu, P.-G., Hirano, N., et al. 2019, ApJ, 880, 69
- Yen, H.-W., Koch, P. M., Takakuwa, S., et al. 2017, ApJ, 834, 178
- Yen, H.-W., Takakuwa, S., Koch, P. M., et al. 2015, ApJ, 812, 129

Appendix A: Large-scale moment 8 and moment 9 maps

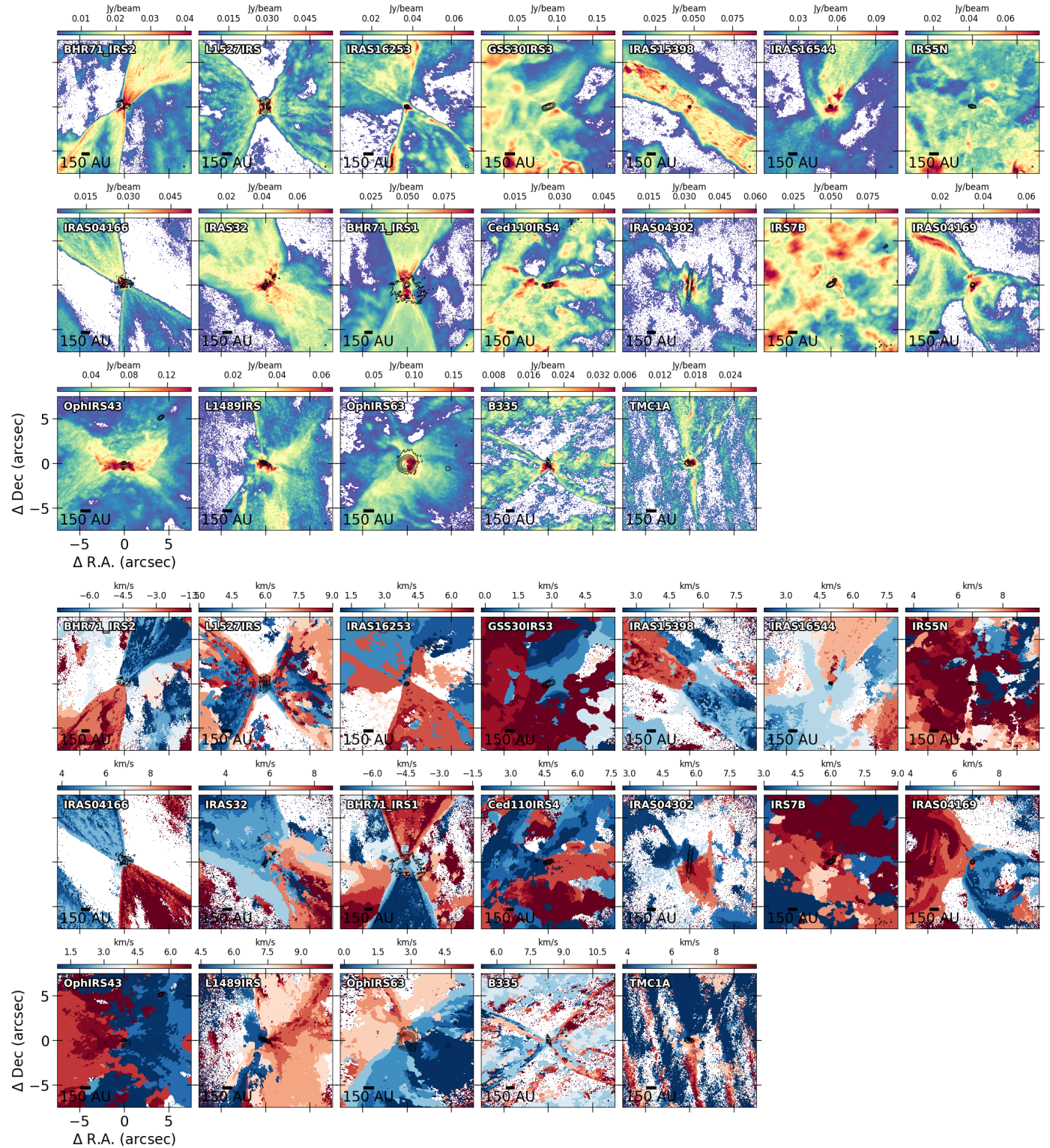


Fig. A.1. Moment 8 (top) and moment 9 (bottom) maps depicting the ^{12}CO (2-1) emission in the inner 15'' region of the nineteen eDisk sources. Moment maps were generated by integrating the regions where $I_v > 3\sigma$, where σ is the rms per channel. The sources are arranged in ascending order of L_{bol} except for B335 and TMC1A, the two sources taken from the archive. The contour lines display the continuum emission at thresholds of 5σ , 20σ , 80σ , and 320σ for each source. The scale bar located at the bottom left shows the 150 au scale in each source, and the synthesized beam is indicated in white at the bottom right corner of each image.

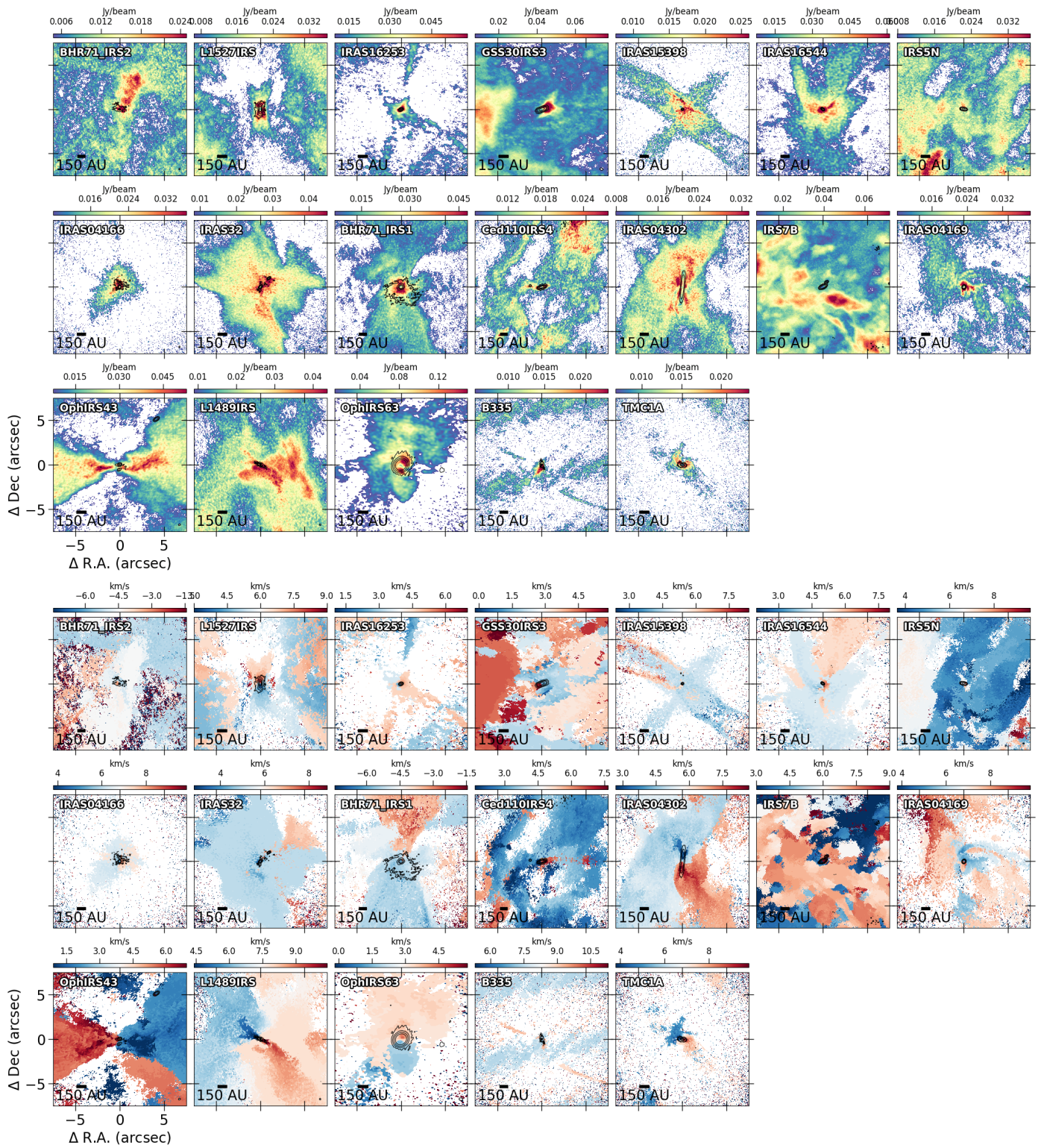


Fig. A.2. Same as Figure A.1 but for ^{13}CO (2–1) instead.

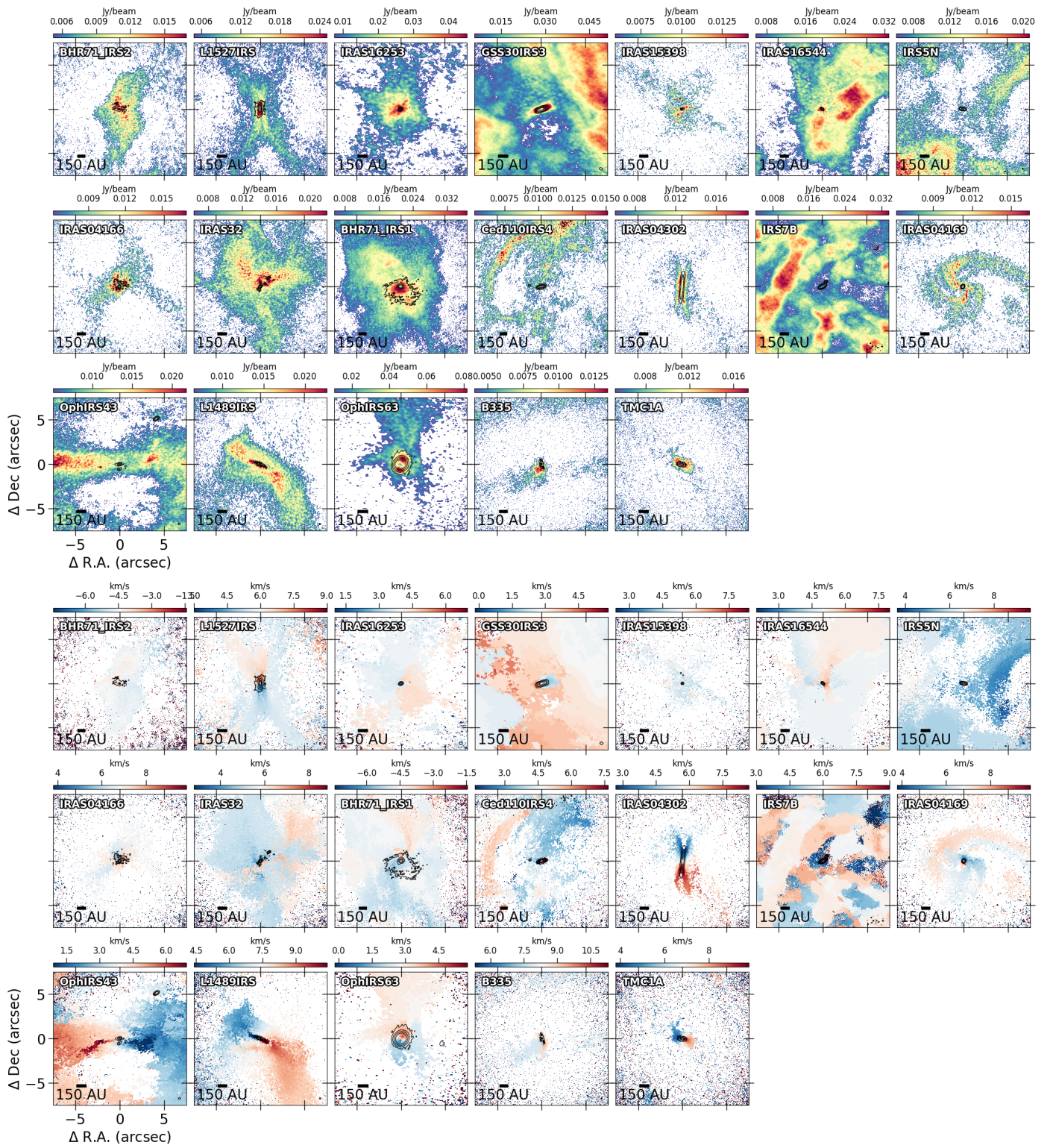


Fig. A.3. Same as Figure A.1 but for C¹⁸O (2–1) instead.

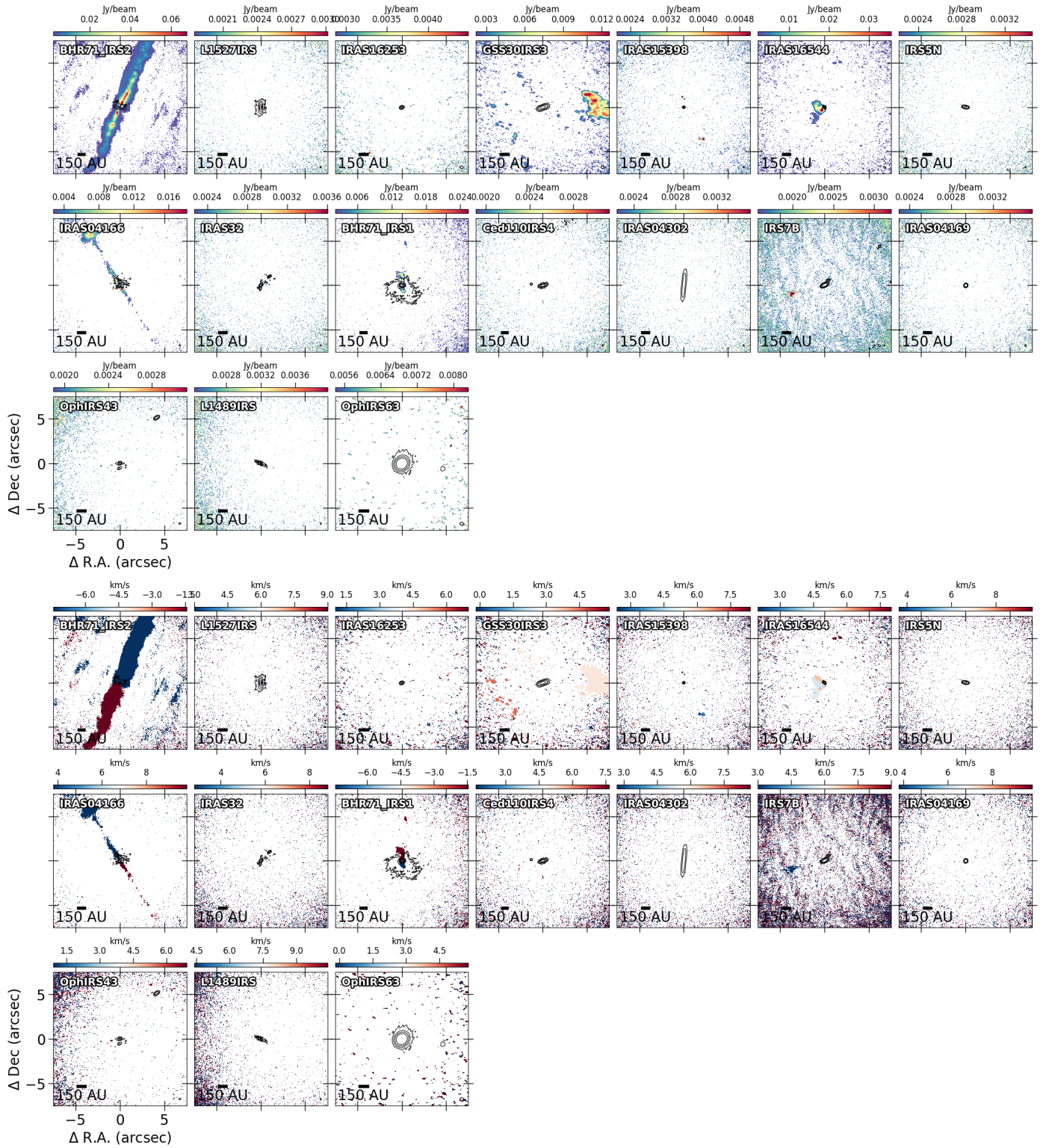


Fig. A.4. Same as Figure A.1 but for SiO (5–4) instead.

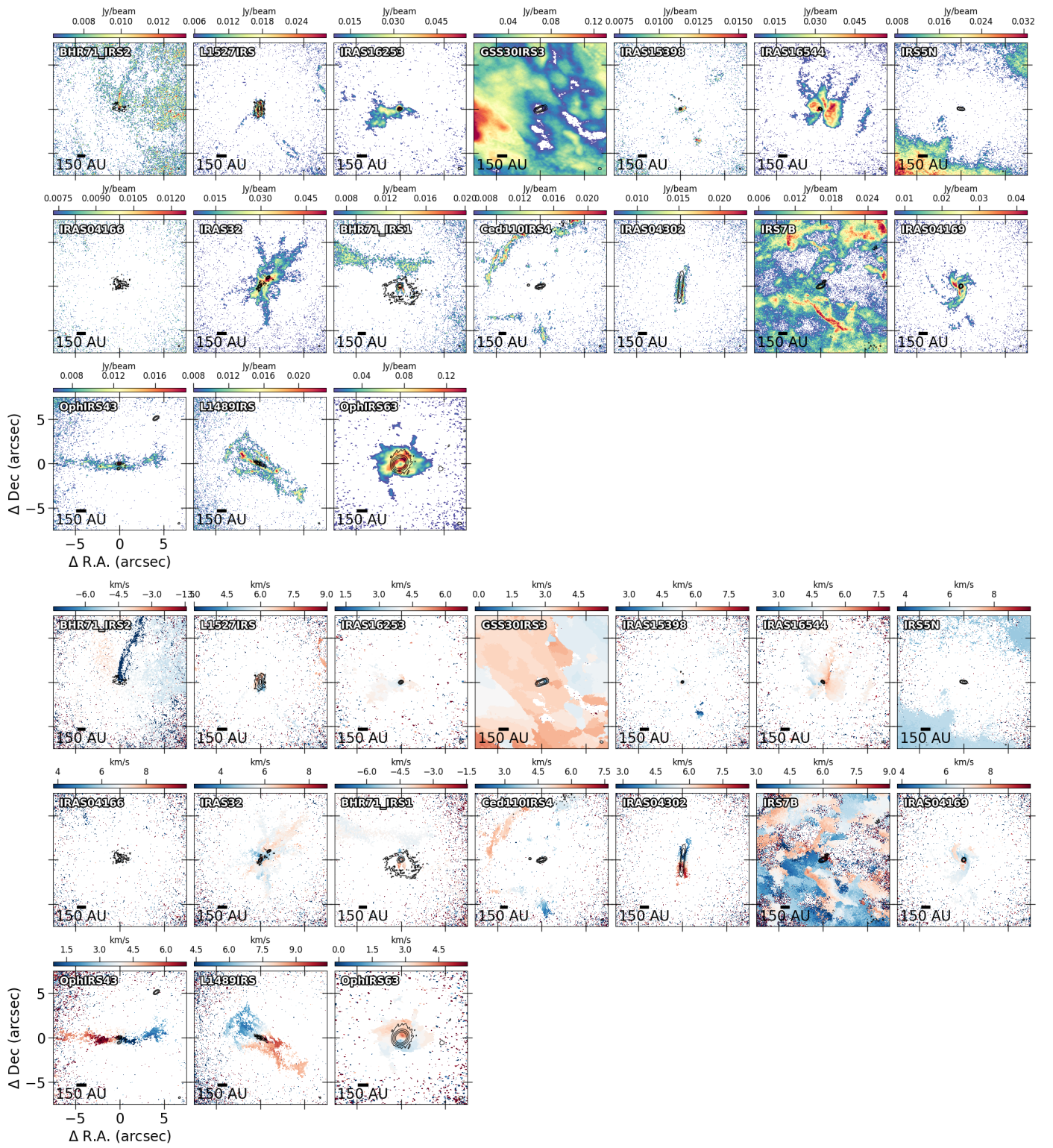


Fig. A.5. Same as Figure A.1 but for SO (6_5-5_4) instead.

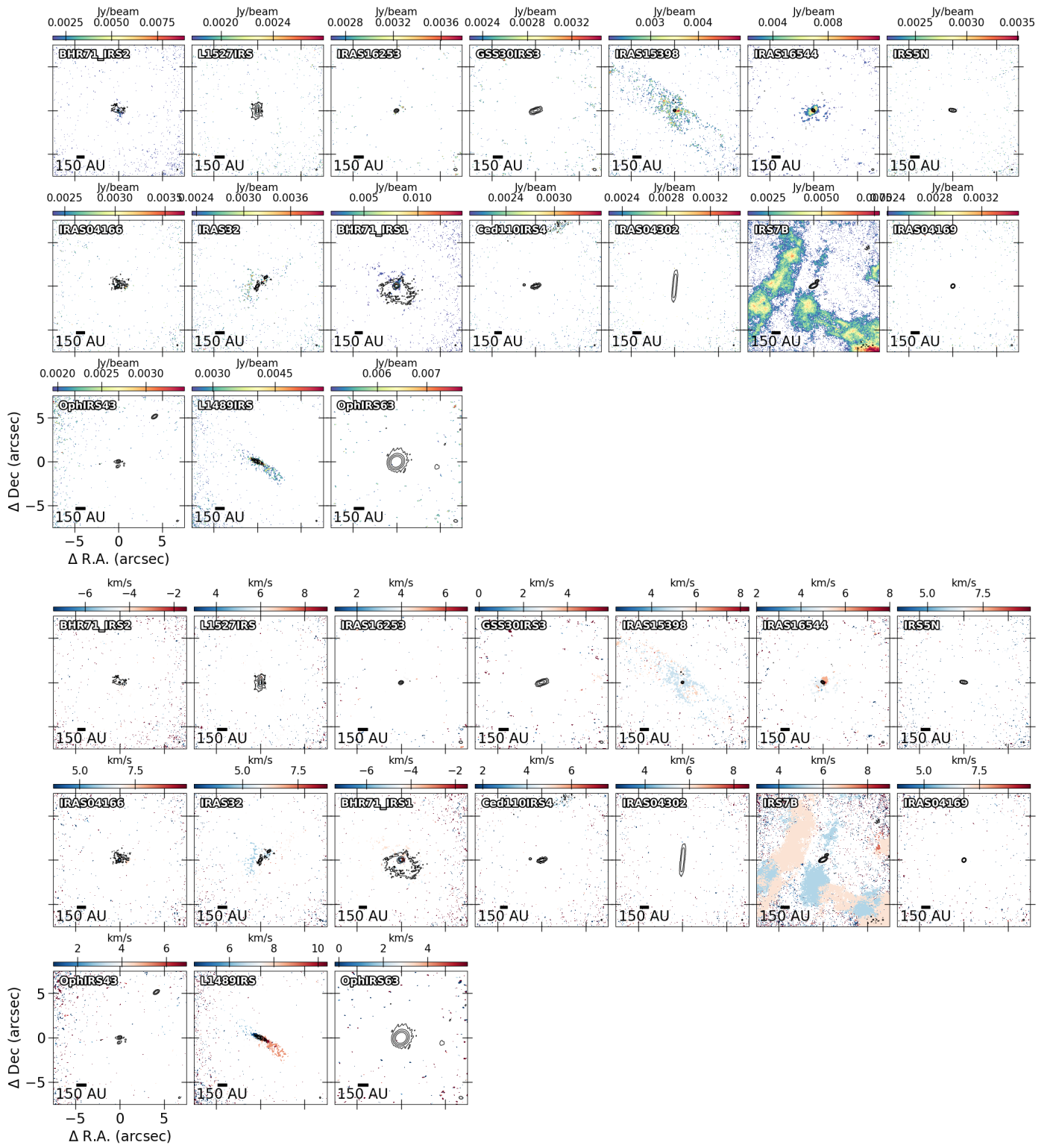


Fig. A.6. Same as Figure A.1 but for DCN (3–2) instead.

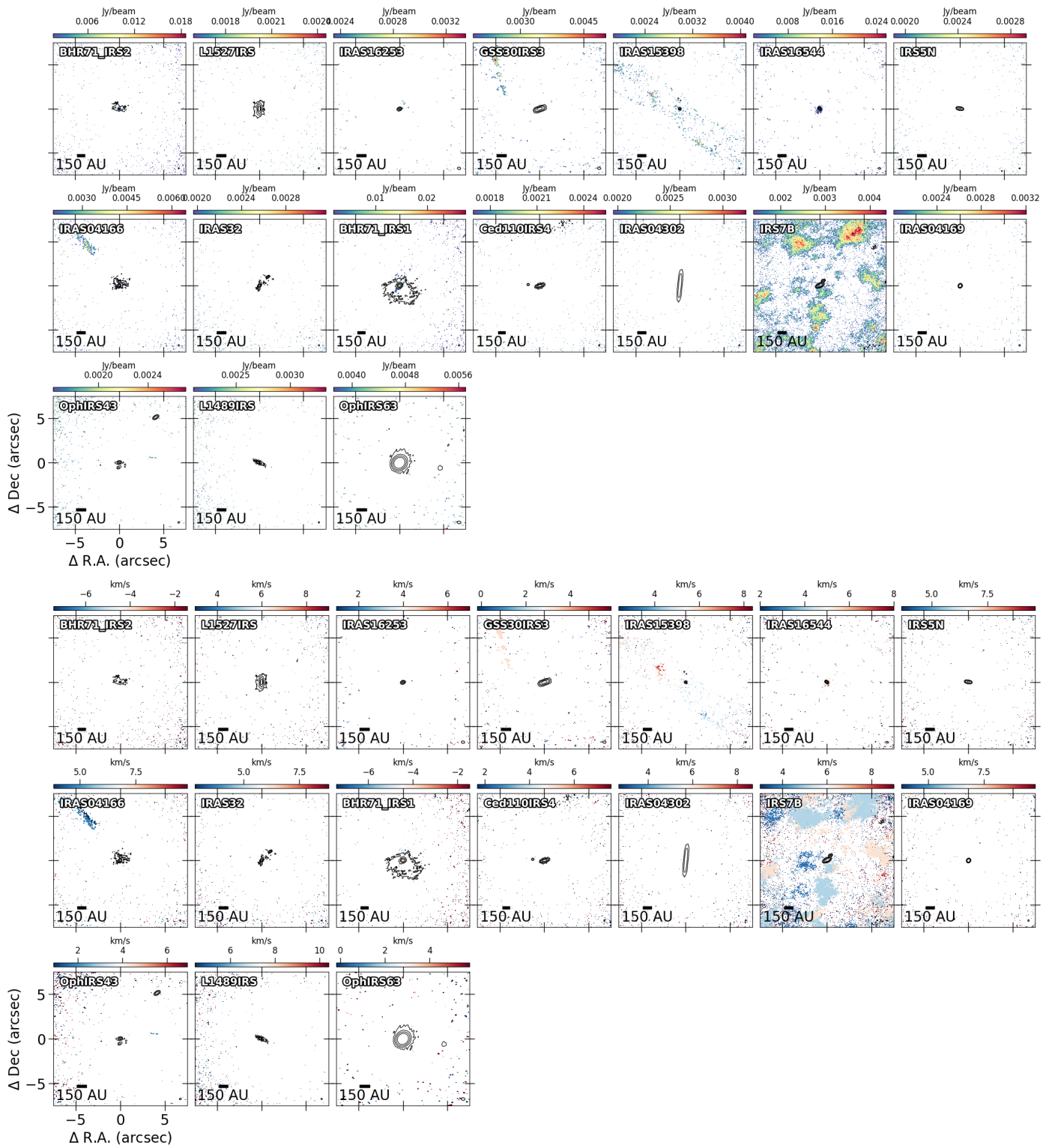


Fig. A.7. Same as Figure A.1 but for CH_3OH (4_2-3_1) instead.

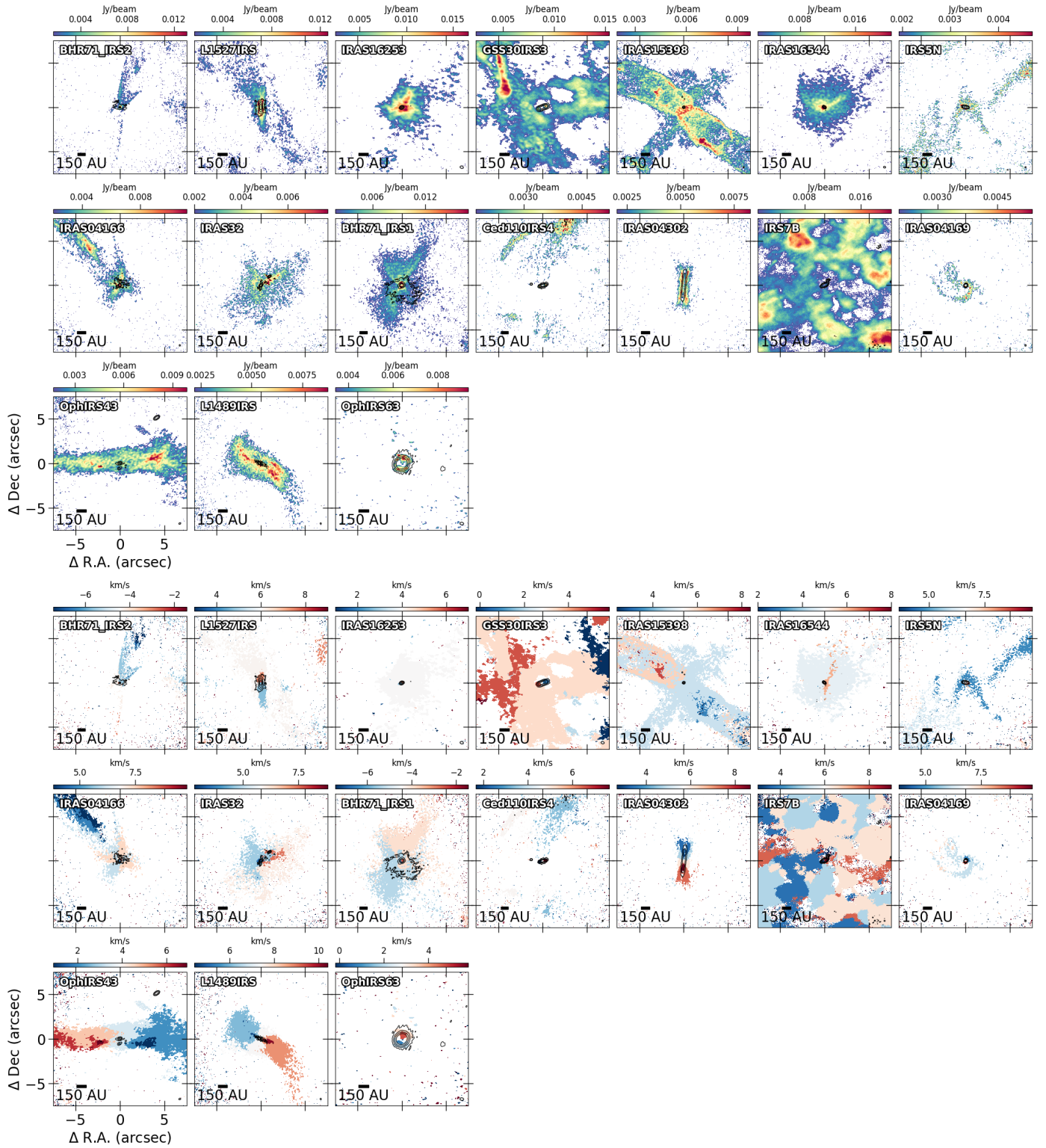


Fig. A.8. Same as Figure A.1 but for H_2CO ($3_{0,3}-2_{0,2}$) instead.

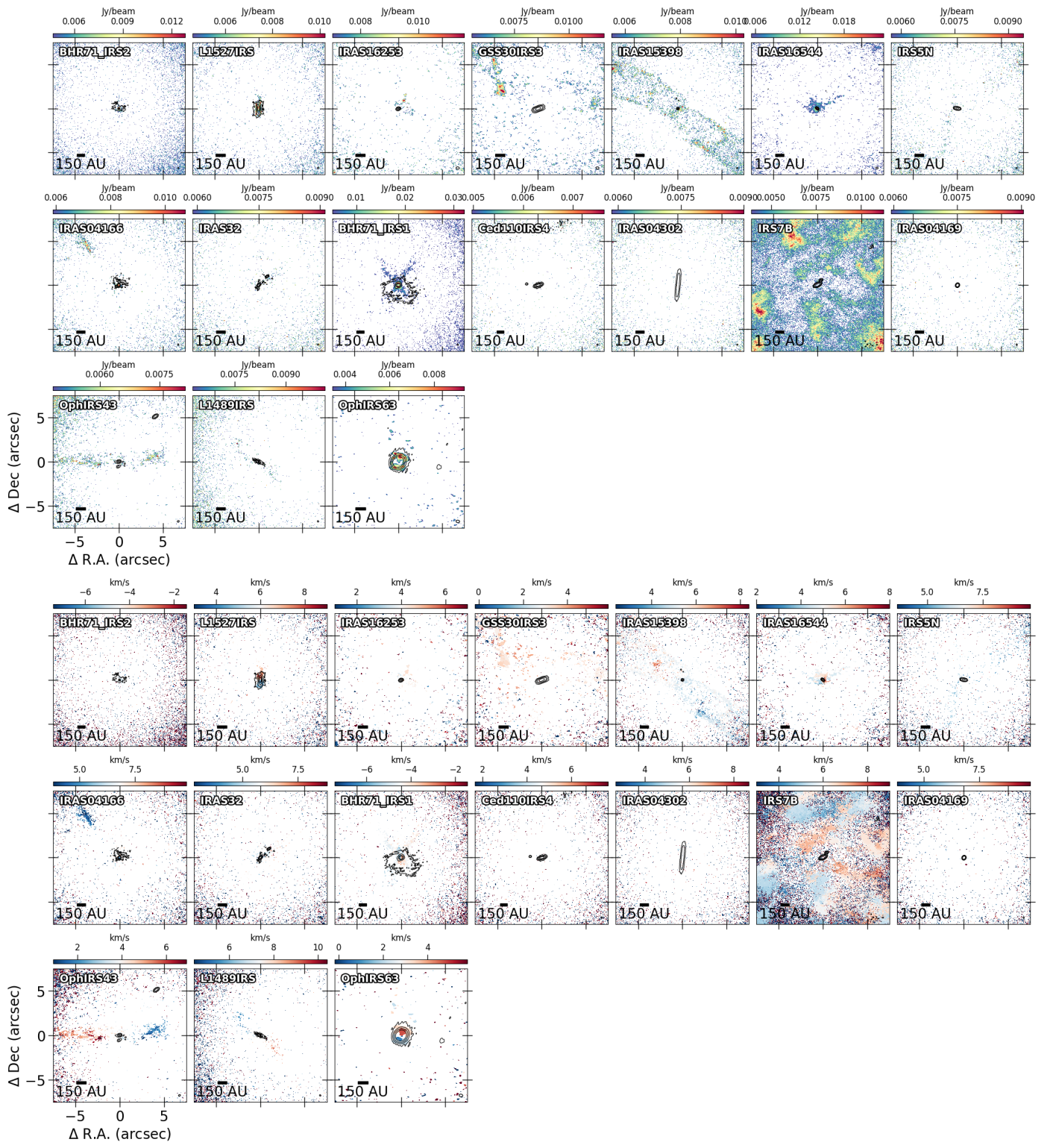


Fig. A.9. Same as Figure A.1 but for H_2CO (3_{2,1} - 2_{2,0}) instead.

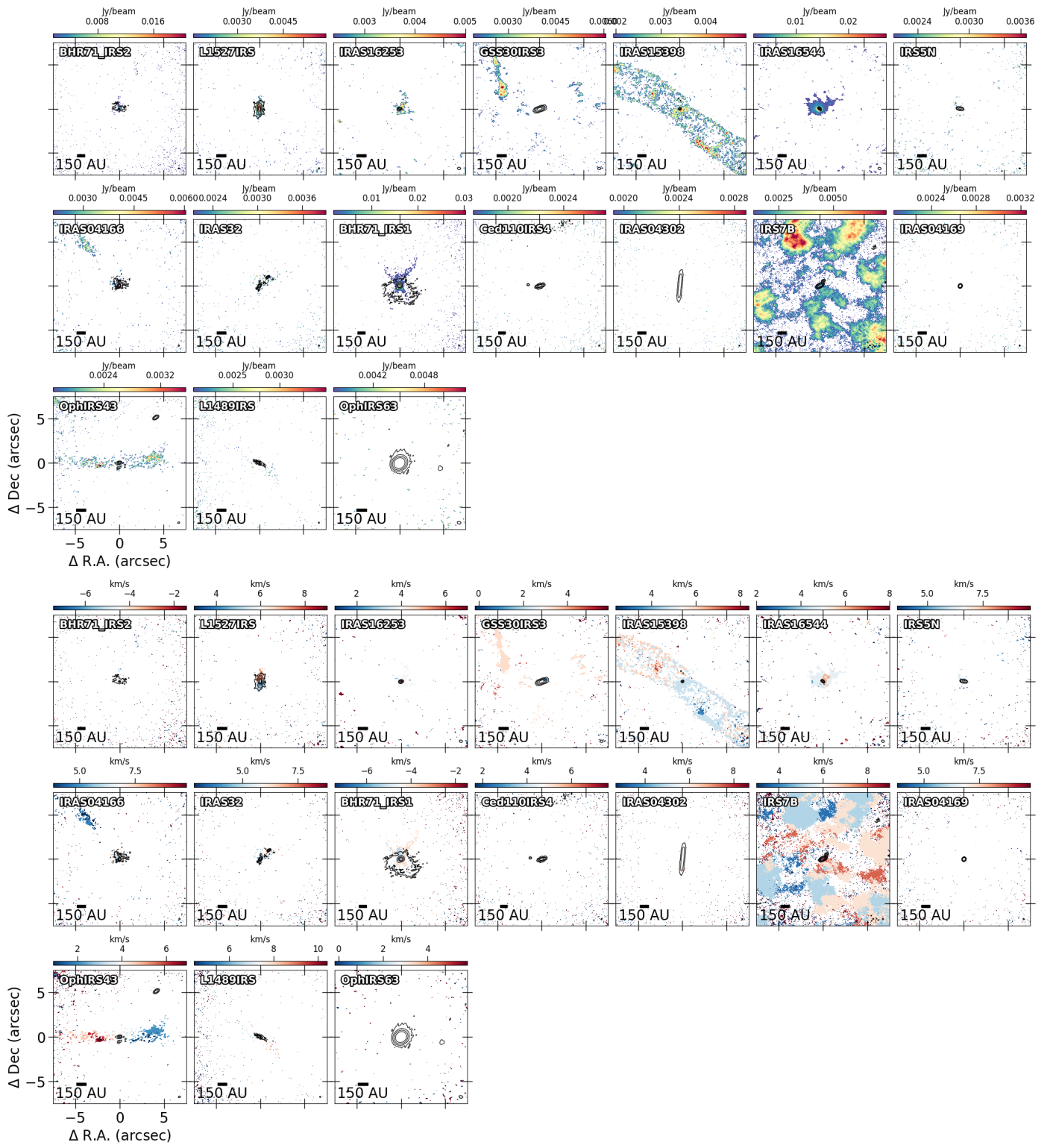


Fig. A.10. Same as Figure A.1 but for H_2CO ($3_{2,2}-2_{2,1}$) instead.

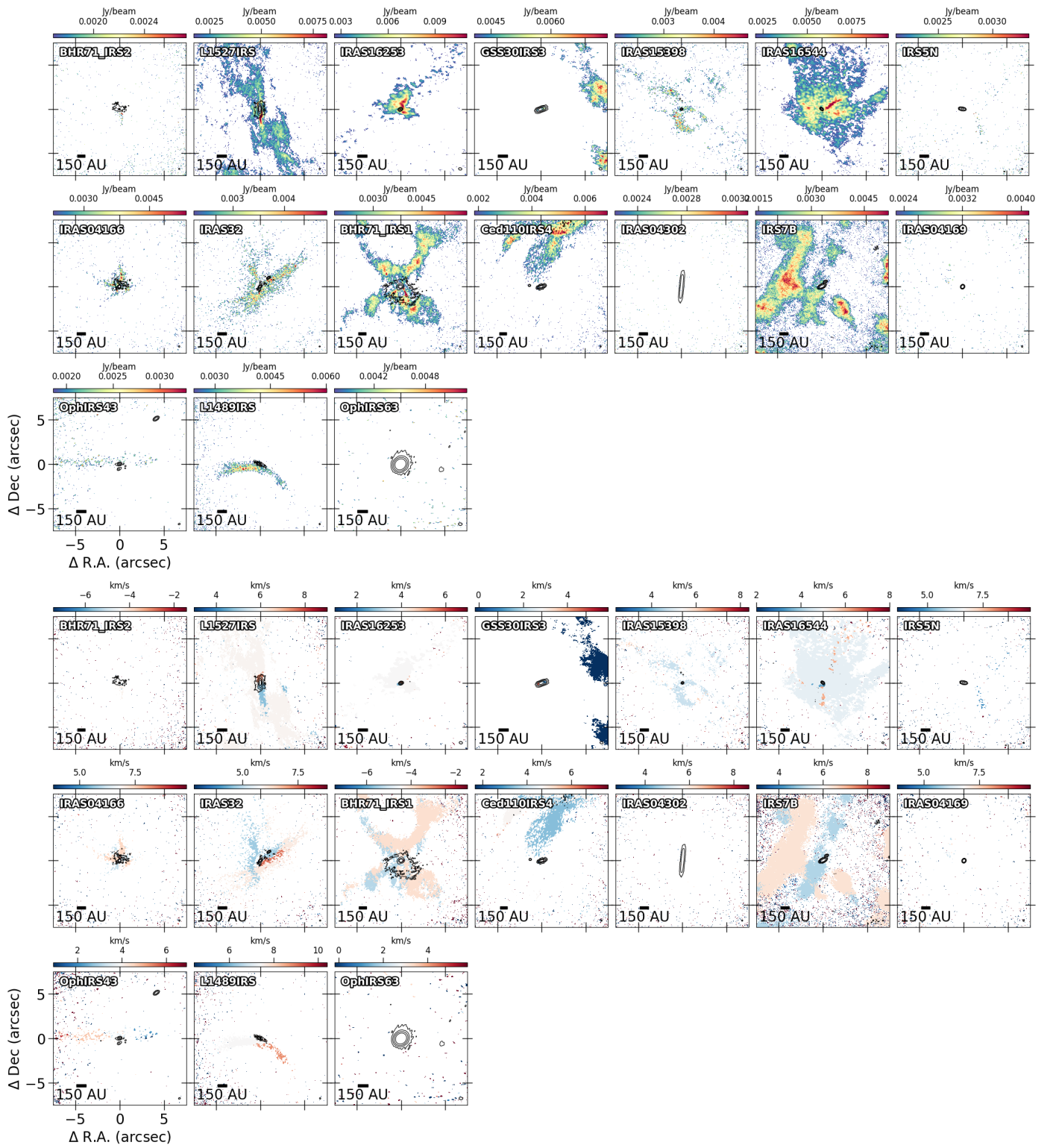


Fig. A.11. Same as Figure A.1 but for the blended $c\text{-C}_3\text{H}_2$ ($6_{0,6}-5_{1,5}$) and ($6_{1,6}-5_{0,5}$) instead.

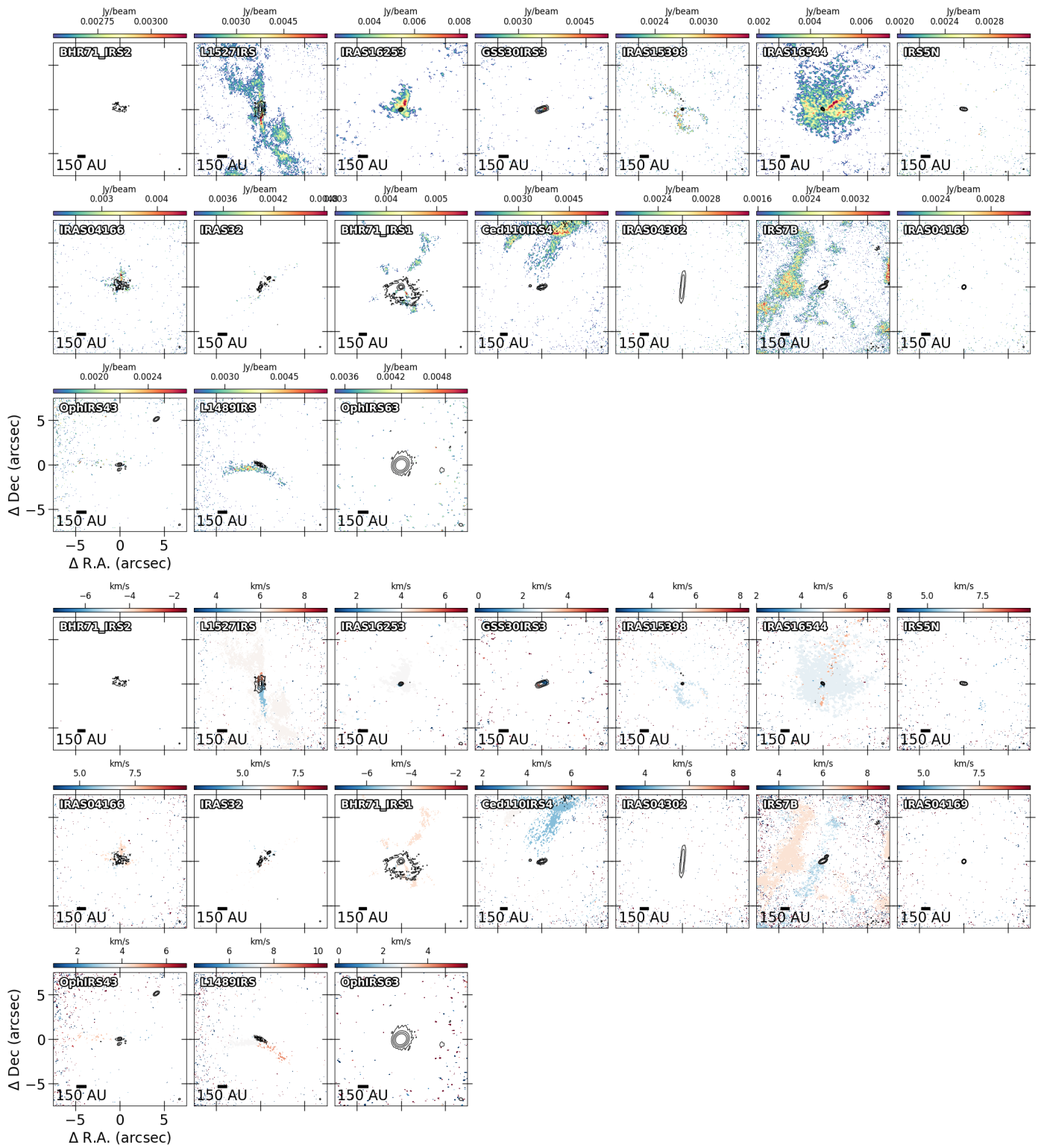


Fig. A.12. Same as Figure A.1 but for $c\text{-C}_3\text{H}_2$ ($5_{1,4}-4_{2,3}$) instead.

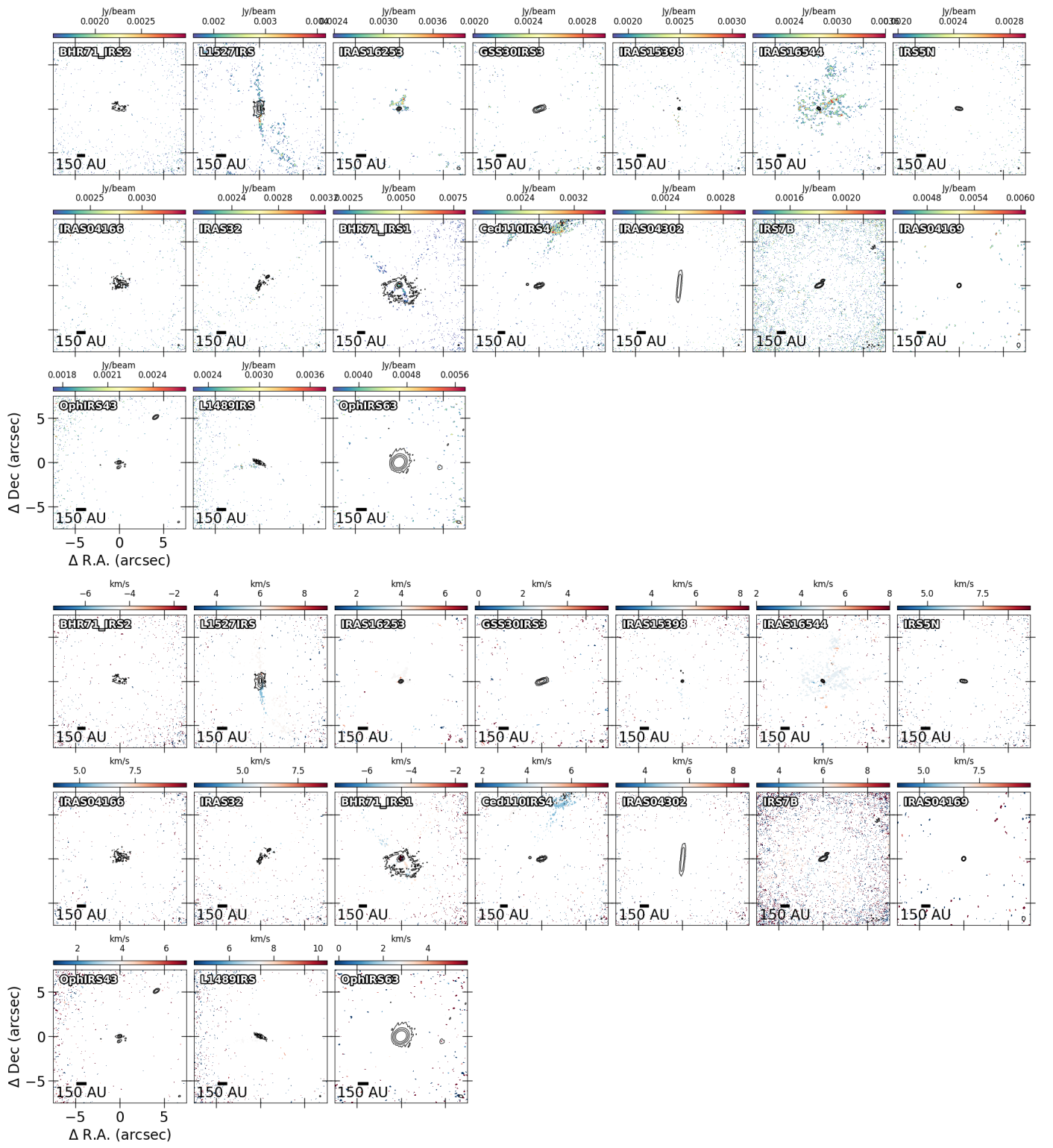


Fig. A.13. Same as Figure A.1 but for $c\text{-C}_3\text{H}_2 (5_{2,4} - 4_{1,3})$ instead.

Appendix B: Zoomed-in small-scale moment 8 and moment 9 maps

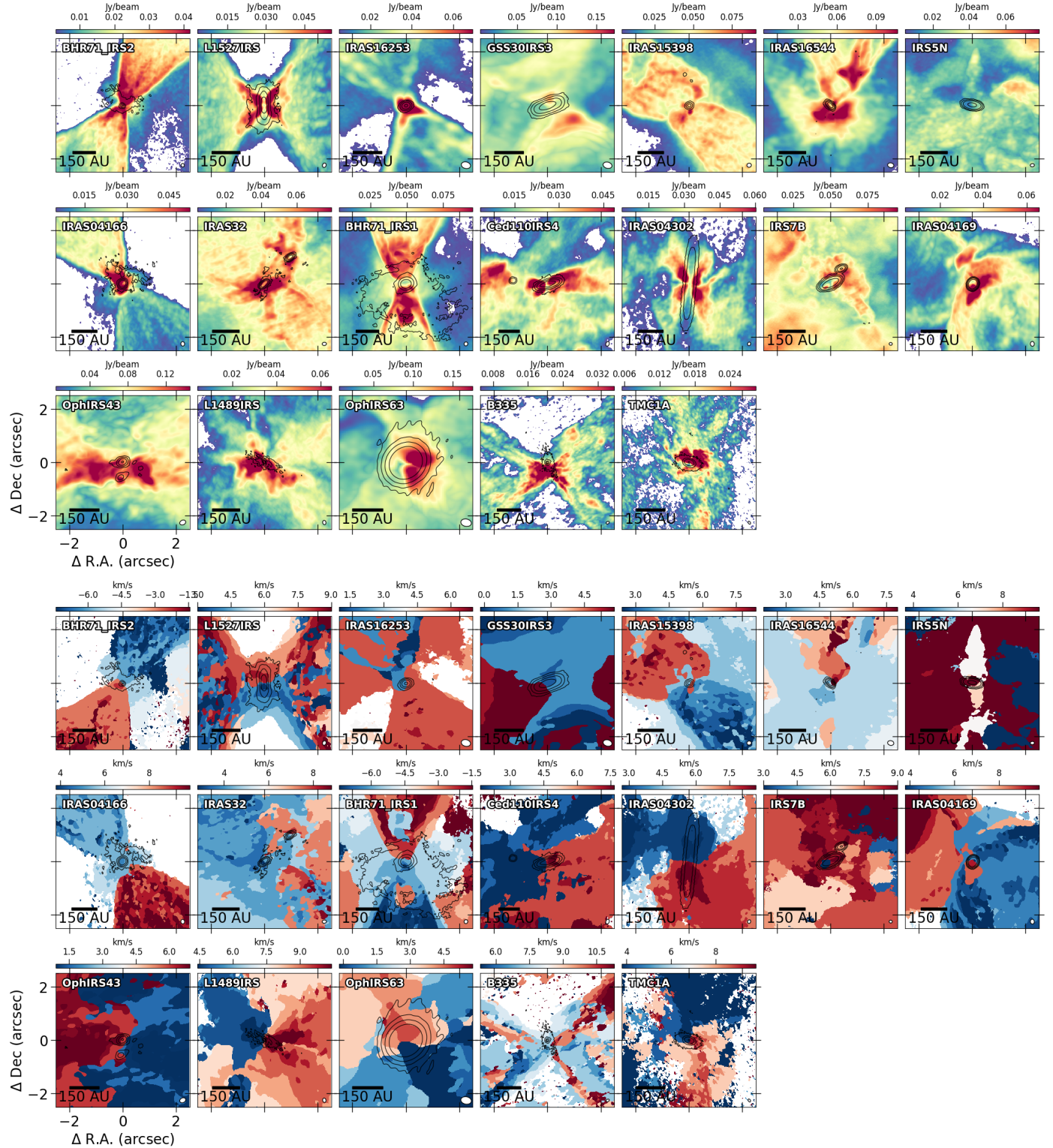


Fig. B.1. Moment 8 (top) and moment 9 (bottom) maps depicting the ^{12}CO (2–1) emission in the inner 5'' region of the nineteen eDisk sources. The moment maps were generated by integrating the regions where $I_{\nu} > 3\sigma$, where σ is the rms per channel. The contour lines display the continuum emission at thresholds of 5σ , 20σ , 80σ , and 320σ for each source. The scale bar is located at the bottom left, and the synthesized beam is indicated in white at the bottom right corner of each image.

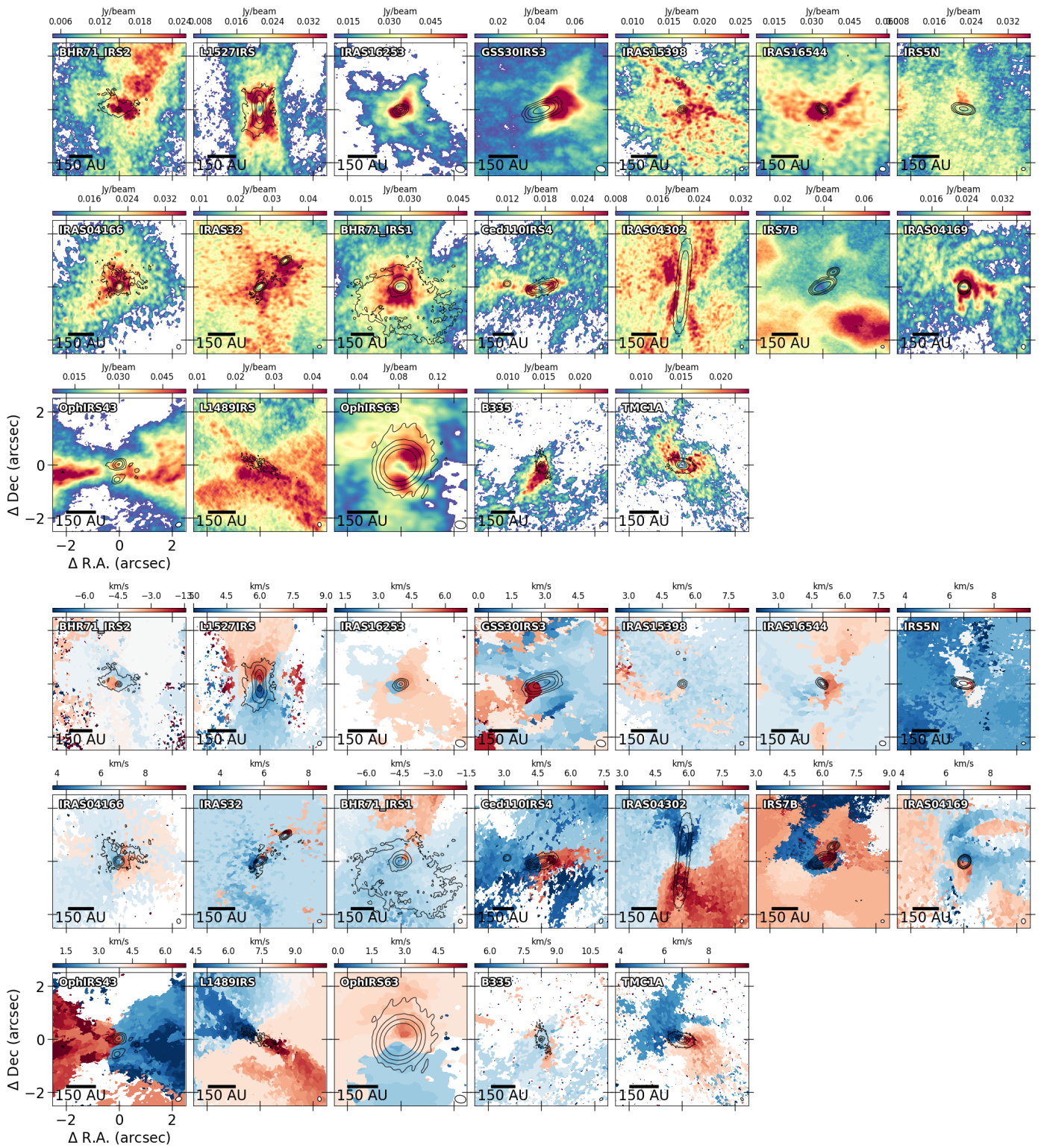


Fig. B.2. Same as Figure B.1 but for ^{13}CO (2–1) instead.

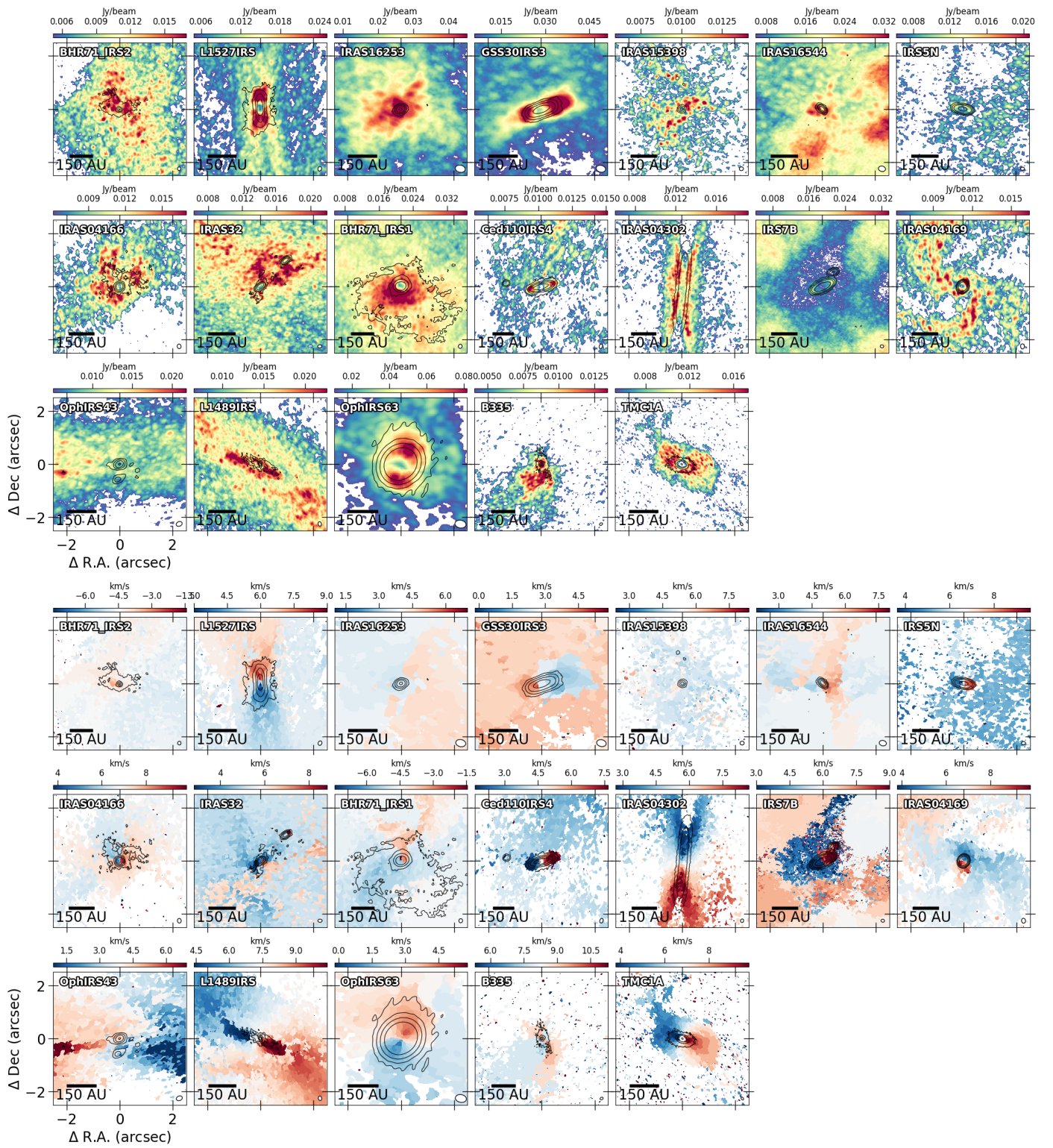


Fig. B.3. Same as Figure B.1 but for C^{18}O (2-1) instead.

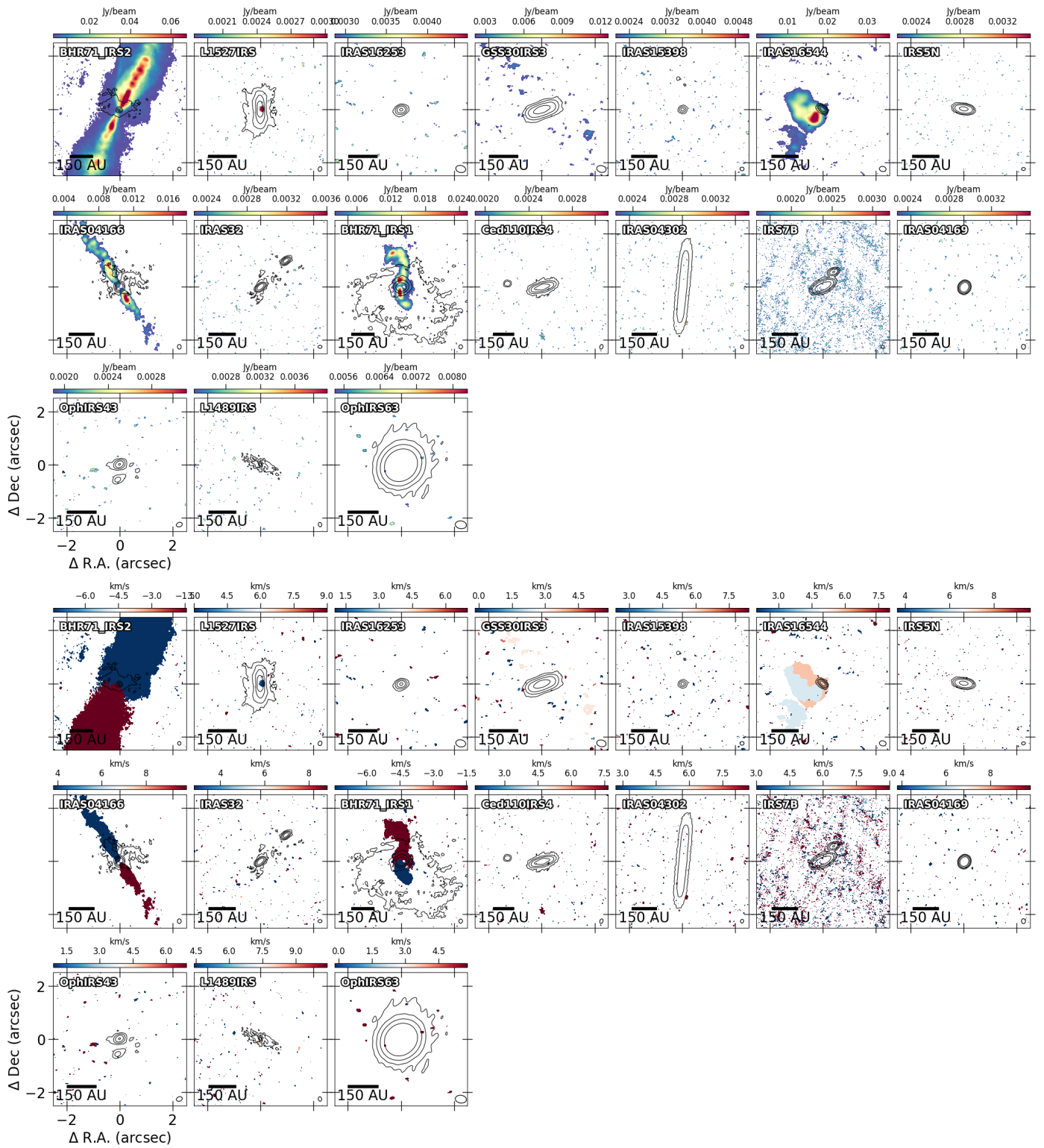


Fig. B.4. Same as Figure B.1 but for SiO (5–4) instead.

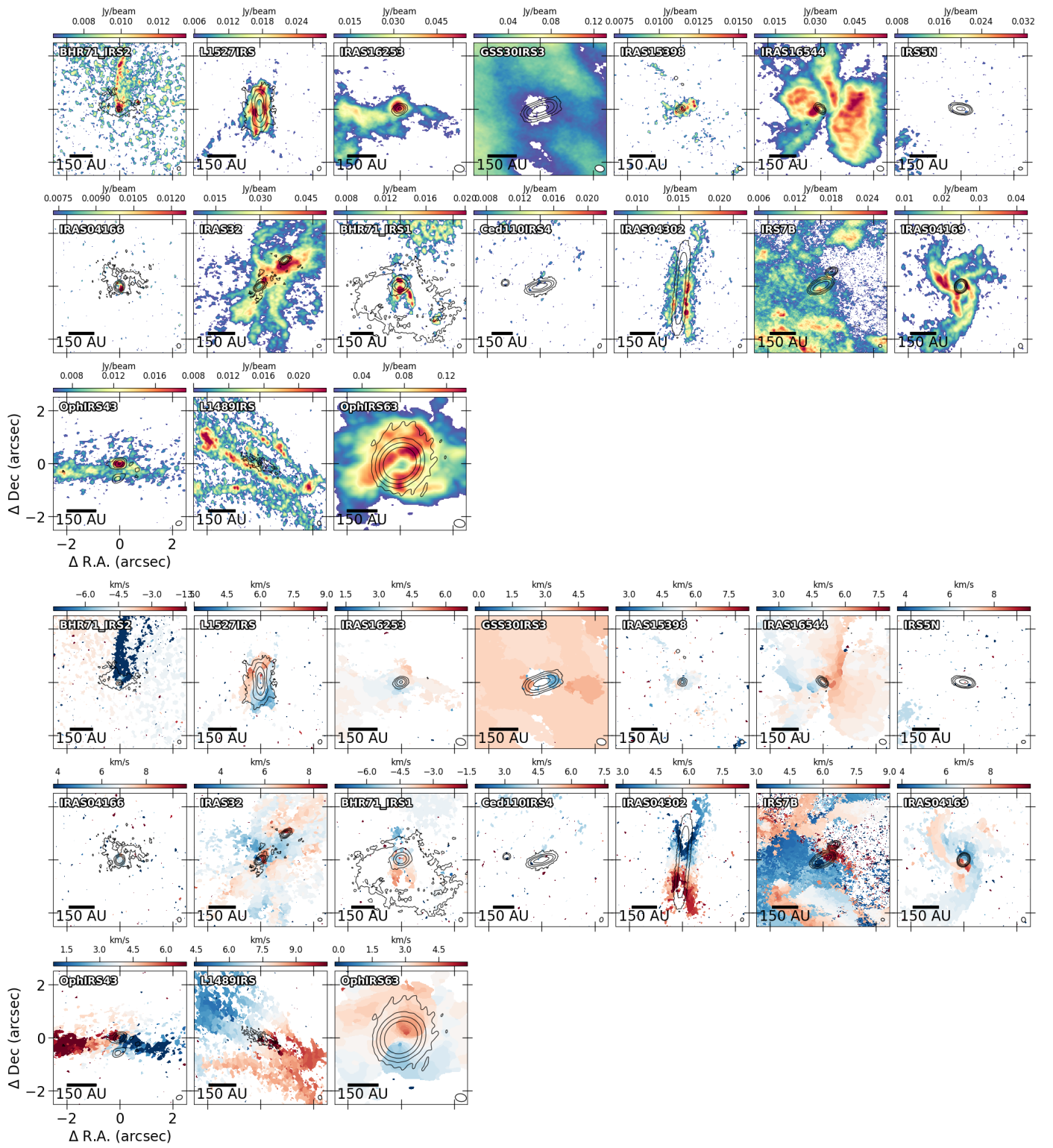


Fig. B.5. Same as Figure B.1 but for SO (6_5-5_4) instead.

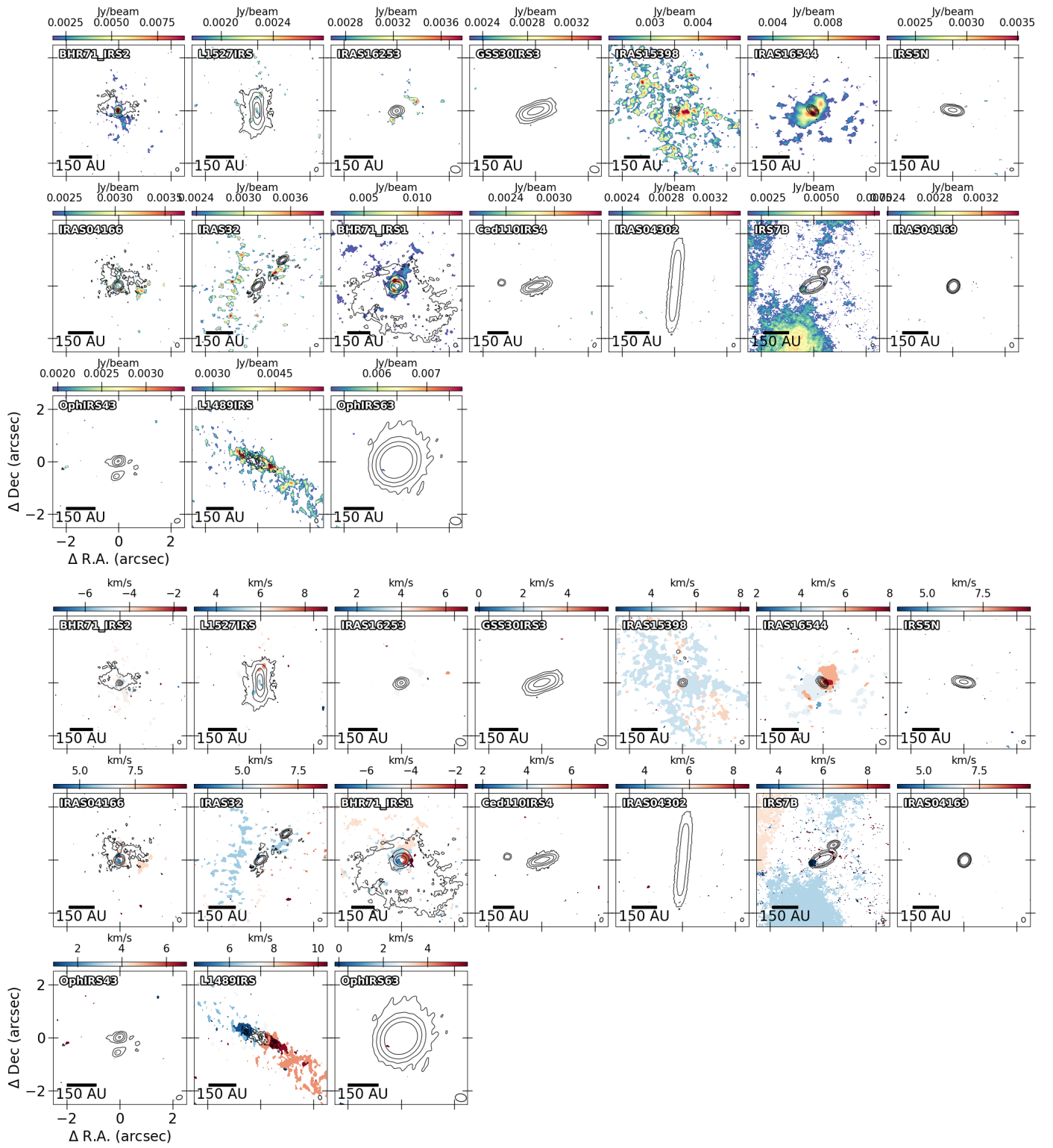


Fig. B.6. Same as Figure B.1 but for DCN (3–2) instead.

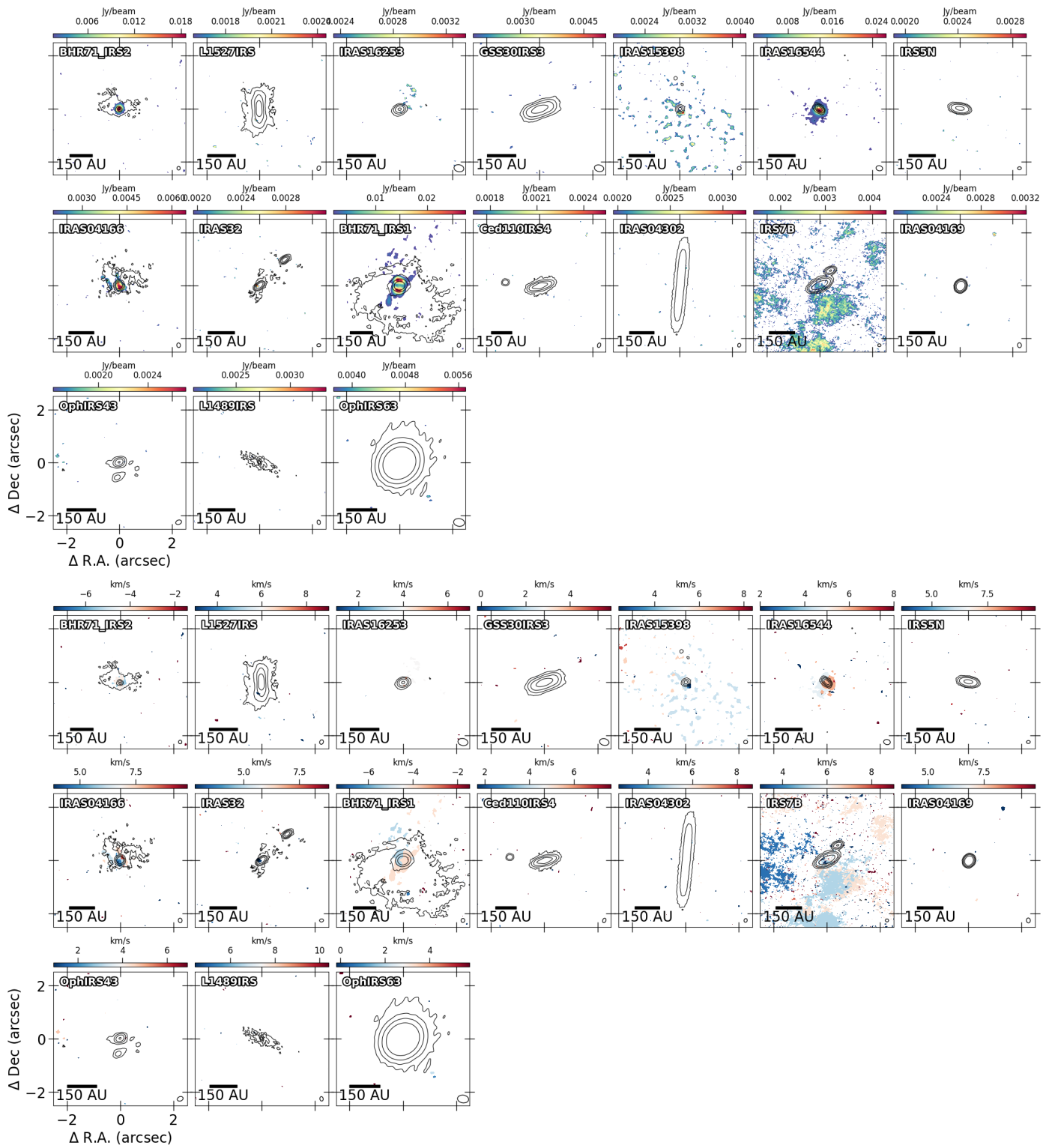


Fig. B.7. Same as Figure B.1 but for CH_3OH (4_2-3_1) instead.

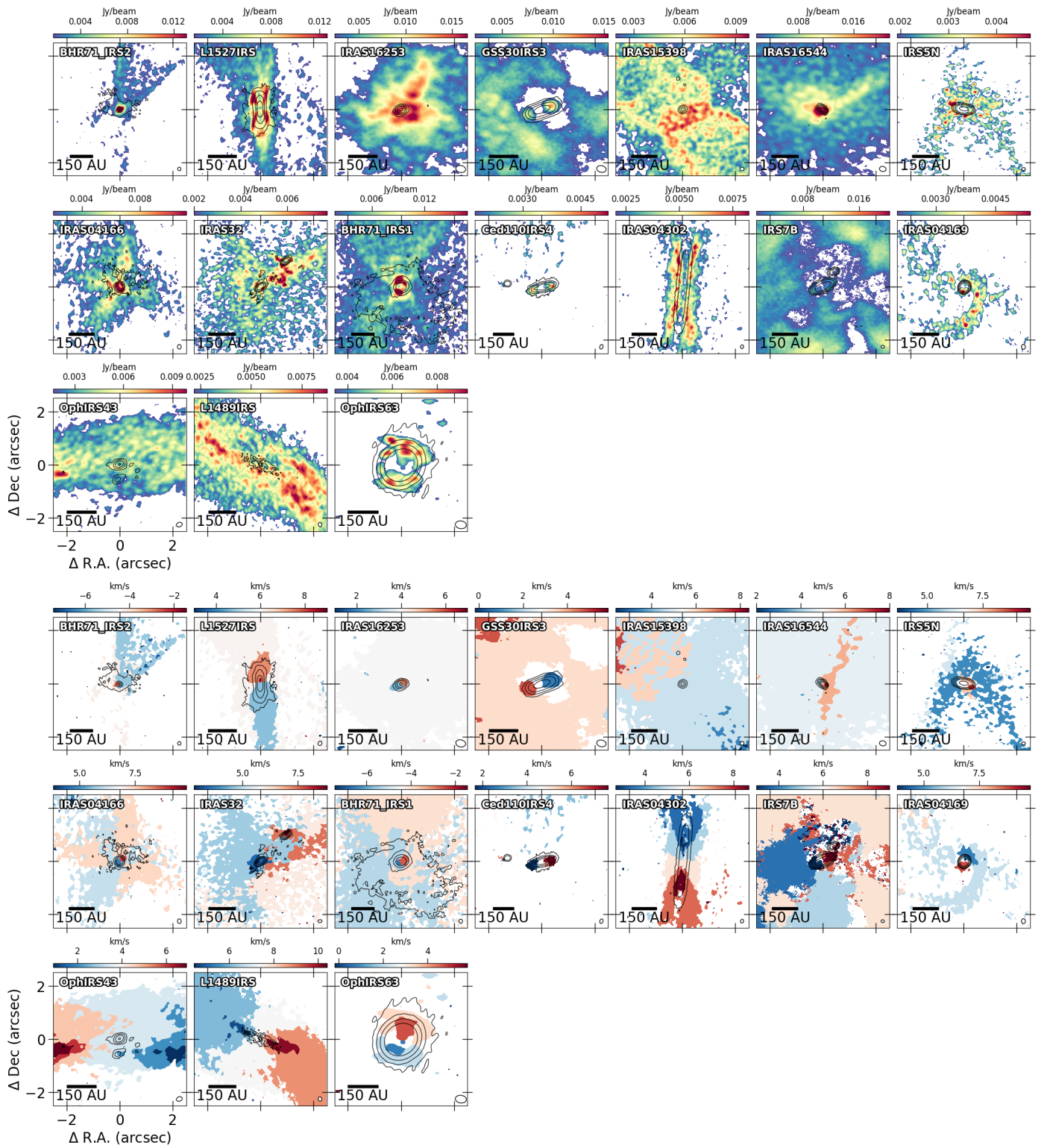


Fig. B.8. Same as Figure B.1 but for H_2CO ($3_{0,3} - 2_{0,2}$) instead.

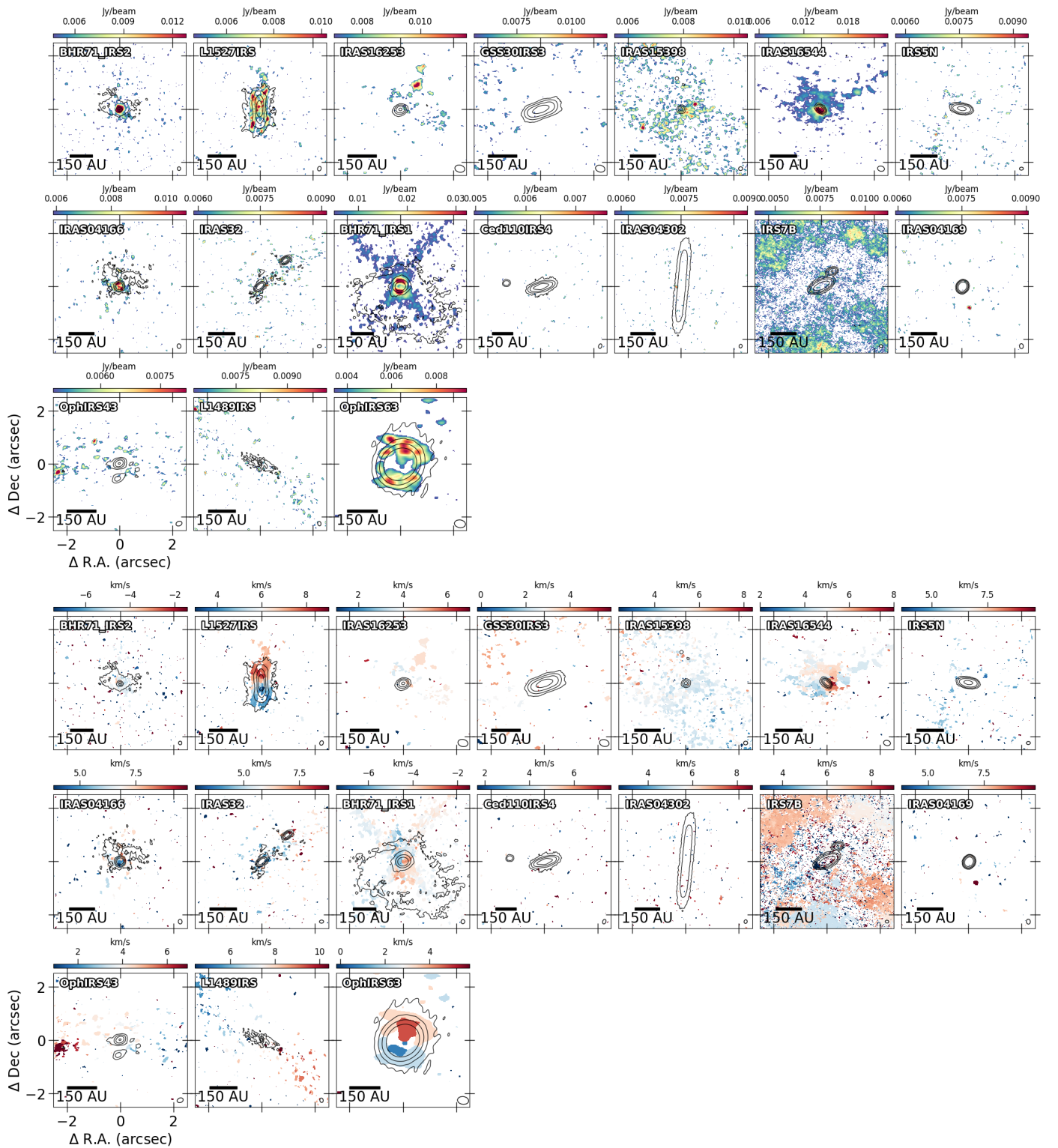


Fig. B.9. Same as Figure B.1 but for H_2CO (3_{2,1}–2_{2,0}) instead.

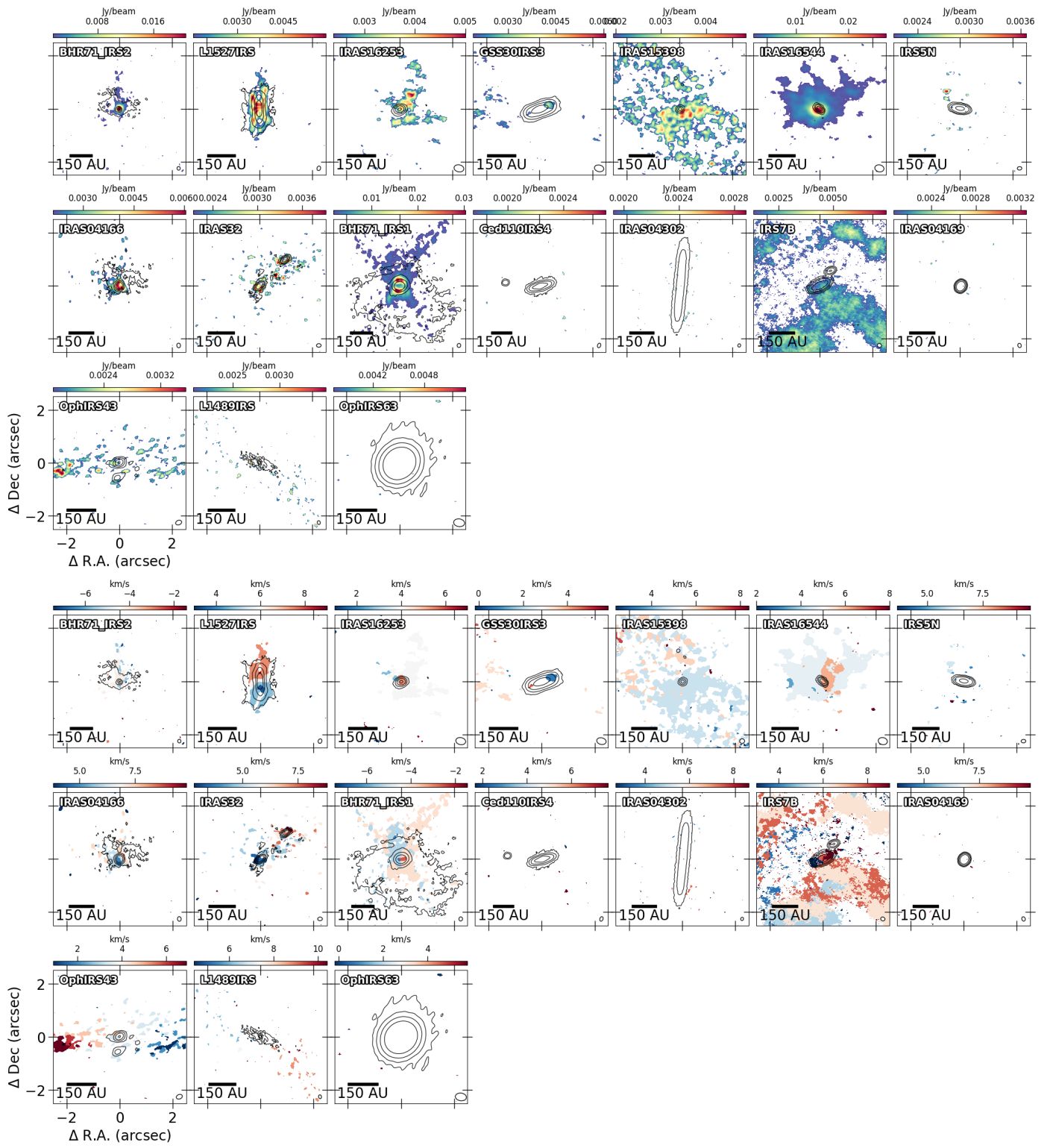


Fig. B.10. Same as Figure B.1 but for H_2CO ($3_{2,2}-2_{2,1}$) instead.

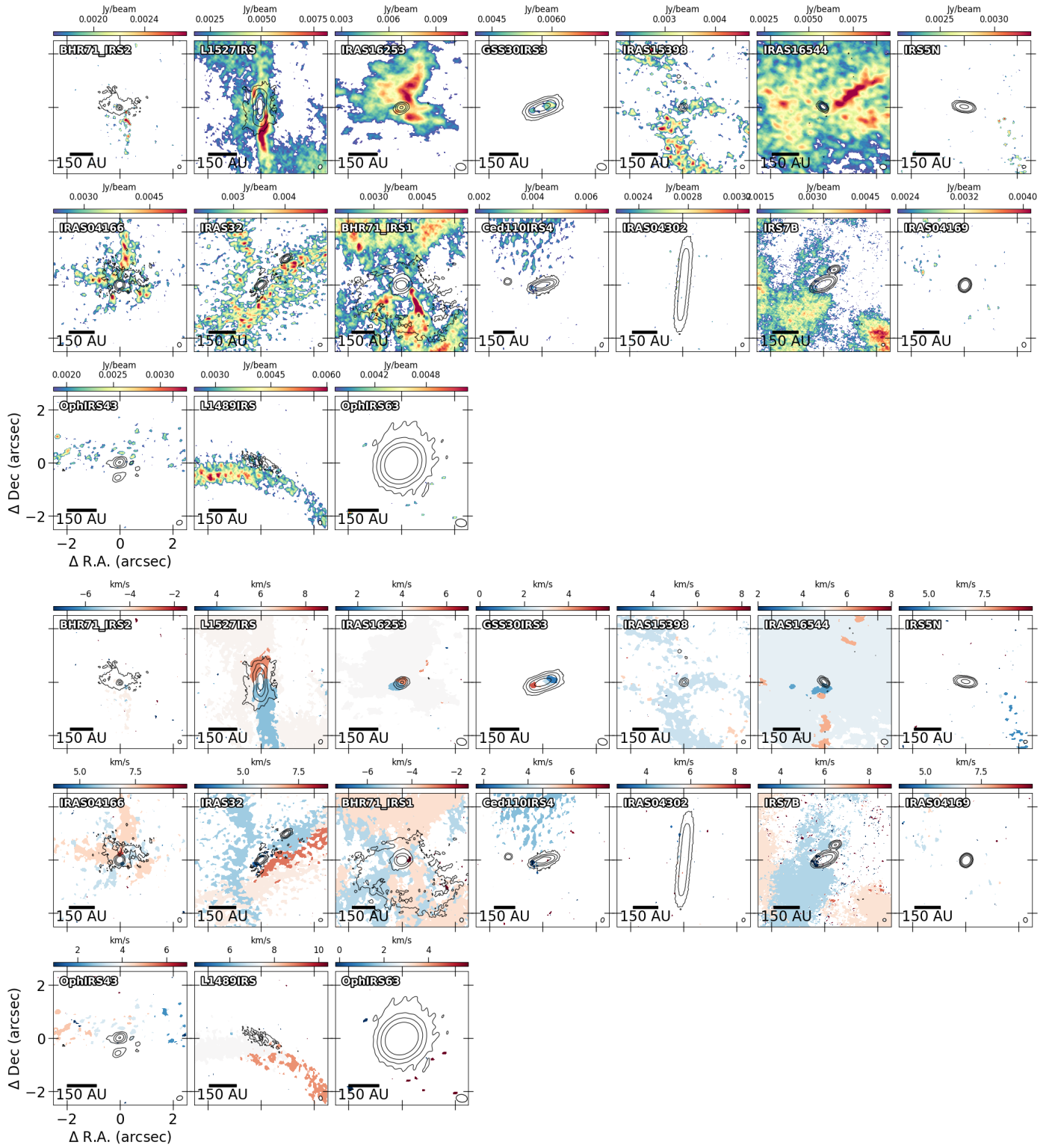


Fig. B.11. Same as Figure B.1 but for the blended c -C₃H₂ (6_{0,6}-5_{1,5}) and (6_{1,6}-5_{0,5}) transitions instead.

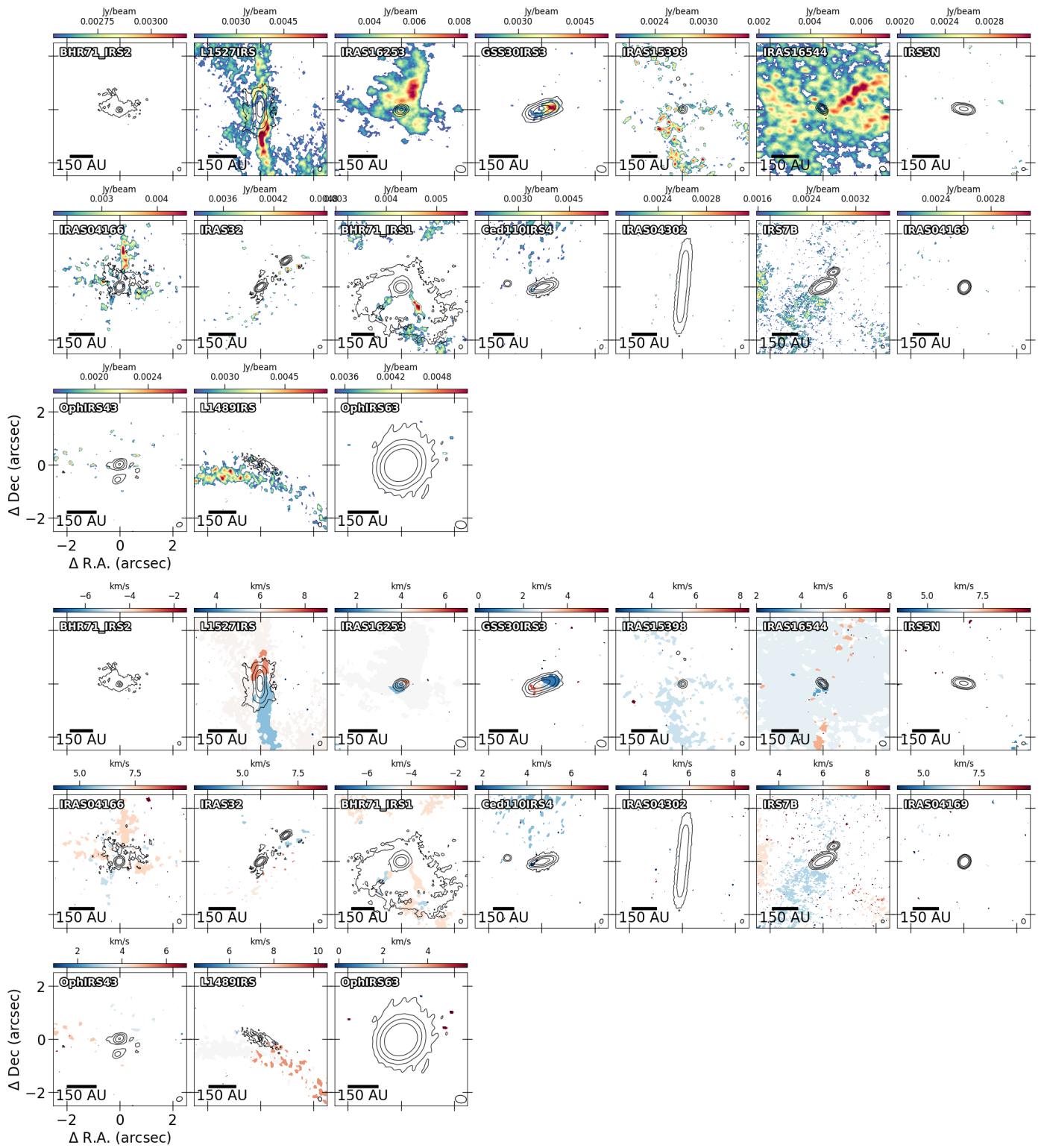


Fig. B.12. Same as Figure B.1 but for $c\text{-C}_3\text{H}_2 (5_{1,4}-4_{2,3})$ instead.

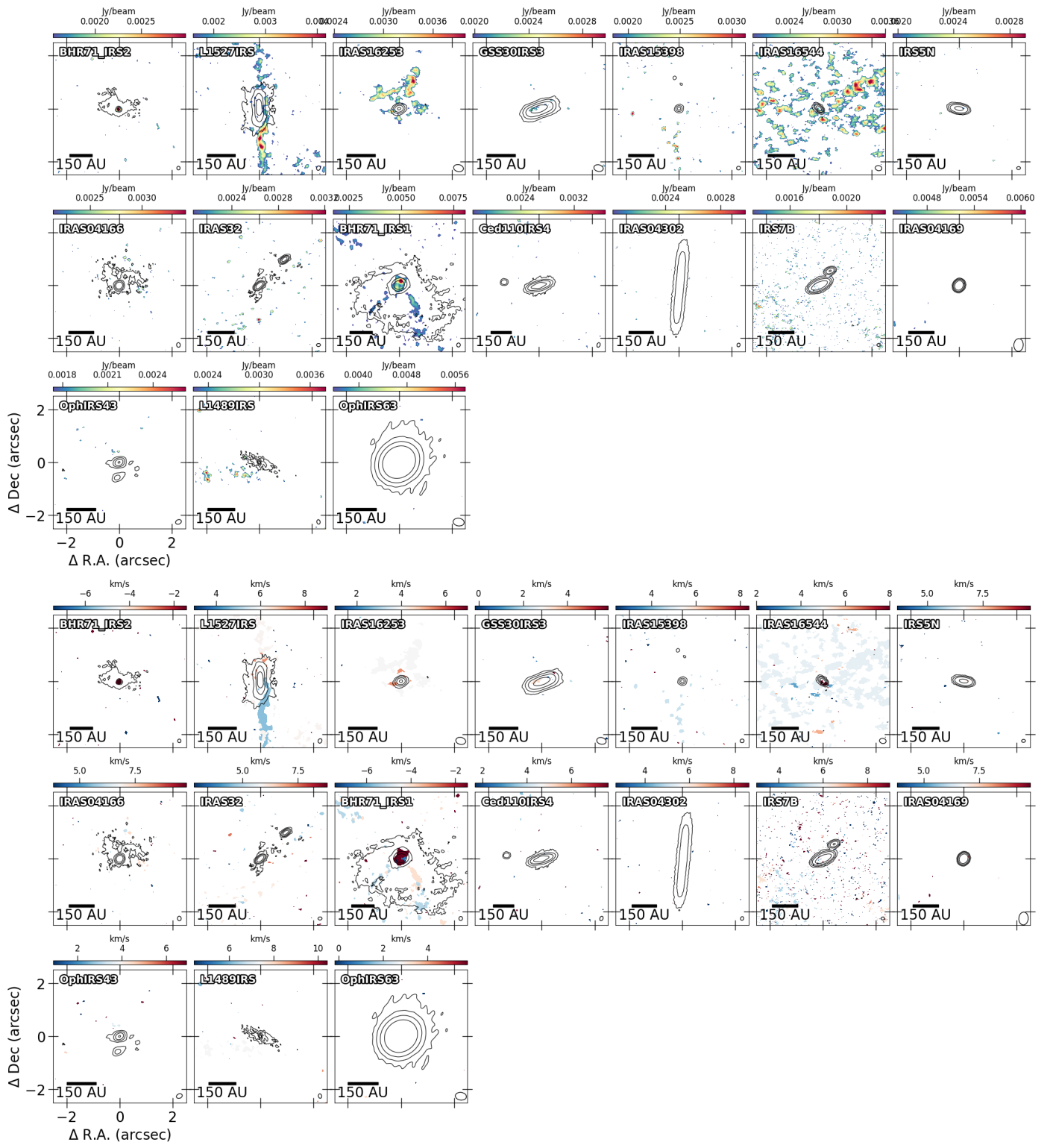


Fig. B.13. Same as Figure B.1 but for $c\text{-C}_3\text{H}_2$ ($5_{2,4}-4_{1,3}$) instead.